2023

MULTI-SCALE CHARACTERIZIATION OF PORE STRUCTURE AND MASS TRANSPORT IN NATURAL ROCKS

Xiaoqing Yuan

Recommended Citation

Yuan, Xiaoqing, "MULTI-SCALE CHARACTERIZIATION OF PORE STRUCTURE AND MASS TRANSPORT IN NATURAL ROCKS" (2023). *Earth & Environmental Sciences Dissertations*. 90.
https://mavmatrix.uta.edu/ees_dissertations/90

MULTI-SCALE CHARACTERIZIATION OF PORE STRUCTURE AND MASS TRANSPORT IN NATURAL ROCKS

by

Xiaoqing Yuan

Presented to the Faculty of the Graduate School of
The University of Texas at Arlington
in Partial Fulfillment of the Requirements
for the Degree of

DOCTOR OF PHILOSOPHY

THE UNIVERSITY OF TEXAS AT ARLINGTON

December 2023

ACKNOWLEDGEMENT

It is my pleasure to express gratitude to my advisors Dr. Qinhong Hu and Dr. Majie Fan for their guidance, support, and generosity. It was a great fortune to meet them and to work with them at the University of Texas at Arlington.

I genuinely thank my family for their uninterrupted and incomparable help, love, and support. I am forever grateful to my parents for giving me the opportunities and experiences that have made me who I am. They altruistically encouraged me to discover new directions in life and seek my destiny. This journey would not be possible without them, and I dedicate this dissertation to my parents. In closing, I want to express my heartfelt gratitude to my love, Zhenxun Zhuang, for standing by my side and fighting alongside me until the very end.

Nov 2023

TABLE OF CONTENTS

LIST OF ILLUSTRATIONS

LIST OF TABLES

ABSTRACT

MULTI-SCALE CHARACTERIZIATION OF PORE STRUCTURE AND MASS TRANSPORT IN NATURAL ROCKS

Xiaoqing Yuan

The University of Texas at Arlington, 2023

Supervising Professors: Dr. Qinhong Hu and Dr. Majie Fan

The mass transport process in porous natural rocks is notably influenced by the pore structure with both geometrical and topological attributes. Nevertheless, previous studies have not taken into consideration the sample size effect or the impact of diagenesis processes on petrophysical investigations of rocks, fluids, and rock-fluid interactions. Six rocks (one granodiorite, one limestone, two chalks, one mudstone, and one dolostone) with different extents of heterogeneity at six different particle sizes were studied to describe the effects of pore structure (especially connectivity) on mass transport. Thirteen geologically different rocks (two marbles, four fossiliferous limestones, six mudstones, and one sandstone) were studied to examine the influence of diagenesis on petrophysical parameters and the Archie's cementation factor (*m*). The methods applied for both studies were (i) porosity measurements of granular rocks, (ii) analyses of gas-phase diffusive transport in a bed of packed particles and intact rocks along with the development of a solid quartz method at six particle sizes to identify the intraparticle diffusion contribution, and (iii) batch sorption tests of multiple ions (anions and cations) using inductively coupled plasma-mass spectrometry. The granular porosity measurement results reveal that with decreasing particle sizes, the effective porosities for the “heterogenous” group of rocks (Grimsel granodiorite and Edwards limestone) increase, whereas the porosities of the “homogeneous” group (two Israel chalk samples, Japan mudstone, and Wyoming dolostone) remain roughly constant. Moreover, the batch sorption work displays a different affinity of rocks for various tracers in anionic and cationic forms. For Grimsel granodiorite, Japan mudstone, and Wyoming dolostone, the adsorption capacity of Sm^{3+} and Eu^{3+} increases as the particle size decreases. Cementation factor results show that diagenesis and microfractures could be root causes of various values of cementation factors in 13 natural rock samples. In general, this integrated research of grain size distribution, granular rock porosity, intraparticle diffusivity, ionic sorption capacity, and diagenetic pattern gives insights into the pore connectivity effect on both physical and chemical transport behaviors in different lithologies with different particle sizes.

CHAPTER 1. INTRODUCTION

1.1. Background

Mass transport within porous rocks is influenced by pore structure, which combines geometry (e.g., pore shape, pore size, pore size distribution, and pore surface area) and topology (e.g., pore connectivity) (Dullien, 2012; Hu et al., 2012). The effective porosity $\varnothing_e$ (i.e., the portion of total porosity $\varnothing_t$ wherein solute transport occurs) can be less than the overall pore space of the medium, because of the presence of "isolated" and "dead-end" pores that do not contribute to the overall transport, or sometimes because of size exclusion of solute molecules in sub-nm sized pore space (Hu et al., 2012). Various studies pointed out that a larger effective porosity, from a better connectivity aspect of pore structure, may occur in smaller-sized samples due to the opening of "isolated" pores in heterogeneous and tight rocks (Hu et al., 2012; Davudov & Moghanloo, 2018; Wu et al., 2018; Fu et al., 2019). It has also been widely reported that porous media with various pore structure characteristics usually display different mass transfer behaviors (Hu et al., 2002; Kosuge et al., 2007; Hu et al., 2012; Sun et al., 2017; Yang et al., 2018; Li et al., 2019). A determination of the effects of pore connectivity on transport processes has been improved by applying both physically-based fluid flow and chemically-related reactive transport experiments, as well as associated theoretical analyses (Tachi et al., 1998; Ewing & Horton, 2002; Hu & Mao, 2012; Peng et al., 2012; Hu et al., 2015; Yan et al., 2018).

A measurement of gas diffusion with non-reactive and conservative gas tracers is an efficient approach to probing the pore structure of, and mass transport through, various natural rocks (Moldrup et al., 2007; Peng et al., 2012). It is generally believed that, for non-reactive tracers, the ratio of the pore diffusion coefficient D_P in porous geomaterials to that in free air D_0, is governed only by the pore network parameters (e.g., porosity, pore size distribution, and tortuosity). Fick's second law of diffusion has been employed to evaluate the non-steady-state diffusion fluxes. In previous research, the gas diffusion coefficient has been measured in soils using the method described by Currie (1960). Peng et al. (2012) first investigated the effect of pore structure on diffusivity, using Currie's method to conduct gas diffusion tests in 11 intact rocks, and reported that the intact samples with smaller mean pore size and wider pore size distribution exhibited lower gas diffusivities. In granular and aggregated media, such as fine-grained rocks like shale, diffusion can occur though both intra-particle and inter-particle pathways, and their respective contributions to transport in such packed granular samples have not been thoroughly investigated (Hu & Wang, 2003). Phounglamcheik et al. (2022) attempted to evaluate the effect of intra-particle and inter-particle diffusion on the reaction rate of char gasification using thermogravimetric analysis based on various particle size distributions of samples, and they found that the intra-particle diffusion can be roughly estimated from the mean particle size distribution. To summarize, previous studies have mainly focused on intra-particle diffusion, affected either by mean pore size or particle size distribution, without considering the effect of crushed granular sizes. Furthermore, the influence of pore connectivity (related to rock type, heterogeneity, and resultant particle size-dependent effective porosity; Hu et al., 2002) on intra-particle diffusion has not been examined. In this work, we used the two-chamber diffusion method, originated by Currie (1960) and later developed by Rolston and Moldrup (2002) with oxygen as the gas tracer, to examine the effects of particle size and pore connectivity on intra-particle diffusion in six different particle sizes of six rocks with different extents of heterogeneity.

In addition to gas diffusion, ionic sorption and transport in natural rocks is linked to their pore connectivity via sample size-dependent effective porosity and accessible pore surface (Hu et al., 2015). The sorption capacity of ions onto adsorbents, owing to their ability of selective binding, has been well documented for both geological and industrial materials (He et al., 2011). Chemical characteristics, surface area, pore structure, and initial concentration of adsorbate have long been indicated as parameters in controlling ionic sorption and transport in various engineered and geological materials (Chang & Lenhoff, 1998; Li et al., 2012; Punyapalakul et al., 2013; Wang et al., 2015; Hong et al., 2019). For example, the importance of pore connectivity was suggested by Chang and Lenhoff (1998), as it influences the upper limit of adsorptive uptake. Particles with larger sizes are correlated with reduced adsorption (Wang et al., 2015). Nonetheless, many geological media, such as sedimentary and igneous rocks being made up of various minerals, are different from industrial man-made materials involved in previous studies (Mohammed et al., 2021). Moreover, due to the specific physical structure and chemical properties, minerals vary in their sorption capacities for binding different ions. For instance, the presence of layered clay minerals increases the sorption properties corresponding to the presence of interlayer surface (Zhuang & Yu, 2002) and exhibits higher adsorption affinities for heavy metals such as Cs^+ and Ba^{2+} (Yao et al., 2020; Musso et al., 2022).

The cementation factor (m) has been widely applied in groundwater exploration, hydrocarbon reservoir evaluation, and porous-media engineering studies (Archie, 1942; Wyllie & Gregory, 1953; Focke & Munn, 1987; Donaldson & Siddiqui, 1989; Salem & Chilingarian, 1999). Previous papers have focused on the effects of pore systems on cementation factors (Focke & Munn, 1987; Gao et al., 2013; Wu et al., 2020). Focke and Munn (1987) pointed out that the large cementation factor variations in carbonates can be attributed to different porosity types in reservoirs. Gao et al. (2013) concluded that for samples with various cementation factors, different exponential correlations exist between diffusivity and average pore diameter. However, the dependence of m on the degree of diagenesis was not examined in those works. The interpretation of genesis for this complex reservoir property from multiple perspectives is needed since complex pore structure and rock properties are well recognized to be the end-products of geological processes (depositional, structural, and diagenetic processes) (Katsube & Williamson, 1994; Liu et al., 2015; Lai et al., 2018; Gao et al., 2020). To emphasize the roles of mineralogy and diagenetic modifications on cementation factor, we conducted X-ray diffraction (XRD) analyses, thin section petrography, and field emission-scanning electron microscopy (FE-SEM) observations in this work.

In porous media, the cementation factor affects gas molecular diffusion coefficient (Tabibi & Emadi, 2003). It is generally believed that the cementation factor is the exponent constant in the empirical function to estimate the diffusion coefficient (Boving & Grathwohl, 2001; Grathwohl, 2012; Peng et al., 2012). Consequently, gas diffusivity has been widely applied to extract the reliable value of m (Boving & Grathwohl, 2001; Mu et al., 2008; Peng et al., 2012; Gao & Hu, 2013; Chagneau et al., 2015; Fang et al., 2018; Wei et al., 2019). Meanwhile, as a straightforward approach for gas diffusivity measurement, the gas diffusion chamber method with oxygen as a tracer was applied in the literature (Currie, 1960; Peng et al., 2012). On the other hand, using the Bosanquet equation to accurately determine the effective diffusion coefficient in porous media has also been adopted in some research (Gao et al., 2013; Fang et al., 2018; Wu et al., 2018). Knudsen diffusion coefficient, a key parameter for the gas diffusivity prediction in the Bosanquet formula, was obtained from mercury intrusion porosimetry (MIP) test, a well-developed characterization tool, in this work. Since MIP has also been widely used for providing information regarding pore structure (Pittman, 1992; Plötze & Niemz, 2011; Gao et al., 2013; Hu et al., 2017), pore size distribution and permeability data were also obtained from this test.

Since the cementation factor (m) varies widely in complicated lithologies, both sedimentary rocks (mudstone and fossiliferous limestone) and metamorphic rocks (marble) were covered in our work. Specifically, mudstones are fine-textured terrigenous rocks with grain sizes typically less than 5 μm (Friedman, 1978; Loog et al., 2001; Sondergeld et al., 2010). In recent years, deeper understandings of mudstone diagenesis in fine-grained sedimentary systems have been rapidly established (Mondol et al., 2007; Taylor et al., 2014; Zhai et al., 2018; Liu et al., 2019). The compaction and cementation of fine-grained sediment result in relatively poor matrix physical properties in mudstone (Mondol et al., 2007). The diagenesis of carbonate sediments generally includes processes such as cementation to produce limestones and dissolution to produce microporosity and cave systems (Tucker & Bathurst, 2009). Especially, for biological limestone, the complexity of pore systems could be higher as a result of the presence of bioclasts in rocks (Timur et al., 1971; Ghamartale et al., 2019). Marble, the metamorphism of sedimentary carbonate rocks, consists of large calcite and/or dolomite in a tight matrix, with the grains well cemented with each other (Yavuz et al., 2010; Taylor et al., 2014). Moreover, it was reported that crack-induced damage that occurred in marbles was higher than other carbonate rocks, significantly enhancing the reservoir quality (He et al., 2016; Lim et al., 2021).

The problem statements in this study are summarized as follows:

1. There is a need to develop an appropriate method to derive intraparticle gas diffusivity,
2. Previous studies didn't investigate the effects of clay minerals and particle sizes on ionic sorption,
3. The relationship between the chemical sorption and pore connectivity of granular rock samples was insufficiently evaluated, and

4. The relationships between diffusivity and porosity, permeability, and average pore diameter, as well as the correlations between porosity and permeability and the cementation factor, were not adequately studied.

Accordingly, the specific research objectives in this study are listed below:

1. To derive intraparticle gas diffusivity using the solid quartz method,
2. To assess the effects of clay minerals and particle sizes on ionic sorption,
3. To link chemical sorption of granular rock samples to their pore connectivity, and
4. To explore the correlations of diffusivity to porosity, permeability, and average pore diameter, as well as of porosity and permeability to cementation factor.

1.2. Motivation and Objectives

This research focuses on the combined effects of pore connectivity and component minerals on mass transport in natural rocks. The adsorption capacity of rocks is strongly correlated with the accessible inner and external surface areas, influenced by pore connectivity and particle sizes. The intrinsic adsorption affinity of rocks is controlled by component minerals. Therefore, the first project investigates the impacts of pore connectivity and particle sizes on the mass transport behaviors of several natural rocks based on complementary approaches of pore structure characterization, gas diffusion, and batch adsorption experiments. Six geologically different rocks with six different particle sizes were chosen to present various extents of pore connectivity, particle sizes, and component minerals in natural rocks that are important for energy and environmental geosciences. The pore connectivity was investigated by grain size distribution, MIP, size-dependent effective porosity with the measurements of both particle and bulk densities, and intra-particle and inter-particle gas diffusion. These rocks were also crushed and sieved into six particle sizes to investigate the particle size effect and associated pore connectivity. Basic properties were analyzed for mineralogy and pore types with X-ray diffraction (XRD) and scanning electron microscopy (SEM). The porosity of each crushed rock with a specific particle size was measured to analyze the scale-dependent effective porosities of these natural rocks. The intra-particle diffusivity was quantified using the solid quartz method developed in this work.

A series of batch adsorption experiments were then conducted with a suite of tracer chemicals (both anions and cations with non-sorbing and sorbing nature) to assess the sorption capacity of the six rock samples with inductively coupled plasma-mass spectrometry (ICP-MS) analyses, a robust and sensitive technique used to detect multiple elements of both tracers and intrinsic elements (Hu et al., 2005; Hu & Mao, 2012). The particle size and sorption capability of rocks (and associated mineral components) were analyzed based on adsorption results. The relationships among the particle sizes, pore connectivity, intra-particle diffusivity, and ionic sorption capabilities of these six natural rocks were then discussed. The results and findings in this study will provide valuable information for the mass-transport assessment in various porous media, with a coupled perspective of pore structure and physical-chemical processes.

The work also examined the internal impact of diagenesis on the cementation factor. The objectives are to obtain the cementation factor from gas diffusion tests and Bosanquet formula method and to clarify the diagenetic influences on the cementation factor. Thirteen pieces of geologically different rocks, including two marbles, four fossiliferous limestones, six mudstones, and one sandstone were selected to achieve the research objectives. A comparative analysis of the cementation factor was analyzed based on gas diffusion and MIP tests. The correlations of diffusivity to porosity, permeability, and average pore diameter were analyzed, respectively, as well as the effects of porosity and permeability on cementation factors. In addition, thin section petrography and FE-SEM observations were conducted to clarify the diagenetic contributions to cementation factors. Finally, diagenetic patterns for these 13 samples were established, and the effects of diagenetic process and microfractures on the cementation factor were discussed.

1.3. Dissertation Structure

The subsequent chapters of this dissertation are organized as follows:

Chapter 2 presents an extensive review of the fundamentals of pore structure system within porous rocks, with the introduction of both geometry (e.g., pore shape, pore size, pore size distribution, and pore surface area) and topology (e.g., pore connectivity) characteristics.

Chapter 3 proposes a solid quartz method to derive the intraparticle gas diffusivity, with both intra-particle and inter-particle diffusion coefficients calculated and compared between different samples and particle sizes.

Chapter 4 reports the batch sorption results for anionic and cationic tracers in studying chemical sorption onto porous media by examining the effect of adsorbent particle sizes on chemical sorption to verify the particle size effect.

Chapter 5 centers on the influence of diagenetic processes and patterns on gas diffusion to investigate the effect of the degree of diagenesis on cementation factor values.

Chapter 6 summarizes key conclusions and offers recommendations for future studies.

CHAPTER 2. PORE STRUCTURE SYSTEM IN NATURAL ROCKS

2.1. Introduction

In this chapter, a comprehensive examination of pore structure types (heterogeneous and relatively homogeneous) effects on gas transport (gas diffusion) behavior were studied. Initially, the definition of pore structure type is introduced. Subsequently, a solid quartz method was proposed to derive intraparticle gas diffusivity. Finally, the behaviors of gas transport in natural rocks are summarized and analyzed, followed by a discussion of the effects of pore sizes and pore structure on gas diffusion.

2.2. Pore network system and heterogeneity

2.2.1. Pore network system

The nature of pore systems is a key aspect of reservoir description (Hollis et al., 2010; Hiatt & Pufahl, 2014). The most important characteristics of the pore system are thought to be pore type, pore-to-throat size ratio, throat-to-pore coordination number in some network patterns, and degree of non-random heterogeneity (Wardlaw & Cassan, 1978; Wardlaw, 1980; Dehghan et al., 2009; Gallagher, 2014; Lai et al., 2018). In porous systems of natural rocks, pore types range from interparticle and intraparticle mineral-matrix pores to organic matter pores to dissolution and fractures pores (Anovitz & Cole, 2015; Ji et al., 2019). Alternatively, the effective porosity $\emptyset_e$, i.e., the portion of total porosity $\emptyset_t$ wherein solute transport occurs, can be less than the overall pore space of porous medium, because of the presence of “isolated” and “dead-end” pores that do not contribute to the overall transport, or sometimes because of size exclusion of solute molecules in sub-nm sized pore space (Hu et al., 2012). Various studies pointed out a larger effective porosity may occur in smaller-sized samples due to the opening of “isolated” pores in heterogeneous and tight rocks (Hu et al., 2012; Davudov & Moghanloo, 2018; Wu et al., 2018; Fu et al., 2019; C Zhao et al., 2021). In terms of pore shape, the ink-bottle-shaped type, characterized by narrow necks and wide bodies, and slit-shaped pores are common in pore systems. Additionally, the pore sizes in rocks are grouped into five categories by the America (2008): macropores (>75 μm), mesopores (30-75 μm), micropores (5-30 μm), ultramicropores (0.1-5 μm), and cryptopores (<0.1 μm). While, according to the International Union of Pure and Applied Chemistry (IUPAC) classification, pores with diameters <2 nm, 2-50 nm, and >50 nm are termed as micro-, meso-, and macropores, respectively. Moreover, pore size distributions in natural geomaterials typically cover full range of pore sizes from very fine to very coarse (Kate & Gokhale, 2006; Choo & Borja, 2015). Generally, bimodal, unimodal and multimodal distributions of pore radii are observed in pore networks (Emmanuel & Berkowitz, 2007; Yao et al., 2010; Wang et al., 2019).

On the other hand, analytical description of the geometric and topological properties of the pore space have been essential for a better understanding of the complex pore structure properties of a natural porous medium (Vogel & Kretzschmar, 1996; Silin & Patzek, 2006; Hajizadeh et al., 2011; Gong et al., 2020). In order to evaluate the spatial distribution of pore space, pore geometry (e.g., pore shape, pore size, pore size distribution, and pore surface area) and topology (e.g., pore connectivity) were considered among previous studies (David, 1993; Peth et al., 2008; Keller et al., 2011; Dullien, 2012; Hu et al., 2012). Particularly, pore connectivity is one of the most important parameters to quantify pore structure of porous material (Portsmouth & Gladden, 1991; Armatas, 2006; Bernabé et al., 2016; Lucas et al., 2021). For instance, Fauzi et al. (2002) and Xiong et al. (2016) reported that pore connectivity is the most important influence on the permeability. In addition, the effect of pore connectivity on mass transport phenomena such as its implications for fluid flow and chemical transport have been examined and clarified (Armatas, 2006; Bernabé et al., 2016; Yuan et al., 2023). It has been widely reported that porous media with various pore structure characteristics usually display different mass transfer behaviors (Hu et al., 2002; Kosuge et al., 2007; Sun et al., 2017; Yang et al., 2018; X. Li et al., 2019). The determination of the effects of pore connectivity on transport processes has been improved by applying both physically-based fluid flow and chemically-related reactive transport experiments, as well as associated theoretical analyses (Tachi et al., 1998; Ewing & Horton, 2002; Hu et al., 2012; Peng et al., 2012; Hu et al., 2015; Yan et al., 2018). Basically, better and high degree of pore connectivity in the network enhances the mass transport performance. However, the sample size effect on the connectivity of pore space is difficult to measure in rock samples because the pore space is spatially correlated at the pore (Bryant et al., 1993; Vogel & Roth, 2001; Okabe & Blunt, 2005; Xiong et al., 2016).

2.2.2. Pore network heterogeneity (heterogeneous and relatively homogeneous)

Due to its composition of various mineral identity, organic materials, pores, cracks, joints, and layers, rock is a typical and naturally heterogeneous material composed of inherent microstructures at the grain scale (Borodich et al., 2015; Navarre-Sitchler et al., 2015; Li et al., 2020; Li et al., 2022). The distribution of overall pore spaces in pore systems of reservoirs ranges from being relatively homogeneous to heterogeneous (Wu et al., 2006; Hollis et al., 2010; Jiang et al., 2013; Jiang et al., 2018; Yuan et al., 2023). As a result, the degree of spatial heterogeneity varies considerably among rock samples (Tews et al., 2004; Xue et al., 2016; Yuan et al., 2023). In fact, both macroscopically and structurally homogeneous and heterogeneous pore systems in natural rocks were reported (Greenkorn et al., 1965; Sahimi, 1993; Knözinger & Kochloefl, 2000; Noiriel et al., 2005; Drits et al., 2010). Therefore, one may consider, to some extent, that a fairly homogeneous pore systems are practically uniform (Wyllie & Spangler, 1952; Dubinin & Stoeckli, 1980; Akin et al., 2000; Amini & Qi, 2000; Teng & Zhao, 2000).

The heterogeneity of pore structure greatly affects fluid flow and solute transport such as gas diffusion and sorption in porous media (Cai et al., 2013; Schmitt et al., 2015; Cao et al., 2016; Cai et al., 2018). In general, reservoir rocks with a high degree of homogeneity, having a single pore system, tend to exhibit high matrix porosity. However, reservoir rocks displaying higher heterogeneity, which means that there are significant spatial variations in the properties when different regions of the pore space are sampled, have a significant impact on the overall quality of reservoirs (Ping & Machel, 1995; Yuan et al., 2023). In particular, the pore structure heterogeneity has a considerable impact on the pathway of fluid migration, as indicated by Li et al. (2022). To illustrate, gas exhibited rapid flow rates within substantial pores and vugs, while its flow was notably sluggish within microfractures.

Furthermore, numerous researchers have employed fractal dimensions to assess the heterogeneity and quantify the complex geometry of pore structures in rock materials (Mandelbrot & Mandelbrot, 1982; Katz & Thompson, 1985; Li et al., 2017; Wang et al., 2021). Fractal dimension, as a measure of rock heterogeneity, suggests that a higher fractal dimension corresponds to increased heterogeneity (Plötze & Niemz, 2011; Li et al., 2017; Wang et al., 2021).

CHAPTER 3. MASS TRANSPORT AND CONTROLLING FACTORS

3.1. Introduction

It has been widely reported that porous media with various pore structure characteristics usually display different mass transport behaviors (Hu et al., 2002; Kosuge et al., 2007; Sun et al., 2017; Yang et al., 2018; Yang Li et al., 2019). Various studies (Hu et al., 2012; Davudov & Moghanloo, 2018; Wu et al., 2018; Fu et al., 2019; Zhao et al., 2021) also pointed out that a larger effective porosity, from a better connectivity aspect of pore structure, may occur in smaller-sized heterogeneous samples due to an opening of “isolated” pores. Gas diffusion with non-reactive and conservative gas tracers is an efficient approach to probing the pore structure of various natural rocks (Moldrup et al., 2007; Peng et al., 2012). It is generally believed that D_P/D_0, which is the ratio of the gas coefficient D_P in geomaterials to that in free air D_0, is only governed by the effect of pore network parameters (e.g., porosity, pore size, and tortuosity). Fick's second law of diffusion has been employed to evaluate the non-steady-state diffusion fluxes. Previous studies mainly focus on intra-particle diffusion being affected either by mean pore size or particle size distribution, without considering the effect of specific particle size. Furthermore, the influence of pore connectivity related to rock types, the extent of heterogeneity, and resultant particle size and effective porosity, on intra-particle diffusion has not been examined. Hence, in this work, we used the two-chamber method, originated by Currie (1960) and late developed by Rolston and Moldrup (2002) with oxygen as the gas tracer, to examine particle size and pore connectivity effect on intra-particle diffusion in six different granular sizes of six natural rocks with different extents of heterogeneity.

3.2. Materials

3.2.1. Sample selection

Six natural rock samples, with different extents of heterogeneity at different observational scales, were selected for this work, including sedimentary (limestone, white chalk, gray chalk, mudstone, and dolostone) and igneous (granodiorite) types (Table 1). Complex component particles (from biological and non-biological origins), associated with post-depositional evolution, result in a tremendously heterogeneous distribution of pores and a high value of tortuosity in

limestone (Choquette & Pray, 1970; Regnet et al., 2019). **Chalk** is commonly regarded as a sedimentary rock that is homogeneous at the measurement scales of the physical properties (Siemers et al., 1994; Mitchell et al., 1997; Fabricius, 2007); however, microfossils (e.g., foraminifera and chalk coccolith) have been observed in chalk matrix (Schlanger & Douglas, 1974; Mitchell et al., 1997). Two chalk samples, white and gray, were used in this work. Most shallow and organic matter-poor **mudstones** are lithologically homogeneous but with very fine pores and large tortuosity to serve as excellent caprocks (Hu et al., 2015; Klaver et al., 2015; Yang et al., 2019; Hu et al., 2021). The **dolostone** is homogeneous with respect to its constituent dolomite crystals (Jones et al., 2001; Allen et al., 2002; Jones & Luth, 2003). In addition, **granodiorite** is generally composed of feldspars, quartz, and mica with various grain sizes on the order of mm scales. The heterogeneity of minerals and pore structure of natural granodiorite has been studied extensively, mostly from the perspective of a geological repository for high-level nuclear waste (Voutilainen et al., 2017; David et al., 2018; Regnet et al., 2019). David et al. (2018) discussed the presence of tiny pores isolated from the interconnected network in granodiorite by coupled broad ion beam-SEM observations.

Table 1. Location, lithology, and relative extent of heterogeneity of samples

Sample name	Source	Lithology	Heterogeneity
Grimsel granodiorite	Grimsel Test Site, Switzerland	Igneous -intrusive	Heterogeneous
Edwards limestone	Texas, USA	Sedimentary	Heterogeneous
Israel white chalk	Negev Desert, Israel	Sedimentary	Relatively homogeneous
Israel gray chalk	Negev Desert, Israel	Sedimentary	Relatively homogeneous
Japan mudstone	Wakkanai Formation in Honorobe, Japan	Sedimentary	Relatively homogeneous

Wyoming dolostone	Wyoming, USA	Sedimentary	Relatively homogeneous

3.2.2. Sample preparation

These six samples included both heterogeneous and relatively homogeneous rock types. These intact rocks from either outcrops or cores were first crushed and sieved under one passing according to ASTM C136-01 (2017), using a stack of stainless sieves with mesh sizes of 0.075, 10.18, 0.5, 0.85, 1.7, and 2.36 mm; therefore, particle sizes of crushed samples range in the sequence of 75-177, 177-500, 500- 841, 841-1700, 1700-2360, and 2360-8000 μm. Moreover, other pieces of intact samples were also ball-milled to powder for XRD and grain size distribution analyses and cut to 1cm cube for MIP measurement. Consequently, the effects of heterogeneity and particle size on pore structure and mass transport (gas diffusion) behaviors could be evaluated by using these six rock samples at different particle sizes (Table 2).

Table 2. Summary of sample preparation and testing methods used in this study for six natural rocks.

Sample preparation	Testing methods (associated Sections)
Granular sample at six size fractions (2360-8000, 1700-2360, 841-1700, 500- 841, 177-500, and 75-177 μm)	Grain and bulk densities for granular porosity (3.3.5; 3.4.3); Gas- phase diffusion (3.3.6; 3.4.4)
Ball-milled powder	XRD (3.3.1; 3.4.1); Grain size distribution analyses (3.3.3; 3.4.2)

1-cm cubic sample	SEM (for two Israel chalks) (3.3.2); MIP (except for Wyoming dolostone) (3.3.4)

3.3. Methods

3.3.1. XRD for mineralogy

XRD analyses were performed to provide the mineralogical composition of these samples. The diffraction spectrum was recorded for each powder-sized (<75 μm) sample by X-Ray Diffractometer (Shimadzu Maxima X XRD-7000) with CuKα radiation at a speed of 2°/min, and the variation of diffraction angle was from 2° to 70°. The XRD data were then analyzed with Jade 9 software using the whole pattern empirical peak profile-fitting method to determine the average mass of minerals.

3.3.2. SEM imaging

The use of SEM can help to effectively evaluate the pore structure characteristics such as intra- and inter-particle pores, organic matter-hosted pores, micro-fractures, as well as correlation between pore space and (Fandrich et al., 2007; Klaver et al., 2015). Two fossil-rich white and gray chalk samples were examined by SEM. Samples were sandpaper-polished, argon ion-milled with TORR CrC-100 Sputtering system, Pt-coated, and observed using Field Emission-SEM (Hitachi S-4800) with a working current of 10 kV.

3.3.3. Grain size distribution measurement of the finest fraction after ball milling

Previous studies about the effects of grain size distribution on rock heterogeneity reveal that natural rock with a uniform grain size distribution may appear homogeneous, otherwise the heterogeneity will be much more obvious (Khasainov et al., 1997; Fitch et al., 2015). In our work, each intact sample was ball-milled to separate the minerals, and then grain size distributions of the produced granular powders were obtained using a Shimadzu SALD-7101 Grain Size Analyzer.

Several parameters were obtained from grain size analyses for heterogeneity evaluation, including the characteristic grain diameter d_x (where d_x is the characteristic grain size where x% of the mass is finer than d_x), the uniformity coefficient C_u ($C_u = d_{60}/d_{10}$), the curvature coefficient C_c ($C_c = d_{30}^2/(d_{10} \times d_{60})$. The material is classified as well-graded, namely heterogeneous, when the C_u values are greater than 5 and the C_c falls between 1 and 3 (Jia et al., 2016).

3.3.4. MIP measurement

Pore structure characteristics of natural rocks have long been investigated by MIP analyses (Porcheron et al., 2004; Kaufmann et al., 2009; Schmitt et al., 2013; Gao & Hu, 2018). Oven-dried 1-cm cubic samples were subjected to MIP analyses at pressures from 0.034 MPa to 413 MPa with Micromeritics AutoPore 9520. The corresponding detectable pore-throat diameter ranged from 45,000 to 2.8 nm based on the Washburn equation (Katz & Thompson, 1986; Gao & Hu, 2018). The fractal dimension of pore structure based on MIP is helpful for the heterogeneity evaluation of natural rocks. Specifically, the MIP test derives fractal dimension for the entire range of pores, the total dimension (D), can be applied as key parameter to quantify the rock heterogeneity according to fractal theory (Mandelbrot & Mandelbrot, 1982; Katz & Thompson, 1985). It was generally believed that larger values of the total fractal dimension correlate to higher heterogeneity of pore structure (Li et al., 2017; Wang et al., 2021).

$$\log S_W = \log(1 - S_{Hg}) = (3 - D)\log r - (3 - D)\log r_{max} \quad (1)$$

where S_W is the cumulative pore volume fraction (%), S_{Hg} is the mercury saturation (%), D is the fractal dimension, r_{max} is the maximal pore radius (μm).

As the natural rocks have a wide spectrum of nm-μm pore sizes, the fractal dimensions of mesopores D_1, transitional pores D_2, and micropores D_3 were calculated according to Eq. 15 in three pore size intervals. The total fractal dimension D of the entire pore space was obtained by the weighted average of porosity for mesopores, transitional pores, and micropores.

$$D = (D_1 \times \emptyset_1 + D_2 \times \emptyset_2 + D_3 \times \emptyset_3)/(\emptyset_1 + \emptyset_2 + \emptyset_3) \quad (2)$$

where $\emptyset_1$, $\emptyset_2$, and $\emptyset_3$ are the porosities corresponding to pore throat diameters in the 100-1000 nm, 10-100 nm, and 2.5-10 nm ranges.

3.3.5. Porosity measurements of crushed rock samples

A measurement of accessible porosity can be obtained by a combination of bulk density and true (particle) density measurements of both intact and crushed rocks (RP40, 1998; Zhao et al., 2021). The bulk density of an oven-dried granular sample was determined with Micromeritics GeoPyc 1365, a displacement measurement equipment. Tiny (127±40 μm) solid materials, namely DryFlo^{TM}, were used to envelop the samples for bulk volume measurements. The volume of sample as well as the total volume of sample and DryFlo^{TM} particles were calculated under rotating movement and desired pressure. The sample bulk density was calculated by dividing sample mass by the difference between two calculated volumes. A modified GeoPyc method (Zhao et al., 2021) using solid quartz powder (<75 μm in dia.) to substitute DryFlo^{TM} particles was applied for the bulk density analyses of small-sized granular samples (typically 75 – 1000 μm in dia.) when the enveloping capabilities of DryFlo^{TM} are questionable as the sizes of sample and enveloping materials become similar.

In addition, true (skeletal or grain) density of porous media was measured using a helium pycnometer density technique with Micromeritics AccuPyc 1340. The working principle of this apparatus is to perform several cycles of cell filling/expulsion of helium, and it is applicable for a wide range of μm-cm sized samples. The sample volume was determined by measuring the pressure change of helium and the volume of helium into the expansion cell after sample filling.

The volume of sample cell was regularly calibrated using calibration standards (e.g., steel balls) to ensure a reproducibility of ±0.01%. With the specified sample weight, true density was easily calculated. More details of the helium pycnometry density measurement are presented elsewhere (Viana et al., 2002).

3.3.6. Gas diffusion chamber method

The diffusion coefficient is governed by the pore structure (geometry and connectivity) of the diffusive pathways. The gas diffusion process and diffusivity measurement through packed non-consolidated samples using two-cell diffusion chamber apparatus was well described by Rolston & Moldrup (2002). All six rock samples, with six different particle sizes, were used in this work to achieve the research objectives. The samples were first placed into a core holder on the top of diffusion chamber (Fig. 1). The core holder and diffusion chamber were isolated from each other by a sliding metal plate, and the diffusion chamber was purged with nitrogen gas to remove all oxygen. Then the metal slide was opened, allowing the oxygen-containing air above and within the sample holder to diffuse into the diffusion chamber from both internal pores within particles and the space between particles (Fig. 1). The oxygen concentration inside the chamber is monitored by an oxygen sensor collected to a Campbell CR1000 datalogger, following the procedures reported by Peng et al. (2012). The oxygen diffusion coefficient was then analyzed based on the unsteady-state method of Currie (1960) and Rolston & Moldrup (2002). The relative oxygen concentration in the diffusion chamber C_r can be calculated as:

$$C_r = \frac{C_t - C_S}{C_0 - C_S} = \sum_{n=1}^{\infty} \frac{2h\, exp(-D_P \alpha_n^2 t/\emptyset)}{L(\alpha_n^2 + h^2) + h} \tag{3}$$

where C_0 is the initial oxygen concentration, C_t is the concentration at time t, C_S is the atmospheric oxygen concentration, L is the sample length, $h = \emptyset / \alpha$ where $\emptyset$ and α are air-filled pore space (both inter- and intra-granular pores) percentage and the chamber volume per area, respectively, and α_n is the positive root of $(\alpha_n L)\tan(\alpha_n L) = hL$. The terms for n ≥ 2 are considered negligible with respect to the first term when the time is greater than zero, and Eq. 3 is then reduced to Eq. 4,

$$C_r = \frac{2h\, exp(-D_P \alpha_1^2 t/\emptyset)}{L(\alpha_1^2 + h^2) + h} \tag{4}$$

Take the natural logarithm of both sides of Eq. 4 to obtain

$$lnC_r = ln\frac{2h}{L(\alpha_1^2 + h^2) + h} - \frac{D_p \alpha_1^2}{\emptyset} \cdot t \tag{5}$$

Thus, a negative linear relationship between lnC_r and t, with the slope of $-D_P \alpha_1^2 t/\emptyset$, is obtained, in which pore or effective diffusion coefficient D_P can be calculated with known α_1 and $\emptyset$. A penetration of oxygen into the diffusion chamber was caused by the oxygen concentration difference between the higher oxygen-containing atmosphere and the relatively oxygen-free diffusion chamber. Crushed rocks, with both intra- and inter-particle pore space, instead of non-aggregated soils with negligible intra-particle porosity, were used in our study to evaluate the contribution of intra-particle diffusivity implicated by pore connectivity. Since a molecule diffusing through the packed granular rocks could travel via the complex geometries both within the intra-particle pore network and the void space between particles, the diffusion process is controlled by the combination of inter- and intra-particle diffusion. Unlike inter-particle diffusion, intra-particle diffusion is slower with tortuous pathways inside the particles. Therefore, a prediction of the intra-particle diffusion coefficient will shed light on the internal geometries of crushed rock samples.

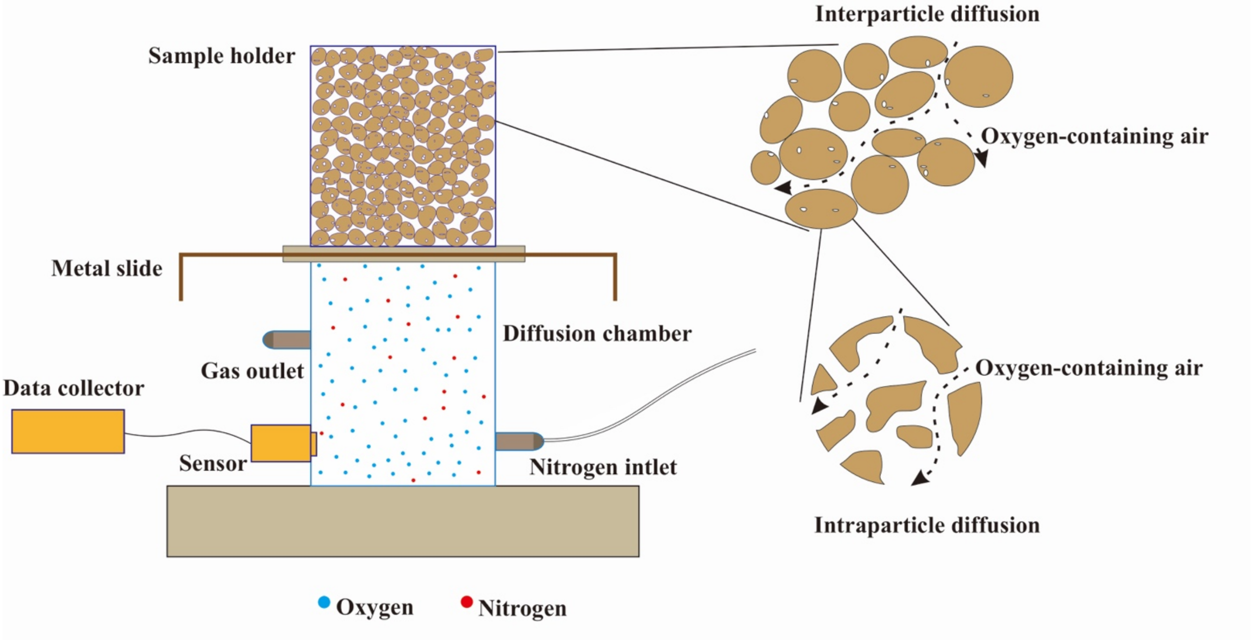

Figure 1. Experimental setup and schematic diagram of gas diffusive transfer in a packed bed of granular samples.

Assuming that the experimentally observed data are the sum of diffusion from two separate inter- and intra-particle pathways, the C_t is the sum of $C_{t-inter}$ and $C_{t-intra}$ (Eq. 6). Then, according to Eq. 3, the relative intra-particle oxygen concentration $C_{r-intra}$ at each time can be represented with Eq. 7:

$$C_t = C_{t-inter} + C_{t-intra} \tag{6}$$

$$\begin{aligned} C_{r-intra} &= \frac{C_{t-intra} - C_s}{C_0 - C_s} = \frac{C_t - C_{t-inter} - C_s}{C_0 - C_s} \\ &= \frac{C_t - C_s}{C_0 - C_s} - \frac{C_{t-inter} - C_s}{C_0 - C_s} + \frac{C_s}{C_0 - C_s} \end{aligned} \tag{7}$$

where $C_{t-inter}$ and $C_{t-intra}$ are the oxygen concentrations from inter-particle and intra-particle diffusion at time t, respectively.

When C_0 for oxygen concentration is close to 0, as the diffusion chamber initially was purged with nitrogen, $\frac{C_s}{C_0-C_s}$ can be reduced to -1. Thus, at time t, the $C_{r-intra}$ is:

$$C_{r-intra} = \frac{C_t - C_s}{C_0 - C_s} - \frac{C_{t-inter} - C_s}{C_0 - C_s} + \frac{C_s}{C_0 - C_s} = C_r + C_{r-inter} - 1 \qquad (8)$$

where $C_{r-inter}$ and $C_{r-intra}$ are the relative concentrations from inter- and intra-particle diffusion at time t, respectively.

Since granular samples involved in this study contain both inter- and intra-particle pathways, an independent and experimental analysis of inter- or intra-particle diffusion of those samples is difficult. A crushed solid quartz method was then utilized in this study to quantify the inter-particle diffusion of crushed porous rock samples with intra-particle pore space and diffusion. This single-crystal solid quartz sample is independently shown to contain no inner pore space (with a measured porosity 0.011± 0.009% by water immersion porosimetry), with the same size fractions of crushed particles as rock samples being utilized to obtain the inter-particle diffusivity. Thus, if the oxygen concentration is measured at two times Δt apart, Eq. 8 can be transformed into Eq. 9 at time (Fig. 3).

$$\Delta C_{r-intra} = \Delta C_r - \Delta C_{r-quartz} \qquad (9)$$

where ΔC_r, $\Delta C_{r-intra}$, and $\Delta C_{r-quartz}$ are the relative oxygen-concentrations increment from total, intra-particle, and inter-quartz particle diffusion at a unit time, respectively.

To obtain ΔC_r, we differentiate the variables on both sides of Eq. 5:

$$\frac{1}{C_r}dC_r = -\frac{D_p\alpha_1^2}{\emptyset}\cdot dt \tag{10}$$

$$\Delta C_r = dC_r = \left(\frac{-D_p\alpha_1^2}{\emptyset}\right)\cdot C_r dt \tag{11}$$

Similarly, $\Delta C_{r-quartz}$ can be calculated:

$$\Delta C_{r-quartz} = dC_{r-quartz} = \left(\frac{-D_{p-quartz}{\alpha_1}^2}{\emptyset_{qtz}}\right)\cdot C_{r-quartz}dt \tag{12}$$

where f_{qtz} is the air-filled pore space percentage in the packed bed of quartz grains.

Consequently, the sum of $\Delta C_{r-intra}$ can provide us with the intra-particle diffusion profile of oxygen tracer for the granular rock sample：

$$C_{r-intra} = \int \Delta C_{r-intra}dt \tag{13}$$

Once $C_{r-intra}$ is obtained, the intra-particle oxygen diffusion coefficient can be calculated based on Eq. 5 (Currie, 1960; Rolston & Moldrup, 2002).

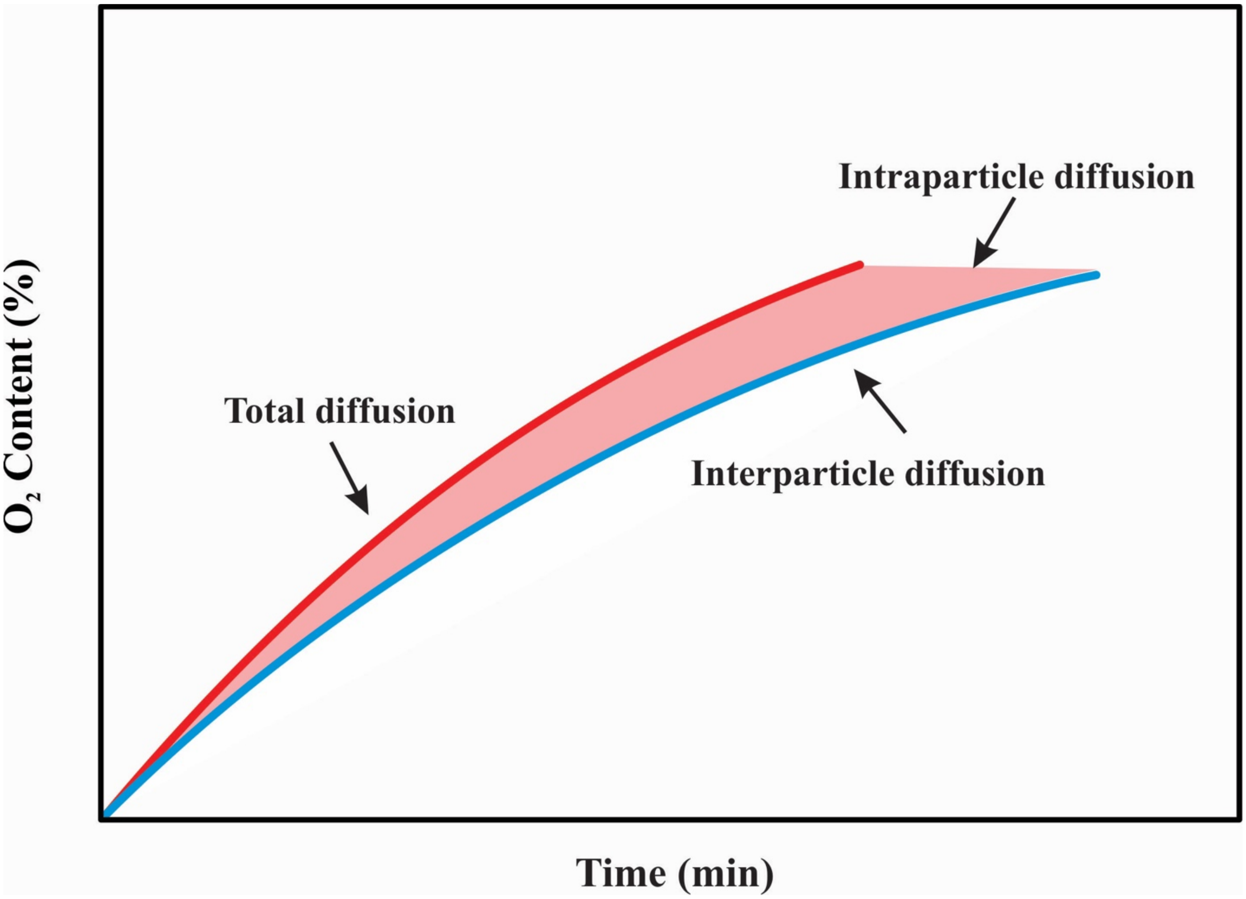

Figure 2. Schematic oxygen signals over time in diffusion tests of packed porous and granular samples, with the red and blue lines representing the data from a porous rock sample and solid quartz, respectively.

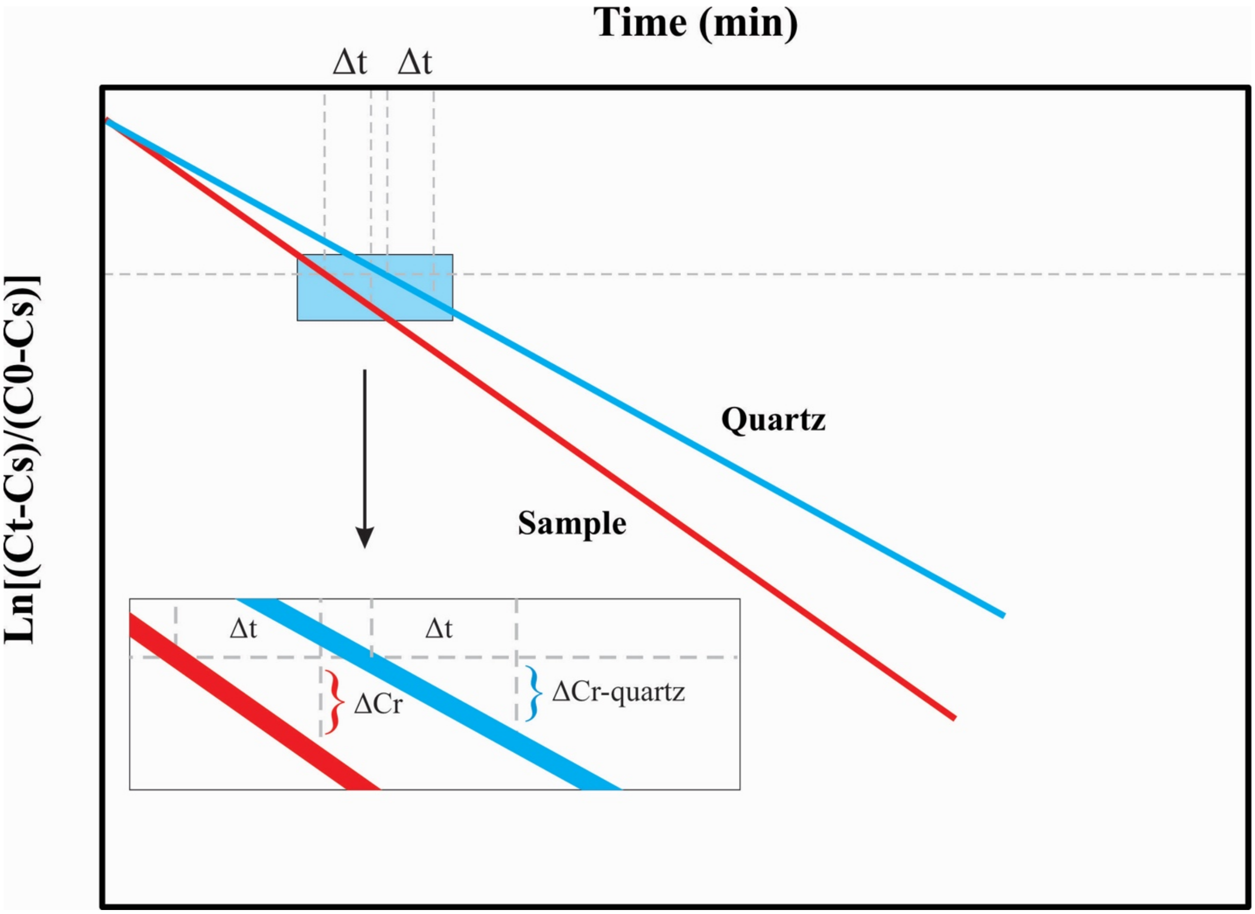

Figure 3. Linear relationships of $ln\ C_r$ and $ln\ C_{r-quartz}$ vs. time as well as corresponding increase of C_r and $C_{r-quartz}$ at time Δt.

In this study, six rock samples with six different particle sizes were oven-dried at 60^{o}C for two days and packed in a PVC cylindrical sample holder (3.5 cm in inner diameter and 4.0 cm in length) for gas diffusion analyses. To limit the heterogeneous compaction effect, a packing method with multiple layers was used, and samples were shaken well at each layer when the sample was poured into the holder.

3.4. Results and Discussion

3.4.1. Mineralogy

As shown in Table 3, Israel white chalk, Israel gray chalk, and Japan mudstone samples contain significant amounts of clay minerals, while Edwards limestone, Wyoming dolostone, and Grimsel granodiorite are samples with low clay contents. Specifically, similar clay contents at around 30 ~ 40% by weight are found in Israel gray chalk and Israel white chalk, containing 4.4% and 37.9% of illite, respectively. In Japan mudstone, clay minerals are dominated by illite and kaolinite at 12.3% each. No clay minerals were detected in Edwards limestone or Grimsel granodiorite, and few are in Wyoming dolostone. Three carbonate rocks are composed of high calcite concentrations: 99.6% in Edwards limestone, 61.5% in Israel white chalk, and 65.8% in Israel gray chalk. In addition, Grimsel granodiorite exhibits high feldspar contents, with 49.5% weight percent albite and 12.5% anorthite.

3.4.2. Grain size distribution and pore structure characteristics

The measured grain size distribution after ball milling for each sample is plotted in Fig. 4. The results illustrate that Edwards limestone and Grimsel granodiorite can be classified as being well-graded with uniformity coefficients Cu of 27.2 and 14.6, respectively; this also indicates that the pore structure of these two samples (the "heterogeneous" group) could be likely heterogeneous. On the other hand, the relatively homogeneous pore structure of Israel gray chalk, Israel white chalk, Wyoming dolostone, and Japan mudstone (the "homogeneous" group) can be related to their poorly-graded grain sizes. Curvature coefficients C_c of these four rock samples are equal to or less than 1, and the C_u values are 6.4, 7.86, 6.4, and 1.51, respectively (Table 4).

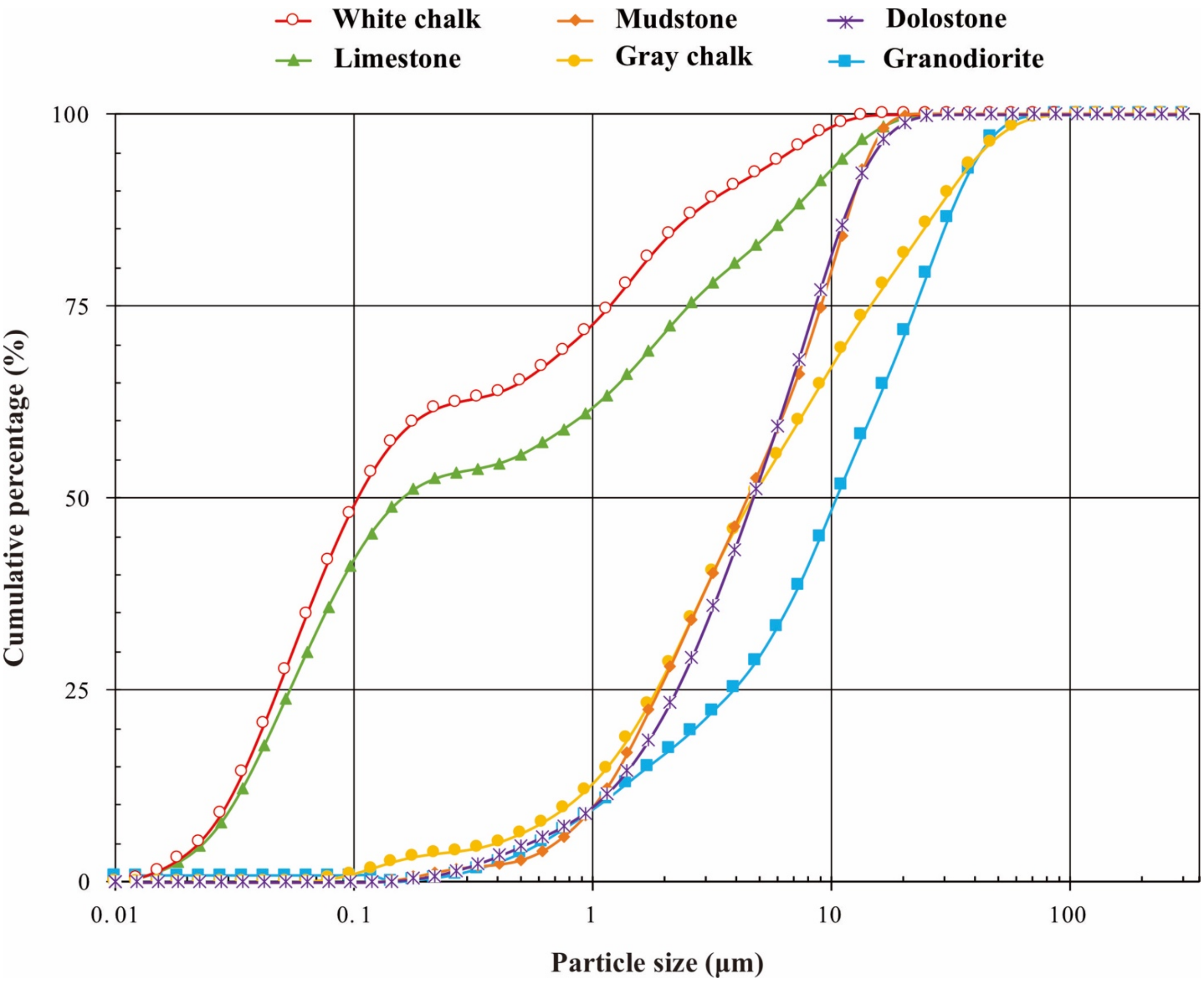

Figure 4. Grain size distribution of ball-milled powders from six rock samples.

Fig. 5 shows the capillary pressure curves obtained from the MIP tests for 1-cm cubes of five rocks (data are not available for Wyoming dolostone). The hysteresis loop in the intrusion/extrusion cycles of our samples indicated that mercury entrapment occurred and pore systems in these natural rocks were heterogeneously distributed (Kaufmann et al., 2009; Plötze & Niemz, 2011). Fractal dimensions obtained from MIP (Table 5) show that Edwards limestone and Grimsel granodiorite display higher entire fractal dimension values, 2.37 and 2.34, respectively, indicating that the pore throat structure for these two samples of "heterogeneous" group are complex and heterogeneous, which is also consistent with the grain size distribution analyses. Compared to Edwards limestone and Grimsel granodiorite, Israel white chalk, Israel gray chalk, and Japan mudstone (the "heterogeneous" group) have lower fractal dimension values of 2.23, 1.82, and 1.89, correspondingly, suggesting relatively homogeneous pore throat structure for these four samples.

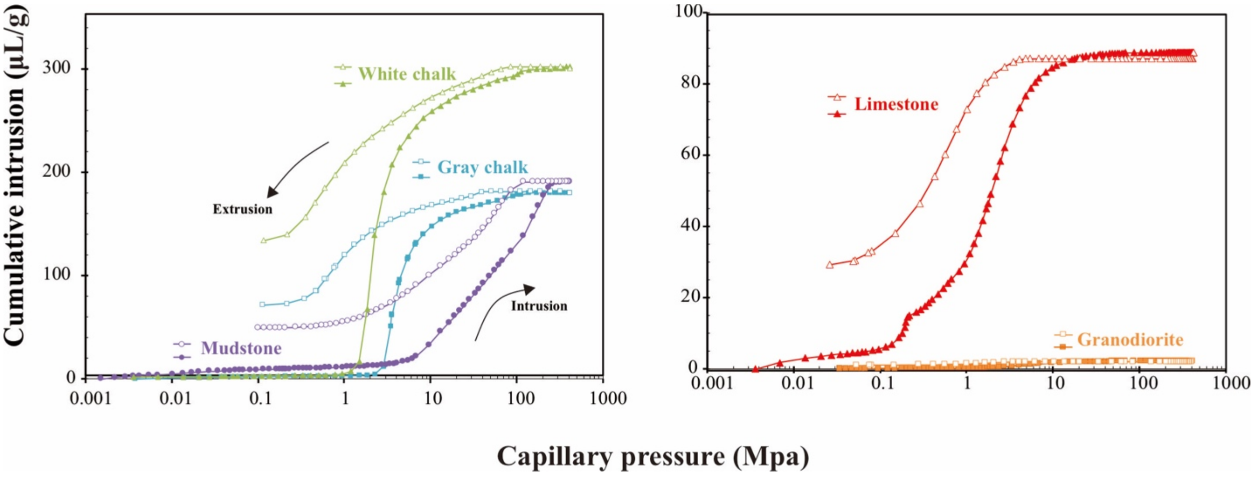

Figure 5. Mercury intrusion (solid symbols) and extrusion (open symbols) curves for five rock samples.

3.4.3. Effective porosities for rock samples at different particle sizes

Consistent with grain size distribution and MIP analyses, in the "heterogeneous" group (Edwards limestone and Grimsel granodiorite) a noticeable increase in intra-particle porosity from coupled bulk-particle densities is observed as the particle size decreases. However, four other rocks in the "homogeneous" group (Israel gray chalk, Israel white chalk, Wyoming dolostone, and Japan mudstone) exhibit a much smaller porosity change with crushed particle size fractions (Fig. 6a). The Edwards limestone sample used in this study was reported to have a highly heterogeneous pore geometry (Johannesen et al., 2007). The mineral and structural heterogeneity of Grimsel granodiorite also has been reported in previous works (Sammaljärvi et al., 2012; Voutilainen et al., 2017). The increase in effective porosity reflects the increase in accessibility to various regions of the pore space as a result of particle size reduction, resulting in the liberation of “isolated” pores and better connectivity (Zhao et al., 2021); due to the strong heterogeneity and poorly-connected pore space, such sample size-dependent effect of effective internal porosity is apparent from the different crushed particle size fractions used in this study.

On the other hand, samples, including white chalk, gray chalk, and dolostone, are more related to the “homogeneous” group and have relatively uniform pore structures. For these “homogeneous” samples, the crushed rock has already reached a critical value of representative elementary volume (REV) in a smaller volume (Shah et al., 2017), which is below the least tested length of 75 μm in this work. The smaller relative porosity change in the chalk samples is in agreement with the results reported by Vik et al. (2013) and Zhao et al. (2021). As a result, the petrophysical property of Israel chalks varies much less with the particle size range and even can be treated as “homogeneous” at these observational scales.

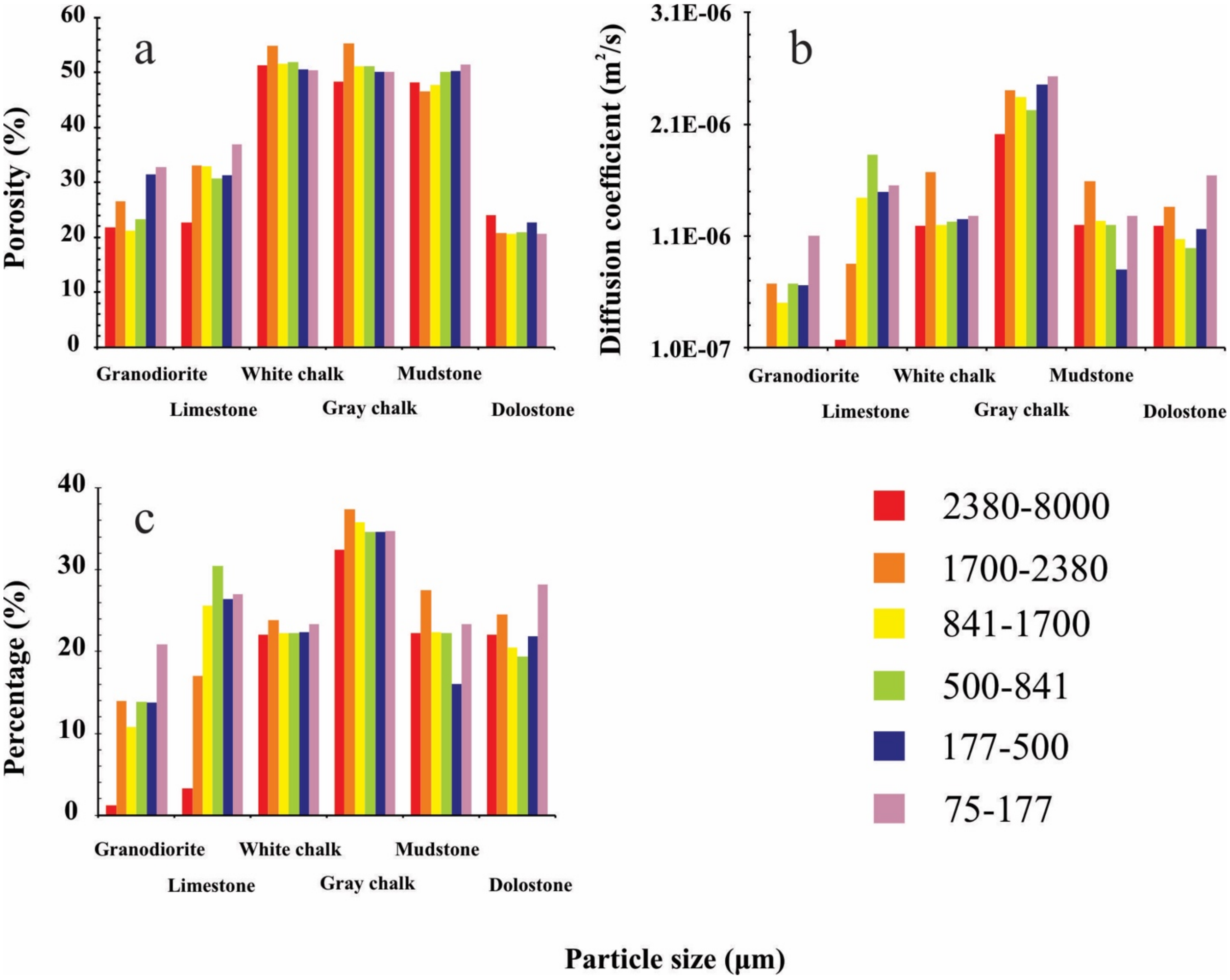

Figure 6. Calculated porosity, intra-particle diffusion coefficient, and the contribution percentage of intra-particle diffusion for six rock samples with six particle sizes (µm).

Normally, an increase in helium porosity of crushed organic-rich and deep mudstone has been observed in previous particle size-effect studies (Tinni et al., 2012; Ma et al., 2014). However, in our work, the Japan mudstone sample came from the Wakkanai Formation which is composed of typically homogeneous siliceous mudstone at a depth of 358 m (Ishii et al., 2011; Aoyagi & Ishii, 2019); therefore, the resultant particle porosities are relatively constant in the range of 75-8000 µm. Hu et al. (2021) reported the dramatic difference in pore connectivity between shallow and deep mudstone, as the organic matter-rich and deep mudstones are subjected to additional maturation process to alter the pore structure and exhibit poor pore connectivity as compared to the compaction and diagenesis of shallow mudstones. The Wyoming dolostone sample is also "homogeneous" with mostly the presence of intercrystalline pore space (Westphal et al., 2004) and displays stable physical properties across the particle size fractions. To summarize, at the observational scales of 75-8000 μm, Edwards limestone and Grimsel granodiorite (the "heterogeneous" group) are heterogeneous porous media, showing scale-dependent porosities, whereas white chalk, gray chalk, dolostone, and shallow mudstone are more of a homogeneous type, and the particle size has less effect on the crushed internal porosities of these four rocks.

3.4.4. Intra-particle gas diffusion

The gas diffusion test is a compelling physical transfer approach to understanding pore connectivity and tortuous pathways of natural rocks. Diffusion results show a notable tendency of increasing intra-particle diffusion coefficient and its proportion with the decrease of particle size in "heterogeneous" Edwards limestone and Grimsel granodiorite (Fig. 6b-c; Table 6). The proportion of intra-particle diffusion in the whole diffusion process of these two samples increases from 3.21% to 34.81%, and 1.21% to 20.91%, respectively, from large (2380-8000 μm) to small (75-177 μm) particle size fractions. It is reported that the heterogeneous Edwards limestone commonly contains intercrystalline pores and micropores as well as larger pores (Johannesen et al., 2007; Yoo et al., 2019). The larger diffusion coefficients in smaller-sized particles are attributed to the opening of intercrystalline pathways in Edwards limestone. Since the granodiorite sample came from the Grimsel Test Site in Switzerland, which has been used as low permeability and heterogeneous materials (David et al., 2018; Schneeberger et al., 2019), the diffusivity of Grimsel granodiorite is the lowest (Table 6) due to its low matrix permeability and poor pore connectivity (Kc et al., 2019).

Israel white chalk and Israel gray chalk (Whitthueser et al., 2000), have similar porosities across the whole range of particle sizes, and the intra-particle diffusion coefficients increase with the decreasing particle sizes. Notably, the gray chalk particles exhibit a higher diffusivity than the white chalk (nearly twice as great; Table 6; Fig. 6b). Therefore, greater pore connectivity is expected within gray chalk. The intrafossil pore space (~3 μm) observed from the SEM images in white chalk is mainly within chalk coccoliths rings, which could provide limited connected pore space (Figs. 7A-B). However, abundant hollow internal chambers (>30 μm) in foraminifera were widely present in gray chalk (Figs. 7C-D). These foraminifera shells could provide ideal effective and connected pore space for mass transfer. The median pore-throat size of white chalk obtained from MIP tests is 0.42 μm, which is slightly larger than that of gray chalk (0.39 μm). These two chalk samples, with similar porosity but displaying different gas diffusion behavior, illustrate the importance of the pore structure effect on mass transport. This observation also implies that a more rapid mass transfer behavior can be achieved with better pore connectivity (the topological attribute of pore structure), even though those samples exhibit similar values of porosities.

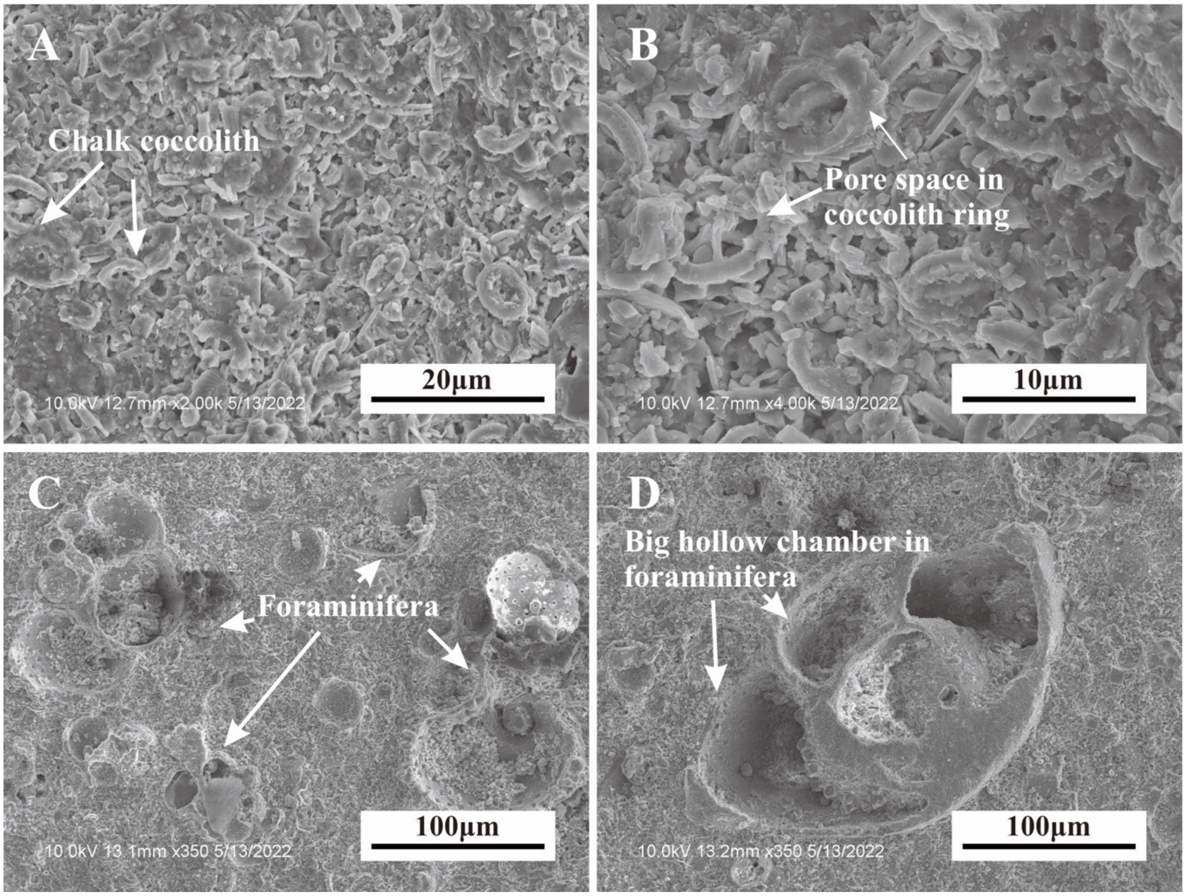

Figure 7. SEM observations of two Israel chalk samples: (A). Gathering of chalk coccolith, white chalk; (B) Pore space (~3 μm) in coccolith ring, white chalk; (C) Cluster of foraminifera, gray chalk; (D) Hollow internal chambers (>30 μm) in multi-chamber.

In contrast, the intra-particle diffusion coefficients of crushed Japan mudstone and Wyoming dolostone remain roughly constant over the tested ranges of particle sizes (Fig. 6b). The gas diffusion run on a monolithic Japan mudstone sample (1 cm^3 cube) exhibits a smaller (3.11×10^{-7} m^2/s; by a factor of ~4) diffusion coefficient than the intra-particle diffusion coefficient of crushed Japan mudstone (Table 6); this indirectly verifies the versatile approach of using solid quartz grains to experimentally and theoretically obtain the intra-particle diffusivity for a wide range of natural rocks with different pore structure characteristics. These “homogeneous,” within the observational scales of 75-8000 μm, samples reach the REV quickly at smaller sample size, and the crushed particle sizes in our work are regarded to be already above the length scale of REV. In other words, the pore structure of these samples would likely be similar for six particle sizes and then the diffusion contribution from the intra-particle pathways is constant, for the effective intra-particle diffusivity to be similar in the same magnitude of 10^{-6} m^2/s. In addition, pore connectivity may dominate intra-particle diffusion behavior: Grimsel granodiorite has similar porosity to Wyoming dolostone, but with its poor pore connectivity it has lower intra-particle diffusivity than Wyoming dolostone.

Table 3. Mineral composition and clay-minerals contents for six rock samples.

Sample name	Mineralogical composition in weight (%)													Clays
	Quartz	Plagionite	Albite	Anorthite	Chlorapatite	Pyrite	Dolomite	Calcite	Biotite	Muscovite	Kaolinite	Montmorillonite	Illite	
Grimsel granodiorite	20.0	3.4	49.5	12.5	n.d.	n.d.	n.d.	n.d.	2.0	12.7	n.d.	n.d.	n.d.	0.0
Edwards limestone	0.4	n.d.	n.d.	n.d.	n.d.	n.d.	n.d.	99.6	n.d.	n.d.	n.d.	n.d.	n.d.	0.0
Israel white chalk	0.6	n.d.	n.d.	n.d.	n.d.	n.d.	n.d.	61.4	n.d.	n.d.	n.d.	0.1	37.9	38.0
Israel gray chalk	0.5	n.d.	n.d.	n.d.	n.d.	n.d.	2.3	65.8	n.d.	n.d.	n.d.	27.1	4.4	31.5
Japan mudstone	9.6	28.4	23.8	6.0	2.9	3.3	n.d.	n.d.	n.d.	n.d.	12.3	1.5	12.3	26.1
Wyoming dolostone	n.d.	n.d.	n.d.	n.d.	n.d.	n.d.	85.5	12.6	n.d.	n.d.	n.d.	1.8	n.d.	1.8

Note: n.d.= not detected

Table 4. Grain size distribution parameters

Sample ID	Particle diameter (μm)				Uniformity parameters	
	d25	d50	d75	d95	C_u	C_c
Grimsel granodiorite	3.95±0.00	11.08±0.00	25.27±0.00	70.8±0.00	14.59	1.86
Edwards limestone	0.06±0.00	0.18±0.00	2.62±0.00	70.8±0.00	27.08	0.19
Israel white chalk	0.05±0.00	0.12±0.00	1.41±0.00	70.8±0.00	6.4	0.54
Israel gray chalk	2.13±0.00	5.23±0.64	16.97±3.48	70.8±0.00	7.86	1.00
Japan mudstone	31.06±0.00	46.91±0.00	57.65±0.00	70.8±0.00	6.40	0.81
Wyoming dolostone	2.62±0.00	4.86±0.00	9.01±0.00	70.8±0.00	6.40	1.23

Table 5. Fractal dimensions of pore throat structure obtained from MIP tests.

Sample ID	Mesopores (100-1000 nm)		Transitional pores (10-100 nm)		Micropores (2.5-10 nm)		Entire pores (2.5-1000 nm)
	D_1	R^2_1	D_2	R^2_2	D_3	R^2_3	D
Grimsel granodiorite	2.9515	0.9482	2.2293	0.9486	2.1136	0.9084	2.3431
Edwards limestone	2.9360	0.8683	2.5835	0.9835	1.1121	0.6081	2.3711
Israel white chalk	2.9962	0.3440	2.1342	0.9693	1.0599	0.8738	2.2250
Israel gray chalk	2.9975	0.9586	1.9106	0.9746	1.1922	0.8338	1.8209
Japan mudstone	2.9915	0.9611	2.9294	0.7034	1.4723	0.6998	1.8916

Table 6. Summary of intra-particle diffusion coefficient (m^2/s) and its contribution to the total diffusion for six rock samples.

Particle size (μm)	Grimsel granodiorite		Edwards limestone		Israel white chalk		Israel gray chalk		Japan mudstone		Wyoming Dolostone	
	Diffusivity (m^2/s)	Proportion (%)	Diffusivity (m^2/s)	Proportion (%)	Diffusivity (m^2/s)	Proportion (%)	Diffusivity (m^2/s)	Proportion (%)	Diffusivity (m^2/s)	Proportion (%)	Diffusivity (m^2/s)	Proportion (%)
2380-8000	5.07×10^{-8}	1.21	1.76×10^{-7}	3.28	1.19×10^{-6}	22.09	2.10×10^{-6}	32.40	1.20×10^{-6}	22.24	1.19×10^{-6}	22.09
1700-2380	6.75×10^{-7}	14.00	8.55×10^{-7}	16.98	1.67×10^{-6}	23.8	2.40×10^{-6}	37.41	1.59×10^{-6}	27.54	1.36×10^{-6}	24.49
841-1700	5.07×10^{-7}	10.78	1.44×10^{-6}	25.61	1.20×10^{-6}	22.22	2.34×10^{-6}	35.80	1.24×10^{-6}	22.36	1.07×10^{-6}	20.52
500-841	6.77×10^{-7}	13.89	1.83×10^{-6}	30.45	1.23×10^{-6}	22.26	2.23×10^{-6}	34.62	1.20×10^{-6}	22.24	9.96×10^{-7}	19.43
177-500	6.60×10^{-7}	13.73	1.49×10^{-6}	26.38	1.25×10^{-6}	22.39	2.46×10^{-6}	34.65	1.00×10^{-6}	19.25	1.16×10^{-6}	21.87
75-177	1.10×10^{-6}	20.91	1.55×10^{-6}	27.01	1.28×10^{-6}	23.36	2.53×10^{-6}	34.73	1.28×10^{-6}	23.36	1.64×10^{-6}	28.23

3.5. Summary

Through integrated pore structure studies of gas for six natural rocks with six different sample sizes, we conclude that a smaller sample scale could have positive effects on pore connectivity for relatively heterogeneous rocks as well as on mass transport properties. For comparatively homogeneous geological media, the change of pore connectivity in various sample sizes is relatively small, indicating relative independence of physical and chemical transport properties on particle sizes. More…

CHAPTER 4. AQUEOUS-PHASE CHEMICAL SORPTION AND CONTROLLING FACTORS

4.1. Introduction

Ionic sorption and transport are considered chemical indicators for evaluating the pore connectivity and chemical retention of natural rocks. The sorption capacity of ions onto adsorbents owing to their ability of selectively binding chemical molecules has been well documented for industrial materials (He et al., 2011). Surface area, pore structure, chemical characteristics, and initial concentration of adsorbate have long been recognized as parameters in controlling ionic sorption and transport in various engineering and geological materials (Chang & Lenhoff, 1998; Li et al., 2012; Punyapalakul et al., 2013; Wang et al., 2015; Hong et al., 2019). Moreover, due to the specific physical structure and chemical properties, mineral compositions vary in their sorption capacities to different ions. Therefore, in this work, six geologically different rocks with six different particle sizes, introduced in Chapter 3, were chosen. Subsequently, a sequence of batch sorption experiments was carried out, utilizing a range of tracer chemicals, including both anions and cations with non-sorbing and sorbing characteristics. These experiments aimed to evaluate the sorption capacity of these six rock samples. Concentration analyses were performed using inductively coupled plasma-mass spectrometry (ICP-MS), a reliable and highly sensitive technique employed to detect multiple elements of both tracers and intrinsic conponents (Hu et al., 2005; Hu & Mao, 2012).

4.2. Materials

4.2.1. Sample selection

The same set of six natural rock samples (limestone, white chalk, gray chalk, mudstone, dolostone, and granodiorite) used in Chapter 3 were selected for this study. Two chalk samples, white and gray, were used in this work. Most shallow and organic matter-poor mudstones are lithologically homogeneous. The dolostone is homogeneous with respect to its constituent dolomite crystals. In addition, granodiorite is generally composed of feldspars, quartz, and micas with various grain sizes on the order of mm scales.

4.2.1. Sample preparation

These intact rocks from either outcrops or cores were first crushed and sieved under one passing according to ASTM C136-01 (2017), using a stack of stainless sieves with mesh sizes of 0.075, 10.18, 0.5, 0.85, 1.7, and 2.36 mm; therefore, particle sizes of crushed samples range in the sequence of 75-177, 177-500, 500- 841, 841-1700, 1700-2360, and 2360-8000 μm. Consequently, the effects of heterogeneity and particle size on pore structure and mass transport (liquid sorption) behaviors could be evaluated by using these six rock samples at different particle sizes (Table 2).

4.3. Batch sorption method

The batch sorption experiments were carried out using air-dried crushed rock samples under atmospheric conditions and room temperature of 22 ± 0.2°C (ASTM, 2001). A range of anionic and cationic tracers (e.g., Br^- and Cs^+) at 0.01 mM concentrations were used as tracer solution and 1 mM calcium nitrate as an electrolyte solution to represent a dilute groundwater system. Three tracer solution controls (no solid samples) were prepared to allow the assessment of any interaction of tracers with the apparatus (e.g., centrifuge tubes and caps). For each rock specimen, triplicate samples were conducted with tracer solution and duplicate samples with electrolyte solution (no spiked tracer, for assessing the background levels of various tracer elements). The amount of rock and solution was accurately weighted out to be ~0.5 g and 2 mL, respectively, with a relatively large solid:volume ratio being 250 g/L.

Batch sorption experiments were carried out by following procedures similar to methods commonly used in the literature (Karickhoff, 1980; Hu et al., 2005). Briefly, both solid and solution were mixed in 15 mL polyethylene centrifuge tubes for sorption with a reaction time of 24 h irrespective of reaching sorption equilibrium or not (ASTM, 2001), the mixtures were centrifuged at 4,000 revolutions per minute for 10 minutes and then further filtered using 0.25 μm Supor membrane under a gentle vacuum, and 0.5 mL filtrate was then mixed with 2.5 mL 1% high-purity nitric acid for ICP-MS analyses. The sorption ability of each sample for each tracer was calculated from the differences between initial and final concentrations using the following equation:

$$K_d = \frac{(C - C_e)}{C_e} \times \frac{V}{M} \tag{14}$$

where K_d is the adsorption coefficient (mL/g), C and C_e are the initial and "equilibrium" or final concentrations of each tracer (mg/L), respectively. V is the volume (mL) of solution, M is the mass (g) of adsorbent used on a dry basis with the moisture content of air-dry samples obtained from oven drying at 105°C for two days.

A high K_d value suggests higher tracer retention by the crushed rock through sorption and chemical reaction. On the contrary, a low K_d value indicates that a larger amount of the tracer remains in the solution for a higher tracer mobility in the aqueous phase (Veeresh et al., 2003; Shaheen et al., 2012).

4.4. Results and Discussion

4.4.1. Batch sorption results for anionic and cationic tracers

Both anions and cations are widely applied as tracers in studying chemical sorption onto porous media. The batch sorption tests, using six natural rocks in six particle sizes ranges interacting with various inorganic anionic and cationic tracers, were used to assess the magnitude of sorption and identify governing parameters, including the mineral composition, surface area, and pore structure. Analyses of the variance for bromide (Br^-) results show that no noticeable sorption is observed between different samples (Fig. 8). This indicates that anionic bromide is a conservative tracer under the experimental conditions for these samples with a negligible amount of metal (hydro) oxides, in accordance with results presented by many researchers such as Levy and Chambers (1987).

Fig. 8 also presents varying extents of sorption of other anionic tracers. Some sorption of SeO_4^{2-} is related to plagioclase (Li et al., 2018), which consists of albite and anorthite. Grimsel granodiorite, with plagioclase as the dominant mineral (Barnes, 1988) (Table 3), also has a relatively higher SeO_4^{2-} sorption amount, with K_d values ranging from 2 to 4 mL/g. By comparison, the SeO_4^{2-} K_d values of other five rocks are close to 0 mL/g, with no measurable sorption. Fig. 8 also shows that the kaolinite-rich Japan mudstone particles demonstrate a strong sorption capacity for anionic CrO_4^-, as compared to other five rocks. Specifically, K_d values of CrO_4^- for Japan mudstone particles ($\times 10^4$ mL/g) is one order of magnitude higher than those of other rocks ($\times 10^3$ mL/g), which is in good agreement with the high sorption capacity of kaolinite clay, reported by Helios-Rybicka and Wójcik (2012). Similar to CrO_4^{2-}, the anionic but larger Sb^{2-}-complex is quite sorptive in Japan mudstone as well. Our results show the sorption capacities of Sb^{2-}-complex on the Japan mudstone samples (×10^5 mL/g) were much higher (several orders of magnitude) than those on the other five rock samples (×10 mL/g). The high sorption capacity of Sb^{2-}-complex on Japan mudstone is due to its rich content of amorphous iron (principally opal-A) (Fan et al., 2013; Sasamoto et al., 2018; Nishimura et al., 2022).

High sorption of heavy metals, monovalent (Cs^+) and divalent (Ba^{2+}) cations, have been observed for high clay content samples (Israel chalks and Japan mudstone) with K_d values around 100 mL/g and 10000 mL/g for Ba^{2+} and Cs^+, respectively (Fig. 9b). With a predominant presence of K^+ in the interlayer space, illite has been known to strongly sorb Cs^+ from its displacement of K^+ (Bradbury & Baeyens, 2000; Zachara et al., 2002). For low clay content samples (Edwards limestone, Wyoming dolostone, and Grimsel granodiorite), a smaller but still appreciable sorption of Cs^+, with K_d values ranging from 50 to 100 mL/g, was observed (Fig. 9a). Overall, the batch sorption tests provide a cost-effective and broad perspective for the sorption extent of a wide range of chemicals, at different forms, molecular sizes, and reactivities, which are related to mineral components of natural rocks.

Notably, batch sorption coefficients in some tracers may have been detected to a level close to the error bars especially for tracer bromide (Br^-) in Figure 8. These results are considered within experimental errors considering the low averaged batch sorption coefficients values (smaller than 1) for those tracers. In addition, the associated error bars are much lower compared to the observed values for tracers of Ba^{2+} and Cs^+ since the batch sorption coefficients are around several hundred (Figs. 9-10).

4.4.2. Effect of adsorbent particle sizes on chemical sorption

Investigating the performance of natural rocks in relation to their particle size has been an important aspect of sorption process, as arbitrarily used particle sizes are used to describe the sorption contribution of intact rocks (Giammar et al., 2007; Venegas et al., 2007; Li et al., 2019; Tachi et al., 2021), which lead to an uncertainty in evaluating the *in situ* contribution of sorption in waste containment (Hu et al., 2019). A relationship between the particle size and the sorptive capacity has been established: the extent of sorption increases with decreasing particle size, and powder form contains the highest adsorptive capacity (Kara et al., 2007; Raposo et al., 2009; Ikenyiri & Ukpaka, 2016). Our experimental results (Fig. 10) also indicate that sample particle size has an effect on the sorption capacities of several tracers. As the particle size decreases, the sorption capacity of Sm^{3+} and Eu^{3+} increases among Grimsel granodiorite, Japan mudstone, and Wyoming dolostone. For "homogeneous" rocks, stronger sorption capacity in smaller-sized particles stems from the increase of specific external surface area (surface area per unit mass) available for tracer's adsorption (Matsui et al., 2011). Therefore, the external surface areas in smaller-sized Japan mudstone and Wyoming dolostone particles are larger compared to larger-sized particles, with an increasing sorption of Sm^{3+} and Eu^{3+}. In contrast, for "heterogeneous" rocks like Grimsel granodiorite, the increasing sorption can be attributed to both the better connectivity and higher external surface area resulting from the decrease in particle sizes (Sepulveda et al., 2001; Hou et al., 2017; Mastalerz et al., 2017). Both Grimsel granodiorite and Edwards limestone exhibit poor pore connectivity and sample size-dependent accessibility to sorptive pore space, from independent analyses of grain size distribution, MIP, and effective porosity by densities methods (Sections 3.3). However, for a tracer-fluid-rock system with either very strong or weak sorption, this difference in pore accessibility can be overshadowed by a strong chemical sorption effect.

The results also show negligible effects of particle size on the tracer sorption of Edwards limestone and Israel chalks within a particle size ranging from 75 to 8000 μm. This was probably due to the similar maximum sorption capacity of these three rocks. Furthermore, literature results (Stipp et al., 2003; Zavarin et al., 2005) show that Sm^{3+} and Eu^{3+} are adsorbed to calcite, which is the main mineral of Edwards limestone and Israel chalks (Table 3). In general, particles with smaller sizes experience higher surface area, resulting in a higher sorption capacity. Notwithstanding, the sorption capacities of particles from limestone and Israel chalks probably reach the peak when the particle size ranges from 2380 to 8000 μm (the upper range of our size sizes), meaning that the strongly sorbed Sm^{3+} and Eu^{3+} in the solution were completely absorbed. Hence, smaller size particles (less than 2380 μm) with a higher surface area can easily reach the same maximum capacity, and the particle size effect was negligible.

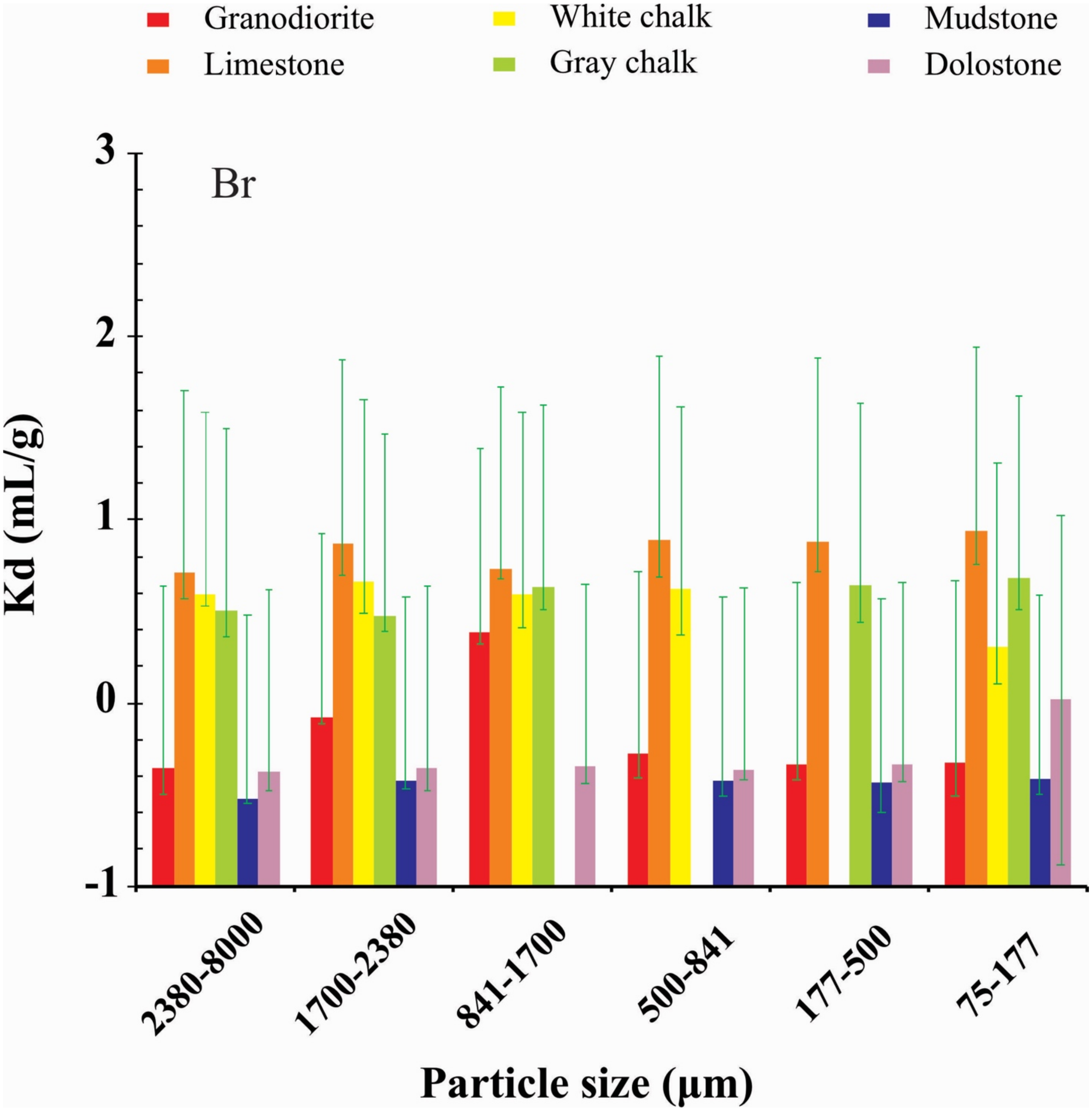
Granodiorite
Limestone
White chalk
Gray chalk
Mudstone
Dolostone
Br
Kd (mL/g)
3
2
1
0
-1
2380-8000
1700-2380
841-1700
500-841
177-500
75-177
Particle size (µm)

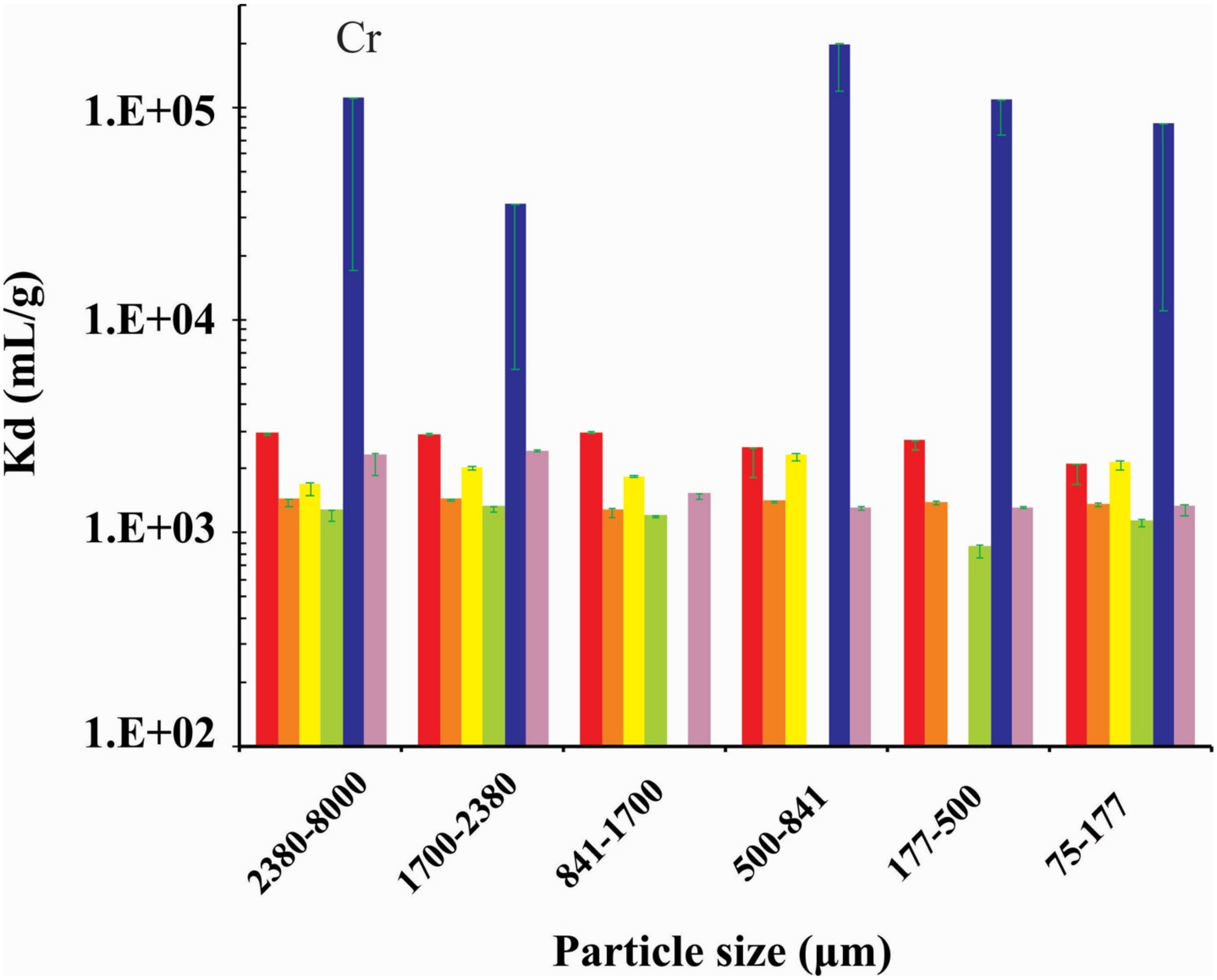
Cr
Kd (mL/g)
1.E+05
1.E+04
1.E+03
1.E+02
2380-8000
1700-2380
841-1700
500-841
177-500
75-177
Particle size (µm)

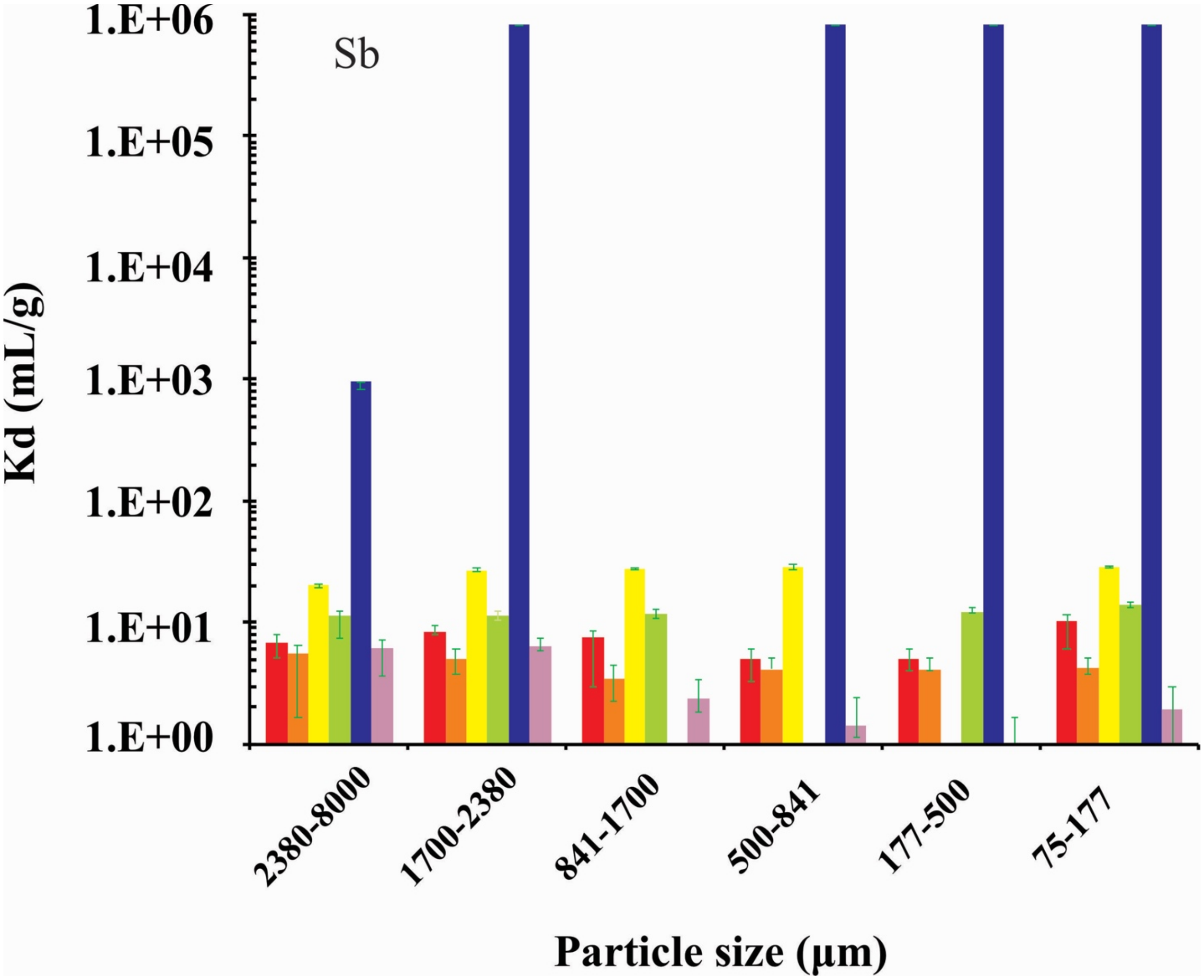
Sb
1.E+06
1.E+05
1.E+04
1.E+03
1.E+02
1.E+01
1.E+00
Kd (mL/g)
2380-8000
1700-2380
841-1700
500-841
177-500
75-177
Particle size (µm)

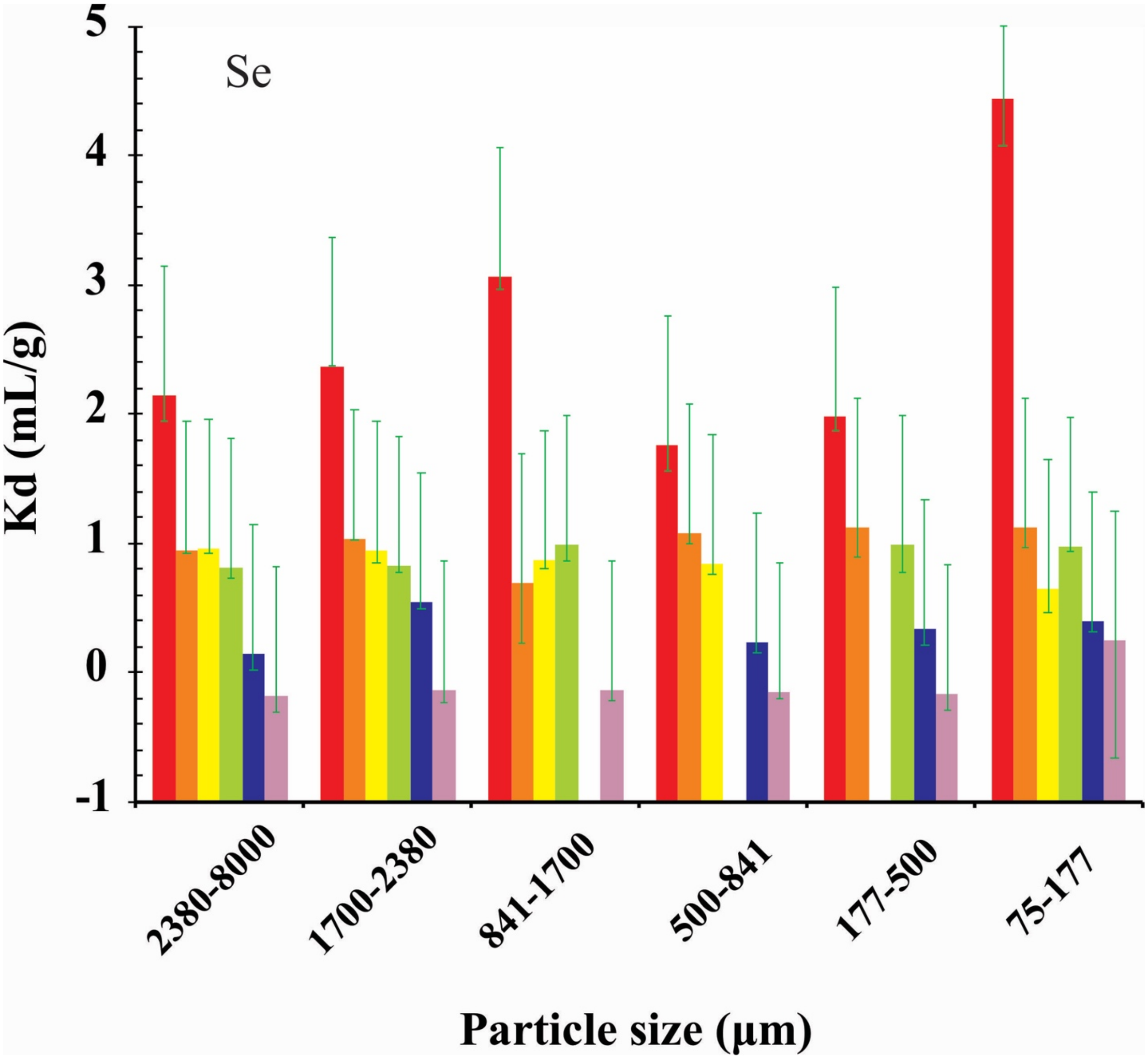

Figure 8. Average batch sorption coefficients K_d (mL/g) values with associated error bars, for anionic tracers of Br^-, SeO_4^{2-}, Sb^{2-}—complex, and CrO_4^{2-} on six different particle sizes of six rock samples. Note: Data of batch sorption for Israel chalk in 177-500 µm, Israel gray chalk in 500-841 µm, and Japan mudstone in 841-1700 µm are not available.

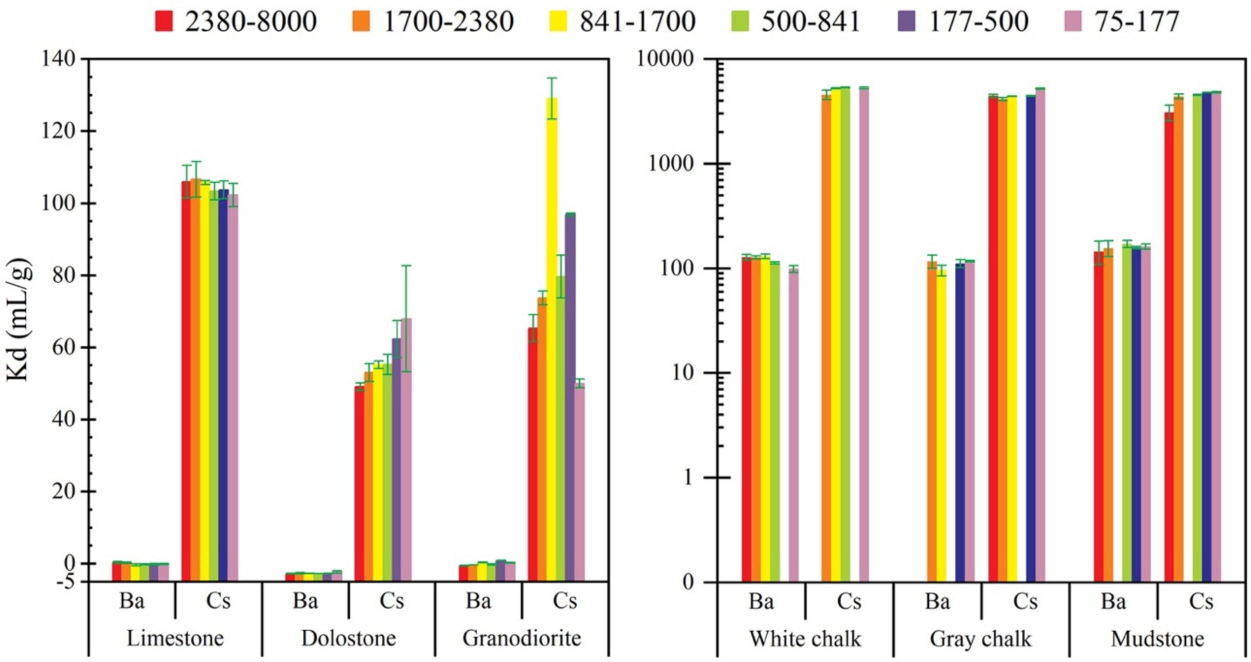

Figure 9. Average batch sorption coefficients Kd (mL/g) values with associated error bars for cationic Ba^{2+} and Cs^{+} on six different size fractions of six rock samples. Note: Data of batch sorption for Israel white chalk in 177-500 µm, Israel gray chalk in 500-84 µm, and Japan mudstone in 841-1700 µm are not available.

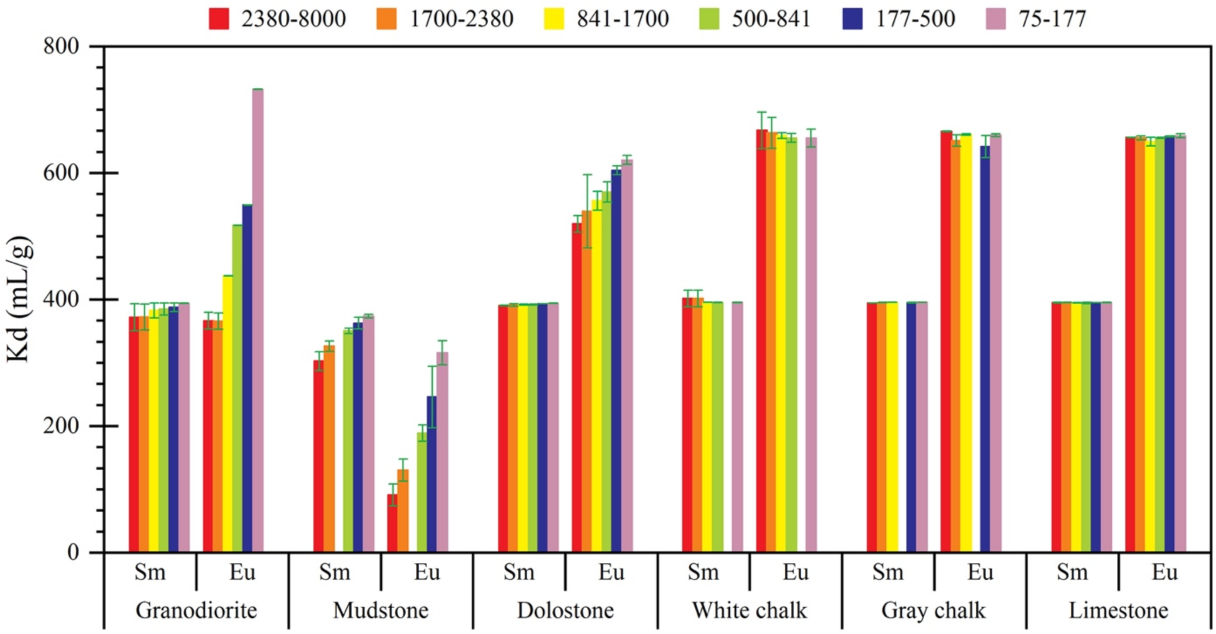

Figure 10. Average batch sorption coefficients Kd (mL/g) values, together with error bars, for cationic Sm^{3+} and Eu^{3+} on six different size fractions of six rock samples.Note: Data of batch sorption for Israel white chalk in 177-500 μm, Israel gray chalk in 500-8841 μm, and Japan mudstone in 841-1700 μm are not available.

4.5. Summary

By conducting comprehensive investigations of pore structures within six distinct natural rock samples across a range of six sample sizes, our findings suggest that in the case of relatively uniform geological materials, alterations in pore connectivity across different sample sizes are rather marginal. Additionally, this study also corroborates the substantial impact of clay minerals and particle size on the ionic sorption capacity of natural rock samples, underscoring their nontrivial contributions。

CHAPTER 5. ARCHIE'S CEMENTATION FACTOR IN POROUS MEDIA

5.1. Introduction

The internal impact of diagenesis on the cementation factor has not been well understood. The cementation factor has a strong relationship with lithological and mineralogical composition of reservoir rocks. Furthermore, it is intertwined with the shape and size of pores and grains (Atkins & Smith, 1961). Table 7 demonstrates that lithology alone does not exclusively govern the cementation factor. Considerably varied cementation factor values have been recorded within the same lithological type. For instance, Porter and Carothers (1970) observed cementation factors ranging from 0.57 to 1.85 in sandstone, while Gomez-Rivero (1976) reported values ranging from 0.02 to 5.67 for sandstone. The objectives of this work are to obtain the cementation factor from gas diffusion tests and Bosanquet formula method and to clarify the diagenetic influences on the cementation factor. Thirteen rock samples with different diagenesis features, including two marbles, four fossiliferous limestones, six mudstones, and one sandstone were selected. A comparative analysis of the cementation factor was analyzed based on gas diffusion and MIP test. The correlations of diffusivity to porosity, permeability, and average pore diameter were analyzed, respectively, as well as the effects of porosity and permeability on cementation factors. In addition, thin section analyses and FE-SEM observations were conducted to clarify the diagenetic contributions to cementation factors. Finally, diagenetic patterns for the thirteen samples were established, and the diagenetic process and microfracture effect on the cementation factor was discussed.

Table 7. Typical ranges of cementation exponent from previous literature.

Lithology	m	References
Mudstone	2.4	Rezaee et al., 2007

	1.55-1.68	Malekimostaghim et al., 2019
	2.32-3.39	Zhong et al., 2021
Sandstone	1.64-2.23	Hill and Milburne, 1956
	1.3-2.15	Carothers, 1968
	0.57-1.85	Porter and Carothers, 1970
	1.2-2.21	Timur et al., 1972
	0.02-5.67	Gomez-Rivero, 1976
	1.64	Adler et al., 1992
	1.39-2.19	Sbiga, 2019
Carbonate rock	1.64-2.10	Hill and Milburne, 1956
	1.78-2.38	Carothers, 1968
	0.39-2.63	Gomez-Rivero, 1976
	1.7-2.3	Schön, 2004
	1.96-2.0	Azar et al., 2008
Metamorphic rock	Increase in the fracturing decreases the cementation factor	Aguilera, 1976

5.2. Materials and Methods

5.2.1. Sample selection and diagenetic stages

Physical characteristics of rocks include depositional texture (grain size, grain shape, and grain packing pattern) and structure (e.g., lamination, cross-stratification, structureless), and diagenetic features (cementation type and distribution, degree of compaction, and dissolution and reprecipitation of minerals) (Dou et al., 2018; Kashif et al., 2019; McKinley et al., 2011; Rushing et al., 2008). Thirteen plug rock samples (2.54 cm in diameter and 3 cm in length) of different lithologies were selected to represent a broad range of physical characteristics for this study. These samples include sedimentary (mudstones, sandstone, and fossiliferous limestone) and metamorphic sedimentary (marble) types (Table 8). These four sedimentary rocks are reservoir rocks of the Pennsylvanian Canyon Group in Texas, Eocene Green River Formation in Wyoming Pennsylvanian Paradox Formation in Utah, and Cretaceous Mancos Formation in Utah. The meta-sedimentary rocks include one dolomite marble and one calcite marble from the Proterozoic Uinta Mountains Group in Utah.

5.2.2. X-ray diffraction (XRD) for mineralogy

The mineralogical compositions of the rock samples were examined using a Shimadzu Maxima X XRD-7000 X-Ray Diffractometer with CuKα radiation. The samples were powered and the fractions less than 75 μm were analyzed. The variation of diffraction angle was from 2° to 70° and the speed was 2°/min. The minerals was identified and the mean percentage of each mineral were determined from the x-ray spectra by using the mineral identification function of Jade 9 software and the whole-pattern empirical peak profile-fitting method. The results of XRD mineralogy analyses for the thirteen samples are presented in Table 9.

5.2.3. Petrographic microscopy and scanning electron microscopy (SEM) imaging

The identification of mineral textures aids interpretation of the diagenetic process (Dravis & Yurewicz, 1985; Mondol et al., 2007; Wang et al., 2017). Blue resin-impregnated thin sections (resin-impregnated at 200 bars and polished to 1 μm) of these 13 samples were studied and photographed with a Leica DM750 P polarized light microscope. Since pore spaces within fine-grained rock samples are difficult to be identified using optical microscopy, in this study, three very fine-grained mudstones were chosen for SEM observations to have a better observation of pore architecture, including intra- and inter-granular pores, organic matter pores, micro-fractures, and the relationship between pore space and minerals. The thin sections used for SEM were manually polished, argon ion-milled using a TORR CrC-100 Sputtering system, Pt-coated, and observed using a Hitachi S-4800 FE-SEM with an operating current at 10 kV.

5.2.4. Mercury intrusion porosimetry (MIP) measurement

MIP is a widely used technique for characterizing geometrical and topological features of rocks, such as porosity, permeability, pore size distribution, tortuosity, and critical pore radius (Gao & Hu, 2013; Hu et al., 2017). Both the diameters of pore throats being invaded by mercury under a specific external pressure and the permeability can be calculated from the MIP data (Washburn 1921; Katz and Thompson, 1986). More details about analysis condition and data interpretation about MIP test can be found in previous studies (Gao & Hu, 2013; Hu et al., 2017) (please refer to 3.3.4 for more details).

5.2.5. Estimation of cementation factor

The cementation factor can be correlated with porosity and diffusivity as expressed in Archie's law, shown in Eq. 15 (Boving & Grathwohl, 2012; Grathwohl, 2012; Peng et al., 2012a; Van Loon & Mibus, 2015; Hwang et al., 2022):

$$D' = D_e/D_a = \emptyset^m \tag{15}$$

where the ratio of D_e/D_a is defined as diffusivity, D' ; D_e is effective diffusion coefficient (m^2/s); D_a is the gas diffusion coefficient in air (m^2/s) with a value of 2.04×10^{-5} m^2/s for O_2 tracer used in our gas diffusion tests; $\emptyset$ is air-filled pore space percentage (%), porosity; and m is cementation factor.

Values of m generally range from 1.5 to 3 for sedimentary rocks (e.g., mudstone, sandstone, siltstone, and limestone) (Borai, 1987; Salem & Chilingarian, 1999; Olsen et al., 2008). However, the m value can be of a broader range in metamorphic rocks due to the presences of vugs and fractures (Bucher & Frey, 2002; Li & Qiang, 2004; Schön, 2011; 2015). According to Eq. 15, once the porosity and diffusion coefficient are known, the cementation factor can be obtained. Consequently, in this study, MIP analyses were used to acquire sample physical properties, such as porosity and tortuosity (Hu et al., 2015). To obtain the diffusion coefficient, two methods, namely the gas diffusion chamber and Bosanquet formula methods, were employed for comparison, with their detailed descriptions being presented below.

5.2.5.1 Gas diffusion chamber method

The gas diffusivity measurement of packed soil samples using a two-cell diffusion chamber apparatus was introduced by Rolston and Moldrup (2002), and Peng et al. (2012a) first conducted gas diffusion tests on 11 intact rocks using test apparatus as illustrated in Fig. 11. In this study, a cylindrical rock sample (2.54 cm in diameter and 3 cm in length) was inserted into a customer-designed PVC cylindrical sample holder (2.7 cm in diameter and 3 cm in length). Microscale gaps between the rock sample and sample holder were smeared with high-vacuum silicone grease to ensure an airtight environment. In brief, the procedure for the diffusion test includes the steps of removing oxygen from the sealed diffusion chamber by purging with nitrogen gas, releasing the oxygen-containing air via diffusion into the chamber through the sample, and continuously measuring the oxygen concentration inside the chamber by an oxygen sensor connected to a Campbell CR1000 data logger. The oxygen diffusion coefficient was then calculated using a non-steady-state method introduced by Currie (1960) and Rolston & Moldrup (2002) (Eq. 16). Combined with Eq. 15, the porosity exponent 'm' can be obtained as the cementation factor.

$$lnC_r = ln\frac{2h}{L(\alpha_1^2 + h^2) + h} - \frac{D_e\alpha_1^2}{\emptyset}\cdot t \tag{16}$$

where C_r is the relative oxygen concentration in the diffusion chamber at time t, L is the length of the sample, h =$\emptyset$ /α with $\emptyset$ and α are air-filled pore space percentage and the volume of the chamber per area, respectively, and α_1 is the positive root of ($\alpha_1 L$) tan ($\alpha_1 L$) = hL. A linear relationship between lnC_r and t, with the slope of $-D_e\alpha_1^2 t/\emptyset$, is derived, in which diffusion coefficient D_e can be calculated if the α_1 and $\emptyset$ are known.

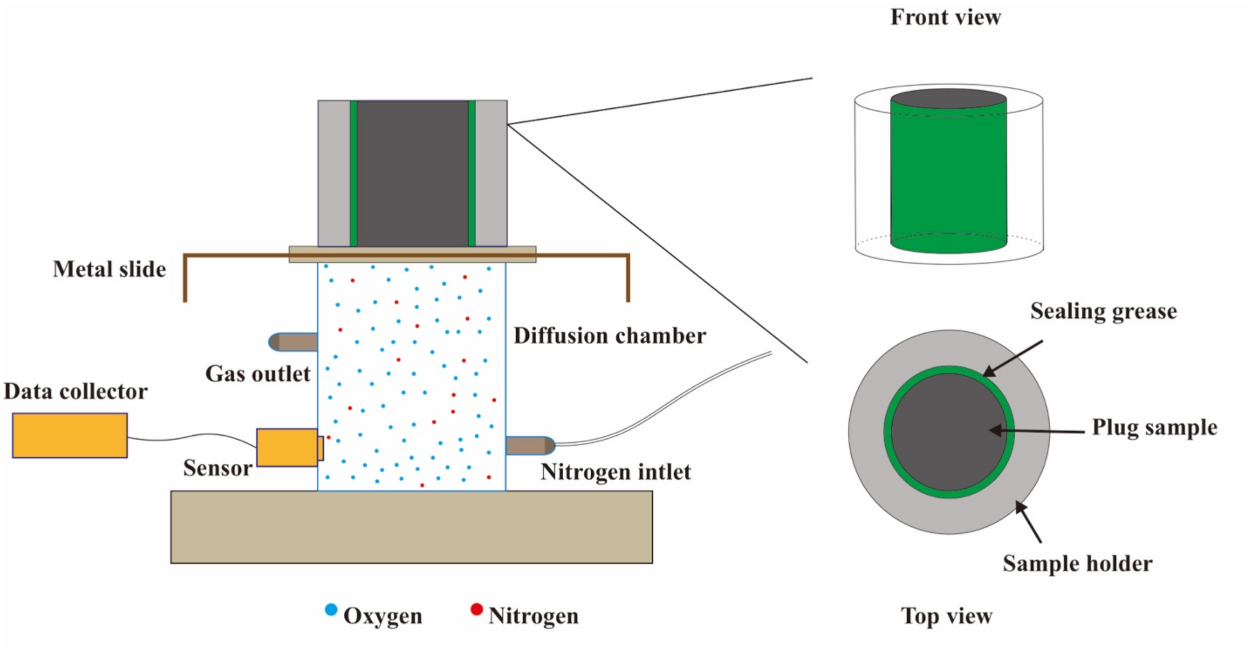

Figure 11. Experimental setup, front and top views of the upper part of the test apparatus.

5.2.5.2 Bosanquet formula method

The average effective diffusivity expression (Eq. 3), namely Bosanquet formula (Pollard et al., 1948), is commonly used to estimate diffusivities for porous geomedia (Reyes et al., 1991;

Kerkhof et al., 1997; Pang et al., 2017; Tokunaga et al., 2017; Yin et al., 2019), with the mean free path of the gas molecules larger than the pore diameter in rock.

$$\frac{1}{D} = \frac{1}{D_a} + \frac{1}{D_{KA}} \tag{17}$$

In this equation, D is the gas diffusion coefficient (m^2/s); D_a is the gas diffusion coefficient in air (m^2/s) (2.04×10^{-5} m^2/s in this case); and D_{KA} is the Knudsen diffusion coefficient (m^2/s).

The Knudsen diffusion coefficient, D_{KA}, which depends on the temperature and molecular weight of tracer gas (O_2) used in the test, and the average pore size of the porous medium, is the key parameter for the Bosanquet formula (Tomadakis et al., 1993). It has been shown that the Knudsen diffusion coefficient can be calculated with the average pore diameter and porosity obtained from MIP data (Cunningham & Williams, 1980; Kast & Hohenthanner, 2000; Mu et al., 2008).

After obtaining D, the effective diffusion coefficient, D_e, can then be calculated from the following Eq. 18 (Evans III et al., 1961; Lu et al., 2014):

$$D_e = \frac{\emptyset}{\tau} D \tag{18}$$

where τ represents the tortuosity factor according to Carniglia (1986), calculated by equation of $\tau = 2.23 - 1.13\emptyset$. Notably, this equation is applicable to rocks with porosity ranging from 0.05 to 0.95, and it assumes that cylindrical diffusion paths predominate in the given porous media (Carniglia, 1986).

In summary, after determining the geometrical and topological parameters of the rocks using MIP data, the Knudsen diffusion coefficient (D_{KA}) and the gas diffusion coefficient (D) (Eq.

17) can be obtained. The effective diffusion coefficient (D_e) can then be calculated using Eq. 18, and finally the cementation factor (m) can be calculated according to Eq. 15.

5.4. Results

5.4.1. Mineralogy

As shown in Table 9, four fossiliferous limestones are composed of high calcite concentrations: 94.4% in CG-1, 58.8% in LF-1, 98.5% in RBU-3, and 74.5% in RBU-4. In addition, five mudstones are enriched in quartz and feldspars, accounting for 74.0% of total minerals in LF-5, 57.1% in RBU-5, 46.3% in MC-4, 45.3% in PW-3, and 20.2% in MK-4. Sample PW-5 and MK-4 have high carbonate content, with 66.2% and 52.1% weight percent calcite, respectively. RBU-1, a sandstone, comprises 70% by weight of quartz and feldspars. Samples DM-2 and DM-5 are both marbles. DM-2 is a dolomitic marble with 59.0% dolomite and 30.0% ankerite, while DM-5 is a calcitic marble with 87.3% calcite content.

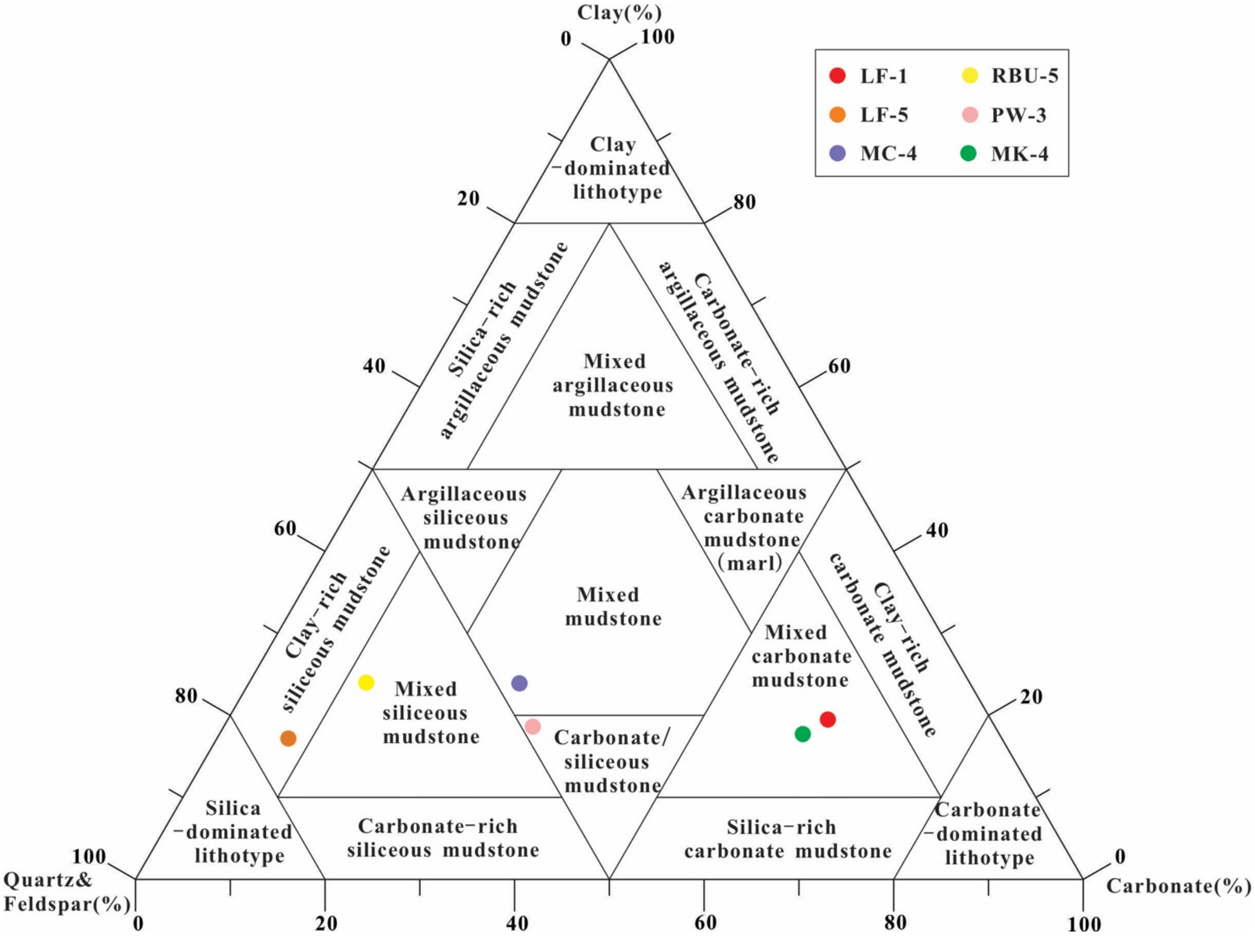

Figure 12. Triangular diagram of mineral compositions for mudstone samples LF-1, LF-5, MC-4, RBU-5, PW-3, and MK-4.

Table 8. Summary of sample source, stratigraphic unit, lithology, and pattern.

Sample name	Sample type	Source	Formation	Depth(m)	Lithology	Cementation group	Derived diagenetic pattern
CG-1	Outcrop	Texas, USA	Canyon	NA	Fossiliferous limestone	One	Strong compaction, strong cementation, and weak dissolution
LF-1	Core	Utah, USA	Mancos	2218.97	Mixed carbonate mudstone	One	Strong compaction, strong cementation, and weak dissolution
LF-5	Core	Utah, USA	Mancos	2312.24	Clay-rich siliceous mudstone	One	Strong compaction, strong cementation, and weak dissolution
RBU-5	Core	Utah, USA	Green river	1770.00	Mixed siliceous mudstone	One	Strong compaction, strong cementation, and weak dissolution
MC-4	Core	Utah, USA	Mancos	2314.96	Mixed mudstone	One	Strong compaction, strong cementation, and weak dissolution
PW-3	Core	Utah, USA	Green river	1685.24	Carbonate/siliceous mudstone	One	Strong compaction, strong cementation, and weak dissolution
PW-5	Core	Utah, USA	Green river	1719.93	Carbonate-dominated lithotype	One	Strong compaction, strong cementation, and weak dissolution
MK-4	Core	Utah, USA	Paradox	1805.66	Mixed carbonate mudstone	Two	Weak compaction, medium cementation and weak dissolution
RBU-1	Core	Utah, USA	Green river	1457.25	Mixed siliceous mudstone	Two	Weak compaction, medium cementation and strong dissolution
RBU-3	Core	Utah, USA	Green river	1459.10	Fossiliferous limestone	Two	Weak compaction, medium cementation and weak dissolution
RBU-4	Core	Utah, USA	Green river	1462.45	Fossiliferous limestone	Two	Weak compaction, medium cementation and weak dissolution
DM-2	Core	Utah, USA	NA	35.36	Dolomite marble	Two	Fracture-matrix
DM-5	Core	Utah, USA	NA	172.21	Calcite marble	Two	Fracture-matrix

Table 9. Mineral compositions of the thirteen rock samples.

Sample ID	Mineralogical composition in weight (%)																		Caly	Carbonate	Quartz+Feldspar
	Quartz	Albite	Dolomite	Calcite	Muscovite	Sidorenkite	Potassium feldspar	Anorthite	Plagionite	Pyrite	Ankerite	Orthobrannerite	Chloritoid-M	Kutnohorite	Clinochlore	Montmorillonite	Illite	Kaolinite			
CG-1	0.8			94.4													4.8		4.8	94.4	0.8
LF-1	12.3	2.5		58.8	6.2		2.7			0.4	3.7		3.9		1.5		8.1		19.7	62.5	17.5
LF-5	61.3	8.2	1.8	1.4	6.6		4.5			3.1	3.2		5.7		4.3				16.6	6.4	74.0
RBU-5	42.5	13.8	3.0	5.0	6.8	6.5	0.8			1.1	2.9	0.9	4.4			4.7	5.8	2.0	21.7	10.9	57.1
MC-4	37.1	6.4	4.4	19.4	11.8		2.8			1.4	4	1	2.6			2.5	6.6		23.5	27.8	46.3
PW-3	17.2		6.1	23.9	9.8		5.9	15.8	6.4	6.8							8.1		17.9	30	45.3
PW-5	0.5		5.1	17.2	1.8		2.7			28.9	43.9								1.8	66.2	3.2
MK-4	19.4		0.9	52.1	11.4		0.8			0.7	4.1					1.4	5.2		18.0	57.1	20.2
RBU-1	49.4	17.4	2	2	2.4	5.6	3.2			0.5		0.5		7.6			8	1.4	10.4	11.6	70
RBU-3				98.5										1.5					0.0	100.0	0.0
RBU-4			3.6	74.5	5.0					0.3				16.5					5.0	94.6	0.0
DM-2			59.0		2.5					0.2	30.0						8.3		10.8	89.0	0.0
DM-5	5.6			87.3	3.2					0.2	2.6		1.0						4.2	89.9	5.6

Table 10. Porosity, average pore diameter, permeability, effective diffusion coefficient, and m values determined by two methods for the thirteen samples.

Sample name	Porosity (%)	d_a (nm)	Permeability (mD)	D_{KA} (m^2/s)	D (m^2/s)	D_e (m^2/s)	Cementation factor *m*	
							Bosanquet formula method	Gas diffusion chamber method
CG-1	7.07	35.30	5.07	5.27×10^{-6}	4.19×10^{-6}	1.38×10^{-7}	1.89	2.13
LF-1	3.47	10.05	1.78	1.50×10^{-6}	1.40×10^{-6}	2.21×10^{-8}	2.03	2.23
LF-5	4.62	18.61	0.71	2.78×10^{-6}	2.45×10^{-6}	5.19×10^{-8}	1.94	1.86
RBU-5	4.52	19.50	1.41	2.91×10^{-6}	2.55×10^{-6}	5.93×10^{-8}	1.92	2.09
MC-4	4.95	20.02	2.98	2.99×10^{-6}	2.61×10^{-6}	5.28×10^{-8}	1.94	1.87
PW-3	4.52	19.50	1.41	2.91×10^{-6}	2.55×10^{-6}	3.50×10^{-7}	1.92	1.61
PW-5	7.48	132.40	NA	1.98×10^{-5}	1.00×10^{-5}	5.28×10^{-8}	1.57	1.44
MK-4	0.94	16.69	0.54	2.49×10^{-6}	2.22×10^{-6}	9.40×10^{-9}	1.65	1.80
RBU-1	5.00	140.00	NA	2.09×10^{-5}	1.03×10^{-5}	2.37×10^{-7}	1.49	0.83
RBU-3	1.09	27.20	0.77	4.06×10^{-6}	3.39×10^{-6}	1.66×10^{-8}	1.57	1.63
RBU-4	0.82	16.70	0.31	2.49×10^{-6}	2.22×10^{-6}	8.20×10^{-9}	1.63	1.70
DM-2	0.41	140.87	1.25	2.10×10^{-5}	1.04×10^{-5}	1.91×10^{-8}	1.58	1.53
DM-5	1.66	13.40	1.35	2.00×10^{-6}	1.82×10^{-6}	1.37×10^{-8}	1.65	1.60

5.4.2. Cementation factor

In this work, several important parameters, such as the average pore diameter (d_a), porosity, and permeability (mD) from MIP tests, the cementation factors obtained from both the gas diffusion chamber method and Bosanquet formula method, are summarized in Table 10. The comparison of cementation factors acquired from the two diffusivity methods is presented in Fig. 13. The results were equally distributed near the straight line with a slope of 1, supporting the validity of these two methods. The cementation factor exhibits a wide range of values from 1 to 2.2 for different rocks, without an apparent relationship of cementation factor to rock types. For instance, both samples RBU-3 and RBU-4 are fossiliferous limestones from Utah, and have significantly lower m values than Texas' fossiliferous limestone CG-1. This suggests that factors other than lithology, such as microfossil particle size and diagenesis of porous media, affect m values and need to be further explored.

5.4.3. Relationships among porosity, permeability, and diffusivity

Porosity and permeability exhibit exponential relationships to diffusivity, giving the best correlation coefficients of 0.4631 and 0.7647, respectively (Figs. 14a-14b), which is consistent with Eq. 15. Similarly, exponential functions between diffusivity and both porosity and permeability were reported by Gao et al. (2013). These results suggest that diffusivity increases as porosity and permeability increase. In addition, there is an exponential relationship between average pore diameter and diffusivity, as shown in Fig. 15. According to these data, these 13 samples can be classified into two discrete groups: Samples CG-1, LF-1, LF-5, and RBU-5, MC-4, PW-3, and PW-5 are classified as Group One, with relatively greater cementation factors (average 1.8995) than Group Two (MK-4, RBU-3, RBU-4, DM-2, and DM-5) which have an average cementation factor of 1.562.

5.4.4. Relationships between porosity, permeability, and cementation factor

The relationship between cementation factor and porosity is highly variable depending on the rock characteristics (Wyllie & Rose, 1950; Raiga-Clemenceau, 1977; Borai, 1987; Focke & Munn, 1987; Olsen et al., 2008). In this study, exponential function relationships between porosity and cementation factors for the two sample groups were observed (Fig. 16a). Samples within Group One have larger porosities than those in Group Two. As porosity increases, the cementation factor of samples in Group One tends to decrease ($R^2 = 0.831$ for fitted exponential regression), while the factor remains relatively constant for Group Two samples ($R^2 = 0.309$). However, there is no strong correlation between this factor and permeability for the two rock groups (Fig. 16b), which was also reported by Olsen et al. (2008).

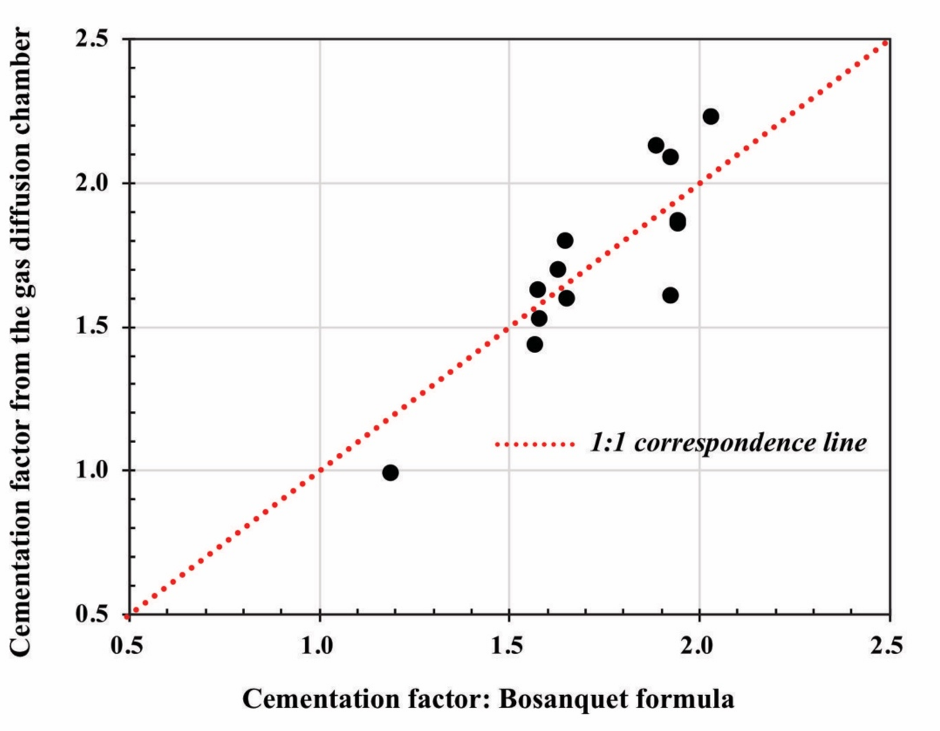

Figure 13. Comparison between cementation factors obtained from gas diffusion chamber method and Bosanquet formula method.

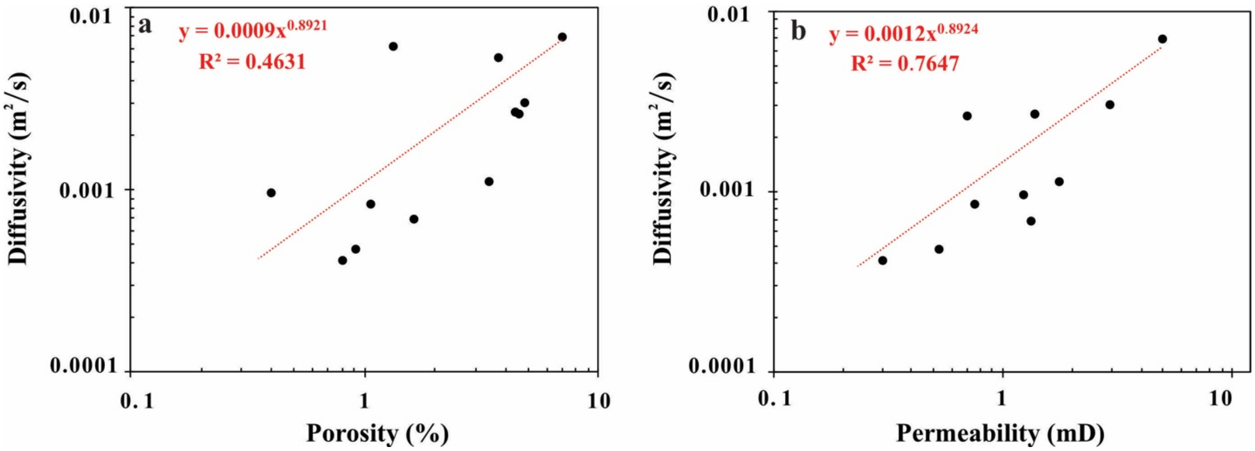

Figure 14. Relationships between diffusivity and porosity (a) and permeability (b).

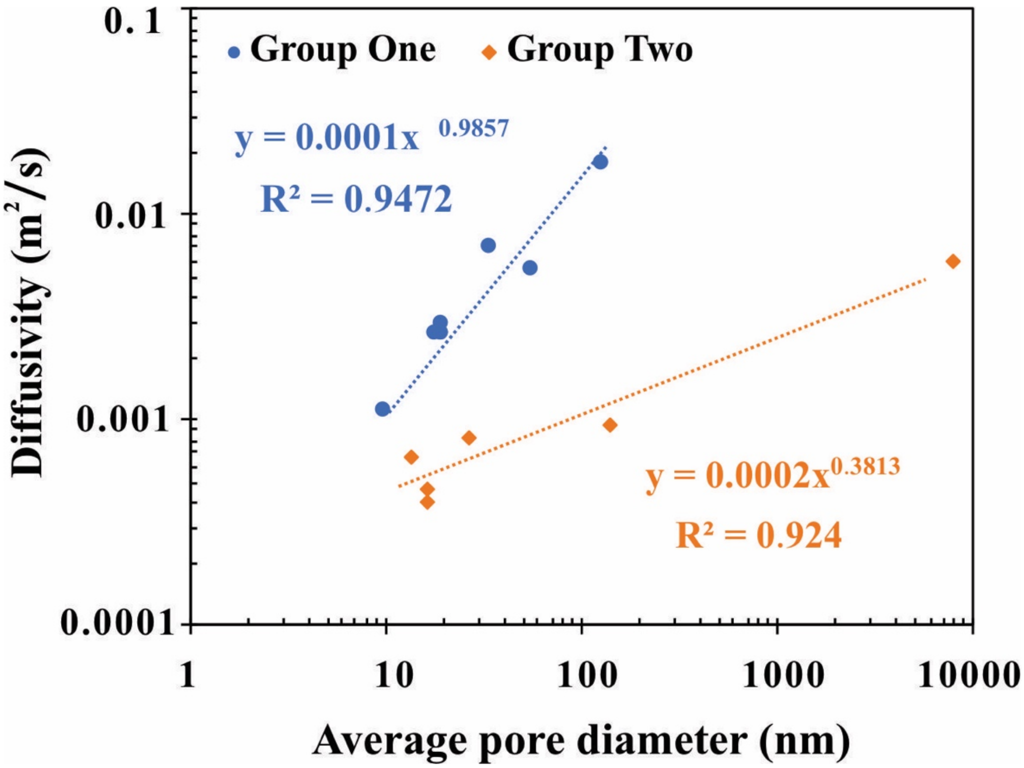

Figure 15. Diffusivity (D') versus average pore diameter (d_a) for 13 samples in two groups.

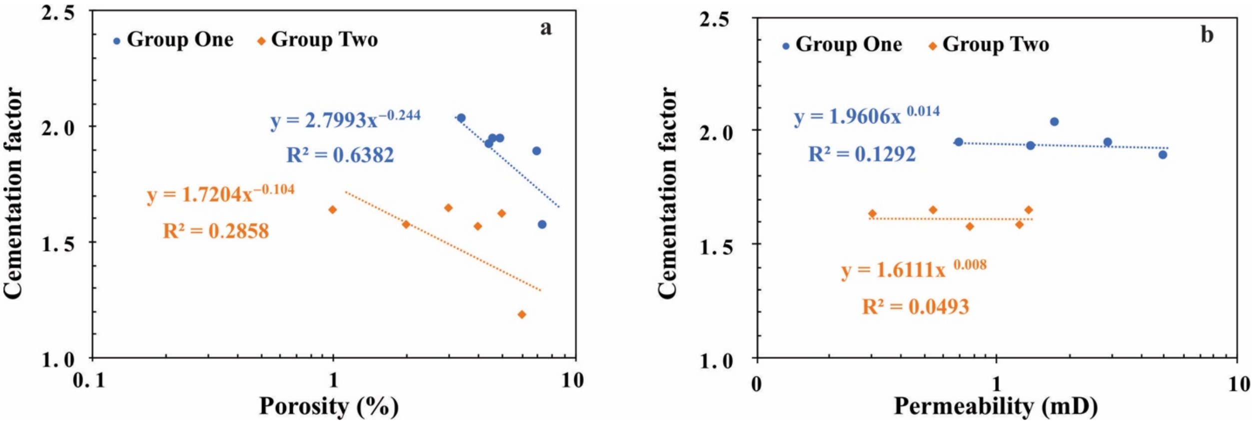

Figure 16. Cementation factor (Bosanquet formula method) vs. porosity and permeability for 13 samples in two groups.

5.5. Diagenetic processes and patterns

5.5.1. Diagenetic process

The compaction processes and cementation could contribute to the reduction of porosity during burial diagenesis (Ehrenberg, 1989; Gluyas & Cade, 1997; Houseknecht, 1987; Lander & Walderhaug, 1999; Brigaud et al., 2009; Lambert et al., 2006; Mørk, 2013; Shalaby et al., 2014), while the dissolution plays an important role in porosity development (Baruch et al., 2015; Colón et al., 2004; Mazzullo & Harris, 1991, 1992).

Group One samples include one limestone (CG-1) and five mudstones (LF-1, LF-5, MC-4, and PW-3). Among them, CG-1, a fossiliferous limestone, was classified as tight limestone based on thin section observations (Fig. 17A). It contains bivalve fragments, which were replaced and/or tightly cemented by both sparry and micritic calcite. Sample LF-1 was classified as mixed carbonate mudstone (Fig. 12) with high calcite content (58.8% by weight). Figure 17B shows that this sample contains abundant small-sized foraminifera (approximately 20-80 µm) and fragments of bivalves, which were uniformly cemented by micritic calcite and clay minerals. In this sample the foraminifera chambers have been filled with secondary sparry calcite in the dark gray matrix. Tight carbonate cementation/matrix resulted in poor reservoir quality in LF-1. In Sample LF-5, a clay-rich siliceous mudstone, has medium to coarse silt-sized angular quartz grains (approximately 20-50 µm) (Fig. 17C), clay matrix and carbonate cement (Fig. 18A). Sample RBU-5 is a mixed siliceous mudstone with course silt grains (45-50 µm). and was firmly cemented and/or replaced by clays (Fig. 18B). Remnant textures of replaced quartz were widely observed (Fig. 17D). Sample MC-4 is a heavily carbonate cemented mixed mudstone. Diagenetic carbonate cements in Sample MC-4 have a tendency to partially or completely replace irregular quartz grains, as shown within the muddy matrix (Fig. 17E). Numerous aggregates of homogeneous microcrystalline and sparry macrocrystalline carbonate cements were identified in Sample PW-3. Macrocrystalline carbonate cements are in a shape of a parallelogram (Fig. 17F). Tightly carbonate-cemented microfossils were found in Sample PW-5. Calcareous microfossils within the lithified matrix show a more or less parallel arrangement (Fig. 17G). Additionally, intragranular fractures were found in quartz grains that are probably related to intense burial compaction in RBU-5 (Makowitz & Milliken, 2003; Makowitz et al., 2006).

In general, samples in Group One are from tight reservoirs and have experienced multiple diagenetic alterations, progressively destroying the reservoir quality. Those well-cemented tight reservoir samples without apparent dissolution tends to exhibit higher cementation factors (Akbar et al., Gao & Hu, 2013; 2008; Byun et al., 2019).

In contrast, Group Two samples exhibited lower cementation factor values either due to the occurrence of the connected fractures (microfractures and open calcite veins) or to the lower degree of compaction and cementation, along with higher dissolution. For example, sample MK-4 is a mixed carbonate mudstone (Fig. 12), with high carbonate content (57.1%). The carbonates in the sample are almost completely sparry calcite. The quartz grains in the carbonate-cemented areas display a patchy 'floating' texture (Fig. 17E). In thin sections of RBU-1, the secondary pore space resulting from the dissolution of carbonate cement was widely observed. Generally, grain sizes fall within the 200-300 μm range, while dissolved pore sizes are typically found in the 50-180 μm range (Fig. 7I).

Samples RBU-3 and RBU-4 are both fossiliferous limestones with microalgae as the main fossil type (Fig. 17F and 17G). Fragments of bivalves filled with micrites, were also commonly observed in RBU-4. Those fossils appeared to be very well-preserved with intact shells. Since fossils are commonly damaged and fractured during compaction (Briggs & Williams, 1981; Khanqa et al., 2009; Marshall & Pirrie, 2013), it appears that sample RBU-3 and RBU-4 experienced a lower degree of compaction and micritization process than Group One samples. DM-2 (dolomite marble) and DM-5 (calcite marble) are two marble samples with different crystal sizes. DM-2 is poorly sorted, with grains ranging from 100 to 700 μm. Microfractures and connected inter-crystalline dissolution pores were observed (Fig. 17H). This explains the unusually high average pore diameter (141 nm) from the MIP analysis. Consequently, microfractures (either induced or natural) may result in a low m value (1.58) in the sample. The effects of fractures and microfractures resulting in lower cementation factor values have been widely reported (e.g., Focke & Munn, 1987; Widarsono, 2011). However, sample DM-5 is a micritic calcite marble, contains sparry calcite-cemented fractures (veins). Some of the veins range up to 800 μm in width with crystals reach sand size (~200 μm). This vein also contains organic matter (Fig. 17I). Consequently, this open calcite vein can contribute to better reservoir quality and a relatively lower cementation factor in DM-5 than most non-fractured samples.

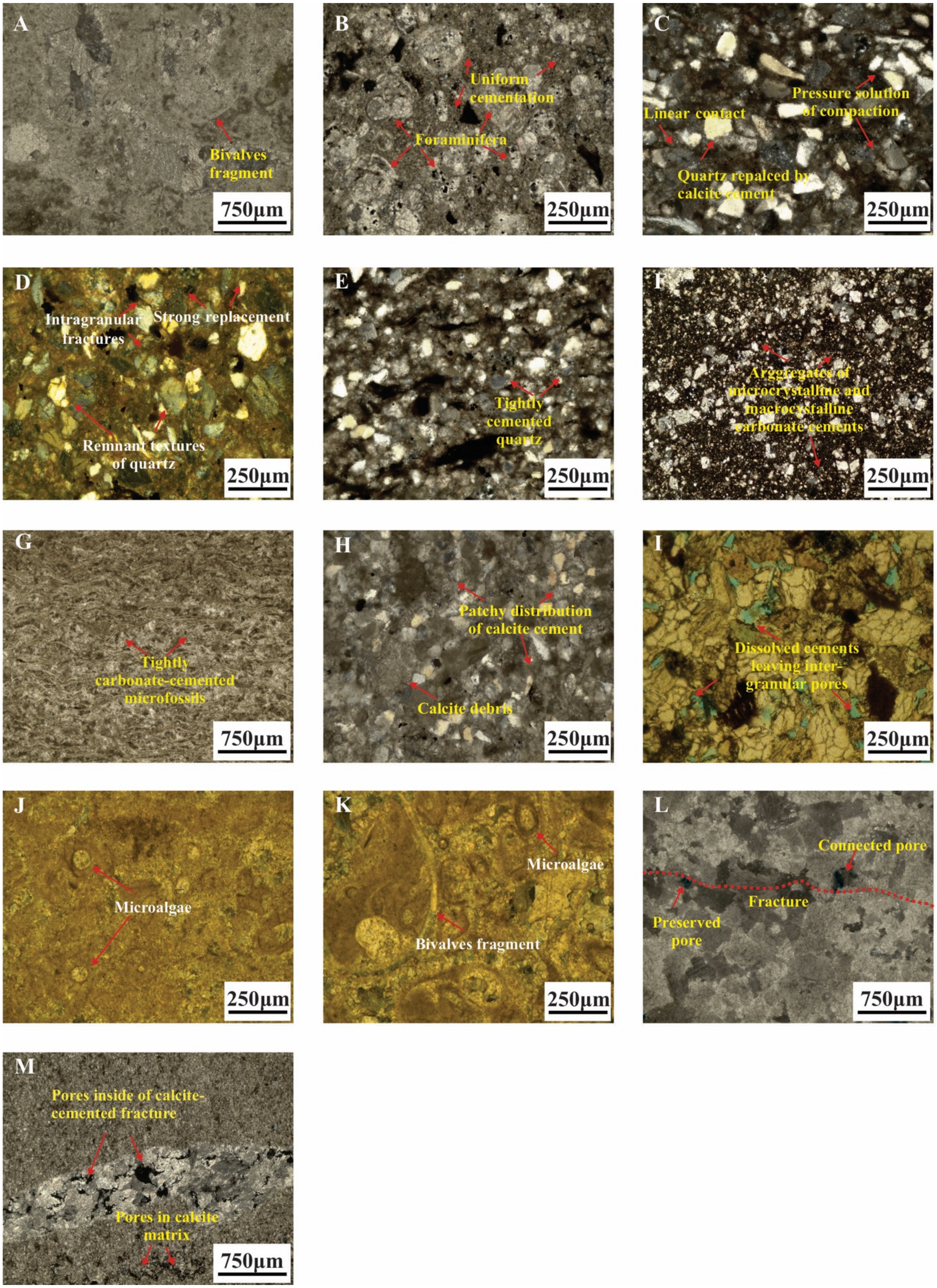
A
Bivalves fragment
750μm
B
Uniform cementation
Foraminifera
250μm
C
Pressure solution of compaction
Linear contact
Quartz repalced by calcite cement
250μm
D
Intragranular fractures
Strong replacement
Remnant textures of quartz
250μm
E
Tightly cemented quartz
250μm
F
Arggregates of microcrystalline and macrocystalline carbonate cements
250μm
G
Tightly carbonate-cemented microfossils
750μm
H
Patchy distribution of calcite cement
Calcite debris
250μm
I
Dissolved cements leaving inter-granular pores
250μm
J
Microalgae
250μm
K
Microalgae
Bivalves fragment
250μm
L
Connected pore
Fracture
Preserved pore
750μm
M
Pores inside of calcite-cemented fracture
Pores in calcite matrix
750μm

Figure 17. Thin section petrographs of 13 rock samples: (A) Microfossils are tightly cemented by carbonate cement (CG-1); (B) Massive foraminifera are uniformly cemented by calcite cement (LF-1); (C) Pressure solution commonly occur at the contact between two stressed quartz grains, with linear contact between grains indicating a strong diagenetic modification due to compaction, and diagenetic cementation and replacement by carbonate also generally observed (LF-5); (D) Intergranular fractures in quartz grains are common; extensive replacement of quartz by carbonate left fine-textured remnant portions (RBU-5); (E) Quartz is tightly cemented by carbonate cements (MC-4); (F) Aggregates of micrite microcrystalline and sparry macrocrystalline carbonate cements are identified (PW-3); (G) Tightly carbonate-cemented microfossils in matrix (PW-5); (H) Carbonate minerals mainly occur as calcite debris rather than cement, and patchy calcite cement in the host rock is highlighted by arrows (MK-4); (I) Dissolved pore space in sandstone (RBU-1); (J) Microalgae are cemented by micritic calcite (RBU-3); (K) Fragments of bivalves and microalgae cemented by carbonate are observed (RBU-4); (L) One microfracture crosses the entire width of the sample in the field of view, with arrows highlighting the positions of connected pores (DM-2); and (M) A semi-filled calcite vein covered the entire thin section in width (DM-5).

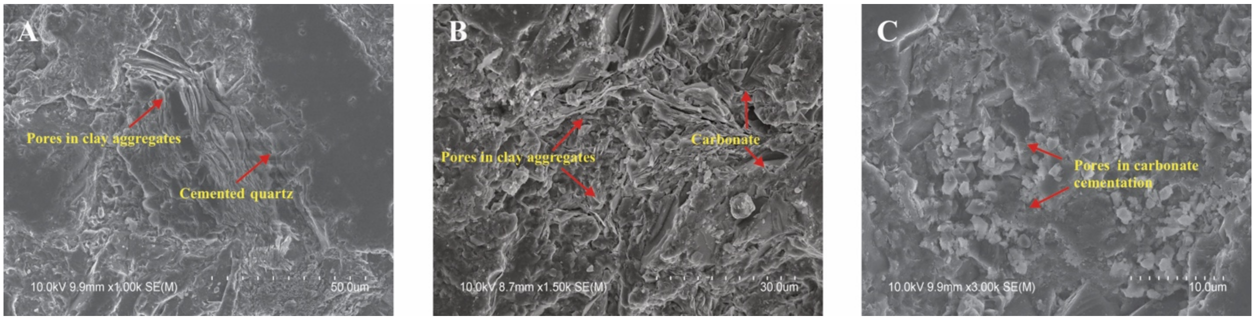

Figure 18. SEM images of three fine-grained mudstones: (A) Sheetlike pores within clay aggregates (LF-5), with no noticeable dissolution being observed; (B) Mixed cementation by clays and carbonates (RBU-5); and (C) Carbonate as a common cementing material with pores found inside of it (MK-4).

5.5.2. Diagenetic patterns

Obvious dissolution was only observed in RBU-1 sample. Rocks from Group One tended to exhibit strong compaction, strong cementation, and weak dissolution, as shown in Figs. 20A. For example, CG-1 shows tight matrices (Fig. 19A), microfossils are tightly cemented by calcite in LF-1 (Fig. 9B), while LF-5, RBU-5, MC-4, PW-3, and PW-5 (Figs. 19C-G) experienced strong diagenetic compaction and cementation. In specific, intergranular pressure solution in LF-5 and intensive fracturing of quartz grains in RBU-5 indicate intense compaction and deformation. Consequently, CG-1, LF-1, LF-5, RBU-5, MC-4, PW-3, and PW-5 were classified as strong compaction, strong cementation, and weak dissolution-diagenesis pattern, displaying higher cementation factors (Figs. 20A and Table 10).

No obvious pressure solution and fractures were observed in MK-4 (Fig. 19H). High degree of inter-granular dissolution was found in RBU-1(Fig. 19I). Intact fossils occurred in RBU-3 (Fig. 19J) and RBU-4, which indicated a weak compaction (Fig. 19K), while fossil edges are very clear, suggesting medium cementation. As a result, MK-4, RBU-1, RBU-3, and RBU-4 are categorized as weak compaction, medium cementation, and weak/strong dissolution-diagenesis pattern with cementation factors around 1.5-1.8 (Fig. 20B and Table 10). Moreover, these results show microfracture development has a significant impact on the physical properties of DM-2 and DM-5 (Fig. 19L-M), tending to decrease the cementation factor. Thus, DM-2 and DM-5 are classified as the fracture-matrix diagenesis pattern, showing lower cementation factors (around 1.5-1.6) (Fig. 20C and Table 10).

Table 10. Summary of dominated diagenetic process of each diagenetic pattern and associated cementation group and cementation factor range.

Diagenetic pattern	Main diagenesis types	Cementation group	Cementation factor range
Strong compaction, strong cementation, and weak dissolution	Dominated by compaction and cementation	One	1.6～2.2
Weak compaction, medium cementation, and weak/strong dissolution	Dominated by weak compaction and cementation	Two	1.5～1.8
Fracture-matrix interaction	Affected by the presence of fracture	Two	1.5～1.6

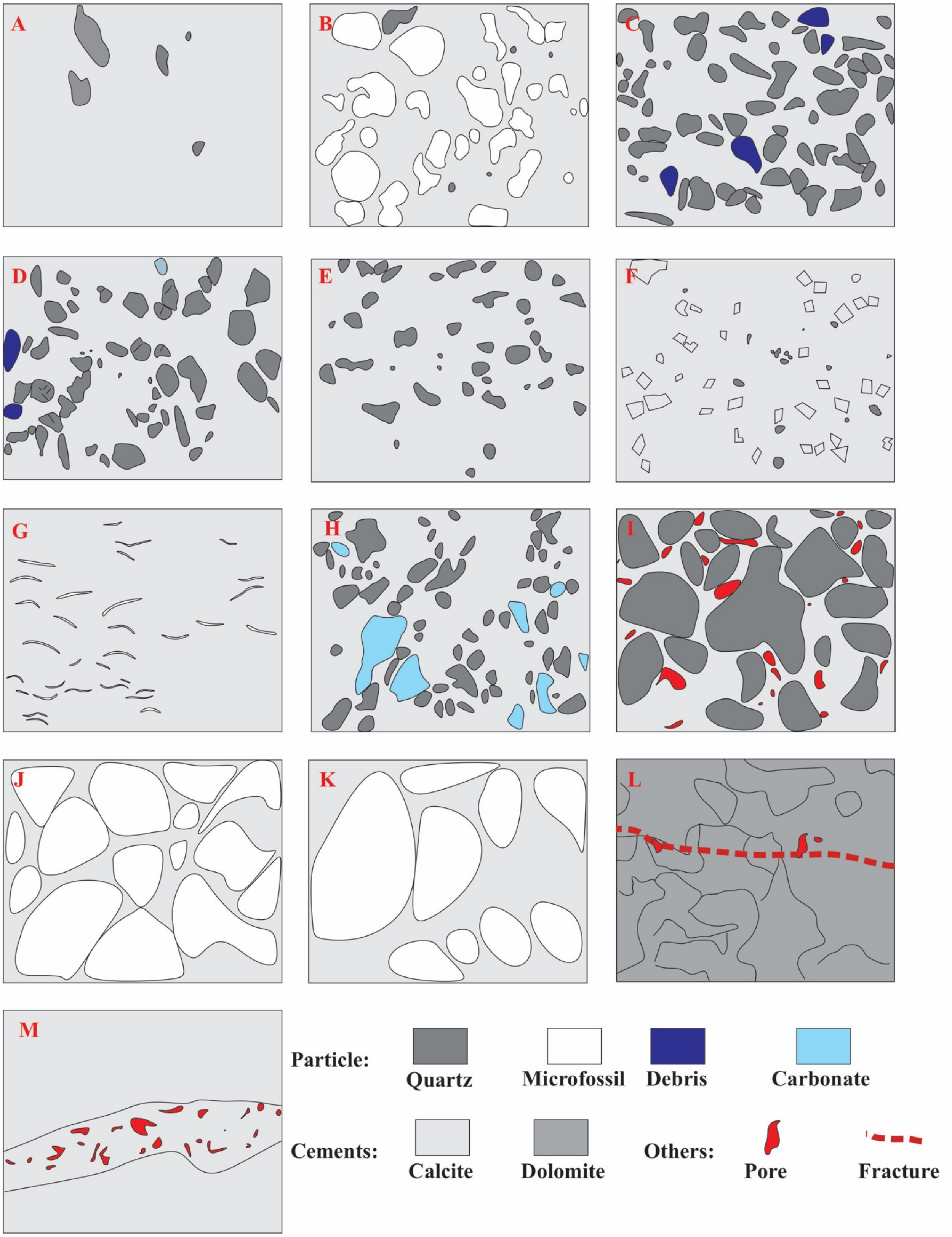

Figure 19. Sketches of diagenesis for thirteen samples: (A) Diagram showing a tight matrix (CG-1); (B) Grains, namely microfossils, are uniformly cemented (LF-1); (C-G) Grains (quartz and

microfossils) are heavily compacted, strongly cemented, and/or replaced by cements of clay and carbonate (LF-5, RBU-5, MC-4, PW-3, and PW-5); (H) Weak compaction and medium cementation (MK-4); (I) Weak compaction, medium cementation, and strong dissolution in matrix (MK-4); (J-K) Nonuniform patchy cementation between grains (mostly microfossils) without obvious compaction (RBU-3 and RBU-4); and (L-M) Fractures observed in thin sections (DM-2 and DM-5).

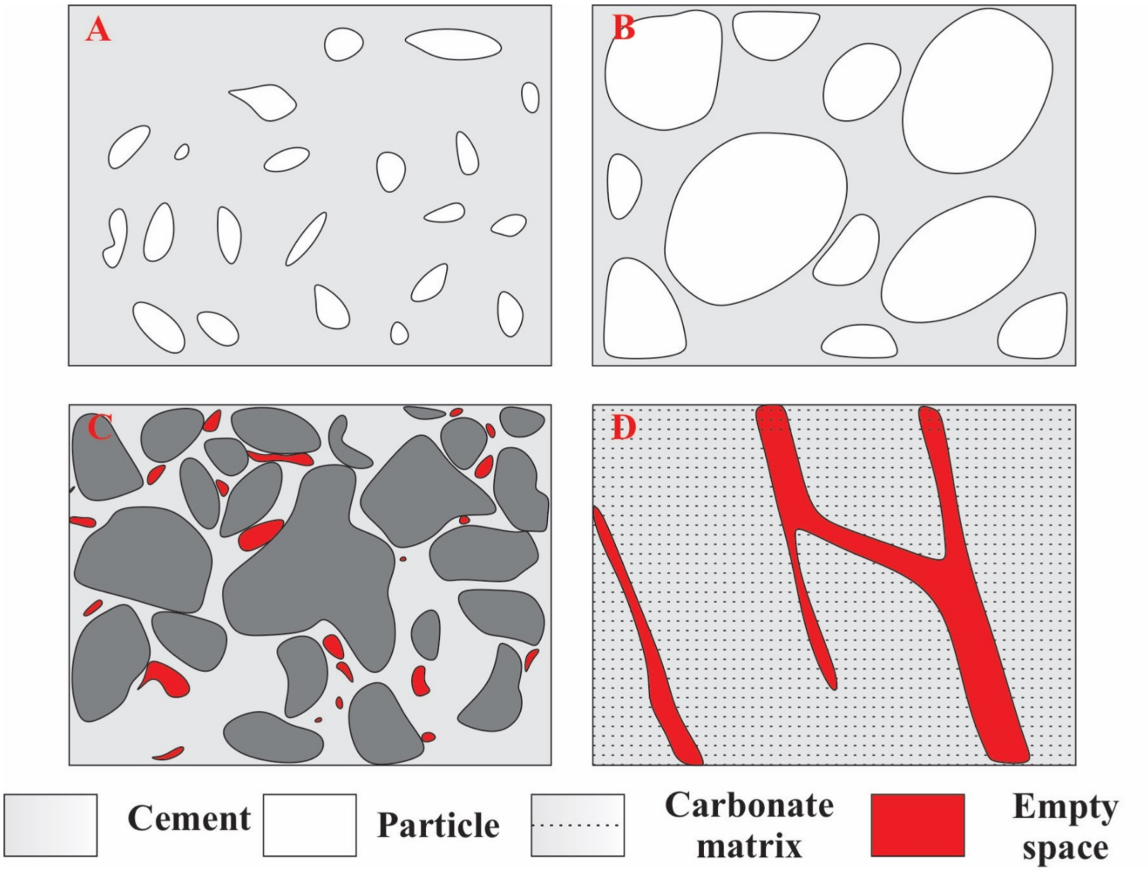

Figure 20. Genetic classification of diagenetic patterns for two groups of samples: (A) Strong compaction, strong cementation, and weak dissolution-diagenesis pattern (CG-1, LF-1, LF-5, RBU-5, MC-4, PW-3, and PW-5); (B) Weak compaction, medium cementation, and weak dissolution-diagenesis pattern (MK-4, RBU-3, and RBU-4); (C) Weak compaction, medium cementation, and strong dissolution-diagenesis pattern (RBU-1); and (D) Fracture-matrix pattern (DM-2 and DM-5).

5.6. Summary

The objective of this work is to derive comparative cementation factors for thirteen different geologic sample in order to understand the effects of diagenetic processes on cementation factor values. The cementation factors were calculated using both the gas diffusion chamber method and the Bosanquet formula method to derive the diffusivities, while porosity was determined by MIP. Cementation factor values derived from these two methods agree quite well with each other. Gas diffusivity is positively correlated with both permeability and porosity. These 13 samples were further categorized into two groups based on the relationship between average pore diameter and gas diffusivity. Group One, which has higher porosity, exhibits higher average cementation factors when compared to Group Two. Exponential relationships exist between the cementation factor and porosity for both Groups One and Two, while no correlations are observed between this factor and permeability for the two groups of rocks. More….

CHAPTER 6. CONCLUSIONS AND RECOMMENDATIONS

6.1. Conclusions

Upon conducting comprehensive investigations into the pore structure using both gas diffusion and aqueous-phase chemical sorption techniques across six distinct natural rocks with varying sample sizes, our analyses lead to several significant conclusions. For relatively heterogeneous rocks, employing smaller sample scales can have a beneficial impact on pore connectivity and mass transport properties. In the case of comparatively homogeneous geological materials, the alterations in pore connectivity observed across different sample sizes are relatively insignificant, signifying the relative independence of physical and chemical transport properties from particle sizes. Additionally, this study further substantiates the noteworthy influences of clay minerals and particle size on the ionic sorption capacity of natural rock samples.

Thin section observations indicate that diagenesis is a key factor that influences the cementation factor. Uniform cementation and compaction result in higher cementation factor values, while weak compaction and medium cementation are more likely to result in lower cementation factor values. In addition, microfracture development has a substantial impact on the characteristics of the entire matrix and can directly result in decreased cementation factor values. Four diagenetic patterns were established for the thirteen samples. The strong compaction, strong cementation, and weak dissolution-diagenesis pattern tended to have higher cementation factors, while the weak compaction, medium cementation, weak dissolution-diagenesis pattern and the fracture-matrix pattern exhibited lower cementation factor values. These findings are useful in implementing carbon utilization and storage projects in various geological formations in the context of efficiency and long-term performance.

6.2. Recommendations and Future Research

This dissertation first examines the physical attributes (pore structure, especially pore connectivity), then combined effects of both physical and chemical (sorption) processes for six natural rocks, and continues with the cementation ….of 13 natural rocks. …. Future studies will include dynamic column transport with a range of sample sizes and water saturation, as the equilibrium-type batch sorption tests, while being practical and cost-effective to produce a broad-brush understanding of the relative magnitude of various chemicals in a fluid-tracer-rock system, indicates a “maximum” interaction which is not representative of the field conditions where fluid-rock interactions are momentary and kinetics-controlled. In addition, the unique gas diffusion approach with oxygen gas tracer will need to verify the chemical interactions with a wide range of natural rocks to separate the potential diffusive flux from both physical and chemical process, using a newly custom-designed apparatus of multiple gas tracers (Hu et al., 2022).

Nomenclature

C	Initial concentration of tracers, mg/L
C_0	Initial oxygen concentration, %
C_c	Curvature coefficient
C_e	Equilibrated/final concentration of tracers, mg/L
C_r	Relative oxygen concentration in the chamber, %
ΔC_r	Relative oxygen-concentration increment from total diffusion
$C_{r-inter}$	Relative oxygen concentration from inter-particle diffusion
$\Delta C_{r-inter}$	Relative oxygen-concentration increment from inter-particles diffusion
$\Delta C_{r-intra}$	Relative oxygen-concentration increment from intra-particle diffusion
$C_{r-intra}$	Relative oxygen concentration from intra-particle diffusion
$\Delta C_{r-quartz}$	Relative oxygen-concentration increment from inter-quartz particles
C_S	Atmospheric oxygen concentration, %
C_t	Oxygen concentration at time t, %
$C_{t-inter}$	Oxygen concentration from inter-particle diffusion, %
$C_{t-intra}$	Oxygen concentration from intra-particle diffusion, %
C_u	Uniformity coefficient
D	Fractal dimension of entire pores
D_1	Fractal dimension of mesopores
D_2	Fractal dimension of transitional pores
D_3	Fractal dimension of micropores
D_P	Pore or effective diffusion coefficient, (m^2/s)
d_x	Characteristic particle size where x% of the mass is finer than dx
K_d	Sorption coefficient, mL/g
L	Height of packed bed of particle samples, cm
M	Mass of adsorbent used in batch test, g
R^2	Correlation coefficient for fractal dimensions
S_W	Cumulative pore volume fraction, %
S_{Hg}	Mercury saturation, %
V	Solution volume in batch test, mL

Greek symbols

α	Volume of the chamber per area of packed bed, m^3
α_n	positive root of $(\alpha_n L)$ tan $(\alpha_n L) = hL$
γ	Pore throat radius, μm
γ_{max}	Maximum pore throat radius, μm
$\emptyset_1$	Porosity corresponding to pore throat diameter in 100-1000 nm, %
$\emptyset_2$	Porosity corresponding to pore throat diameter in 10-100 nm, %
$\emptyset_3$	Porosity corresponding to pore throat diameter in 2.5-10 nm, %
$\emptyset$	Air-filled pore space percentage in packed sample, %
$\emptyset_{qtz}$	Air-filled pore space percentage in packed bed of quartz grains, %

REFERENCES

Adler, P. M., Jacquin, C. G., & Thovert, J. F. (1992). The formation factor of reconstructed porous media. *Water resources research*, 28(6), 1571-1576.

Aguilera, R. (1976). Analysis of naturally fractured reservoirs from conventional well logs (includes associated papers 6420 and 6421). *Journal of petroleum technology*, 28(07), 764-772.

Akbar, M., Steckhan, J., Tamimi, M., Zhang, T., & Saner, S. (2008). Estimating cementation factor (m) for carbonates using borehole images and logs. In *Abu Dhabi International Petroleum Exhibition and Conference*. OnePetro.

Akin, S., Schembre, J., Bhat, S., & Kovscek, A. (2000). Spontaneous imbibition characteristics of diatomite. *Journal of Petroleum Science and Engineering*, *25*(3-4), 149-165.

Allen, D., Kenyon, W., Lisitza, N., & Song, Y.-Q. (2002). Pore geometry and its geological evolution in carbonate rocks. *Petrophysics-The SPWLA Journal of Formation Evaluation and Reservoir Description*, *43*(05).

Amini, F., & Qi, G. (2000). Liquefaction testing of stratified silty sands. *Journal of Geotechnical and Geoenvironmental Engineering*, *126*(3), 208-217.

Anovitz, L. M., & Cole, D. R. (2015). Characterization and analysis of porosity and pore structures. *Reviews in Mineralogy and Geochemistry*, *80*(1), 61-164.

Aoyagi, K., & Ishii, E. (2019). A method for estimating the highest potential hydraulic conductivity in the excavation damaged zone in mudstone. *Rock Mechanics and Rock Engineering*, *52*(2), 385-401.

Archie, G. E. (1942). The electrical resistivity log as an aid in determining some reservoir characteristics. *Transactions of the AIME*, *146*(01), 54-62.

Armatas, G. S. (2006). Determination of the effects of the pore size distribution and pore connectivity distribution on the pore tortuosity and diffusive transport in model porous networks. *Chemical Engineering Science*, *61*(14), 4662-4675.

Atkins Jr, E. R., & Smith, G. H. (1961). The significance of particle shape in formation resistivity factor-porosity relationships. *Journal of Petroleum Technology*, 13(03), 285-291.

Azar, J. H., Javaherian, A., Pishvaie, M. R., & Nabi-Bidhendi, M. (2008). An approach to defining tortuosity and cementation factor in carbonate reservoir rocks. *Journal of Petroleum Science and Engineering*, 60(2), 125-131.

Barnes, V. E. (1988). The Precambrian of central Texas. *Centennial Field Guide*, *4*, 361-368.

Baruch, E. T., Kennedy, M. J., Löhr, S. C., & Dewhurst, D. N. (2015). Feldspar dissolution-enhanced porosity in Paleoproterozoic shale reservoir facies from the Barney Creek Formation (McArthur Basin, Australia). *AAPG Bulletin*, *99*(9), 1745-1770.

Bernabé, Y., Li, M., Tang, Y.-B., & Evans, B. (2016). Pore space connectivity and the transport properties of rocks. *Oil & Gas Science and Technology–Revue d'IFP Energies nouvelles*, *71*(4), 50.

Borodich, F. M., Bull, S., & Epshtein, S. (2015). Nanoindentation in studying mechanical properties of heterogeneous materials. *Journal of Mining Science*, *51*, 470-476.

Boving, T. B., & Grathwohl, P. (2001). Tracer diffusion coefficients in sedimentary rocks: correlation to porosity and hydraulic conductivity. *Journal of Contaminant Hydrology*, *53*(1-2), 85-100.

Borai, A. (1987). A new correlation for the cementation factor in low-porosity carbonates. *SPE Formation Evaluation*, *2*(04), 495-499.

Bradbury, M. H., & Baeyens, B. (2000). A generalised sorption model for the concentration dependent uptake of caesium by argillaceous rocks. *Journal of Contaminant Hydrology*, *42*(2-4), 141-163.

Brigaud, B., Durlet, C., Deconinck, J.-F., Vincent, B., Thierry, J., & Trouiller, A. (2009). The origin and timing of multiphase cementation in carbonates: Impact of regional scale geodynamic events on the Middle Jurassic Limestones diagenesis (Paris Basin, France). *Sedimentary Geology*, *222*(3-4), 161-180.

Briggs, D. E., & Williams, S. H. (1981). The restoration of flattened fossils. *Lethaia*, *14*(2), 157-164.

Bryant, S. L., Mellor, D. W., & Cade, C. A. (1993). Physically representative network models of transport in porous media. *AIChE Journal*, *39*(3), 387-396.

Bucher, K., & Frey, M. (2002). *Petrogenesis of Metamorphic Rocks*. Springer Berlin, Heidelberg.

Byun, Y. H., Hong, W. T., & Yoon, H. K. (2019). Characterization of cementation factor of unconsolidated granular materials through time domain reflectometry with variable saturated conditions. *Materials*, *12*(8), 1340.

Cai, J., Lin, D., Singh, H., Wei, W., & Zhou, S. (2018). Shale gas transport model in 3D fractal porous media with variable pore sizes. *Marine and Petroleum Geology*, *98*, 437-447.

Cai, Y., Liu, D., Pan, Z., Yao, Y., Li, J., & Qiu, Y. (2013). Pore structure and its impact on CH4 adsorption capacity and flow capability of bituminous and subbituminous coals from Northeast China. *Fuel*, *103*, 258-268.

Cao, T., Song, Z., Wang, S., & Xia, J. (2016). Characterization of pore structure and fractal dimension of Paleozoic shales from the northeastern Sichuan Basin, China. *Journal of Natural Gas Science and Engineering*, *35*, 882-895.

Carniglia, S. (1986). Construction of the tortuosity factor from porosimetry. *Journal of Catalysis*, *102*(2), 401-418.

Carothers, J. E. (1968). A statistical study of formiton factor relation to porosity. *The Log Analyst*, 9, 38-52.

Chagneau, A., Claret, F., Enzmann, F., Kersten, M., Heck, S., Madé, B., & Schäfer, T. (2015). Mineral precipitation-induced porosity reduction and its effect on transport parameters in diffusion-controlled porous media. *Geochemical Transactions*, *16*(1), 1-16.

Chang, C., & Lenhoff, A. M. (1998). Comparison of protein adsorption isotherms and uptake rates in preparative cation-exchange materials. *Journal of Chromatography A*, *827*(2), 281-293.

Choo, J., & Borja, R. I. (2015). Stabilized mixed finite elements for deformable porous media with double porosity. *Computer Methods in Applied Mechanics and Engineering*, *293*, 131-154.

Choquette, P. W., & Pray, L. C. (1970). Geologic nomenclature and classification of porosity in sedimentary carbonates. *AAPG Bulletin*, *54*(2), 207-250.

Colón, C. F. J., Oelkers, E. H., & Schott, J. (2004). Experimental investigation of the effect of dissolution on sandstone permeability, porosity, and reactive surface area. *Geochimica et Cosmochimica Acta*, *68*(4), 805-817.

Cunningham, R. E., & Williams, R. J. J. (1980). *Diffusion in Gases and Porous Media*. Springer New York, NY.

Currie, J. (1960). Gaseous diffusion in porous media Part 1.-A non-steady state method. *British Journal of Applied Physics*, *11*(8), 314.

David, C. (1993). Geometry of flow paths for fluid transport in rocks. *Journal of Geophysical Research: Solid Earth*, *98*(B7), 12267-12278.

David, C., Wassermann, J., Amann, F., Lockner, D. A., Rutter, E. H., Vanorio, T., Amann Hildenbrand, A., Billiotte, J., Reuschlé, T., & Lasseux, D. (2018). KG²B, a collaborative benchmarking exercise for estimating the permeability of the Grimsel granodiorite–Part 1: measurements, pressure dependence and pore-fluid effects. *Geophysical Journal International*, *215*(2), 799-824.

Davudov, D., & Moghanloo, R. G. (2018). Scale-dependent pore and hydraulic connectivity of shale matrix. *Energy & Fuels*, *32*(1), 99-106.

Dehghan, A. A., Kharrat, R., Ghazanfari, M. H., & Farzaneh, S. A. (2009). Studying the effects of pore geometry, wettability and co-solvent types on the efficiency of solvent flooding to heavy oil in five-spot models. Asia Pacific Oil and Gas Conference & Exhibition,

Donaldson, E., & Siddiqui, T. (1989). c. *SPE Formation Evaluation*, *4*(03), 359-362.

Dou, W., Liu, L., Wu, K., Xu, Z., Liu, X., & Feng, X. (2018). Diagenetic heterogeneity, pore throats characteristic and their effects on reservoir quality of the Upper Triassic tight sandstones of Yanchang Formation in Ordos Basin, China. *Marine and Petroleum Geology*, *98*, 243-257.

Dravis, J. J., & Yurewicz, D. A. (1985). Enhanced carbonate petrography using fluorescence microscopy. *Journal of Sedimentary Research*, *55*(6), 795-804.

Drits, V., Ivanovskaya, T., Sakharov, B., Zvyagina, B., Derkowski, A., Gor'kova, N., Pokrovskaya, E., Savichev, A., & Zaitseva, T. (2010). Nature of the structural and crystal-chemical heterogeneity of the Mg-rich glauconite (Riphean, Anabar Uplift). *Lithology and Mineral Resources*, *45*, 555-576.

Dubinin, M., & Stoeckli, H. (1980). Homogeneous and heterogeneous micropore structures in carbonaceous adsorbents. *Journal of Colloid and Interface Science*, *75*(1), 34-42.

Dullien, F. A. (2012). *Porous Media: Fluid Transport and Pore Structure*. Academic Press.

Ehrenberg, S. (1989). Assessing the relative importance of compaction processes and cementation to reduction of porosity in sandstones: discussion; compaction and porosity evolution of Pliocene sandstones, Ventura Basin, California: Discussion. *AAPG Bulletin*, *73*(10), 1274-1276.

Emmanuel, S., & Berkowitz, B. (2007). Effects of pore‐size controlled solubility on reactive transport in heterogeneous rock. *Geophysical Research Letters*, *34*(6).

Evans III, R., Watson, G., & Mason, E. (1961). Gaseous diffusion in porous media at uniform pressure. *The Journal of Chemical Physics*, *35*(6), 2076-2083.

Ewing, R. P., & Horton, R. (2002). Diffusion in sparsely connected pore spaces: Temporal and spatial scaling. *Water Resources Research*, *38*(12), 21-21-21-13.

Fabricius, I. L. (2007). Chalk: composition, diagenesis and physical properties. *Bulletin of the Geological Society of Denmark*, *55*, 97-128.

Fan, J.-X., Wang, Y.-J., Cui, X.-D., & Zhou, D.-M. (2013). Sorption isotherms and kinetics of Sb(V) on several Chinese soils with different physicochemical properties. *Journal of Soils and Sediments*, *13*(2), 344-353.

Fandrich, R., Gu, Y., Burrows, D., & Moeller, K. (2007). Modern SEM-based mineral liberation analysis. *International Journal of Mineral Processing*, *84*(1-4), 310-320.

Fang, X., Cai, Y., Liu, D., & Zhou, Y. (2018). A mercury intrusion porosimetry method for methane diffusivity and permeability evaluation in coals: A comparative analysis. *Applied Sciences*, *8*(6), 860.

Fauzi, U., Hoerdt, A., & Neubauer, F. (2002). Influence of coordination number and percolation probability on rock permeability estimation. *Geophysical Research Letters*, *29*(8), 78-71-78-74.

Fitch, P. J., Lovell, M. A., Davies, S. J., Pritchard, T., & Harvey, P. K. (2015). An integrated and quantitative approach to petrophysical heterogeneity. *Marine and Petroleum Geology*, *63*, 82-96.

Focke, J., & Munn, D. (1987). Cementation exponents in Middle Eastern carbonate reservoirs. *SPE Formation Evaluation*, *2*(02), 155-167.

Friedman, G. M. (1978). Classification of sediments and sedimentary rocks. In: Middleton, G.V., Church, M.J., Coniglio, M., Hardie, L.A., Longstaffe, F.J. (eds) *Encyclopedia of Sediments and Sedimentary Rocks*. Encyclopedia of Earth Sciences Series. Springer, Dordrecht.

Fu, Y., Jiang, Y., Wang, Z., Hu, Q., Xie, J., Ni, G., Lei, Z., Zhou, K., & Liu, X. (2019). Non-connected pores of the Longmaxi shale in southern Sichuan Basin of China. *Marine and Petroleum Geology*, *110*, 420-433.

Gallagher, S. R. (2014). *Depositional and diagenetic controls on reservoir heterogeneity: Upper morrow sandstone, Farnsworth Unit, Ochiltree County, Texas* Citeseer].

Gao, Z., Fan, Y., Xuan, Q., & Zheng, G. (2020). A review of shale pore structure evolution characteristics with increasing thermal maturities. *Advances in Geo-Energy Research*, *4*(3), 247.

Gao, Z., & Hu, Q. (2013). Estimating permeability using median pore-throat radius obtained from mercury intrusion porosimetry. *Journal of Geophysics and Engineering*, *10*(2), 025014.

Gao, Z., & Hu, Q. (2018). Pore structure and spontaneous imbibition characteristics of marine and continental shales in China. *AAPG Bulletin*, *102*(10), 1941-1961.

Gao, Z., Hu, Q., & Liang, H. (2013). Gas diffusivity in porous media: determination by mercury intrusion porosimetry and correlation to porosity and permeability. *Journal of Porous Media*, *16*(7).

Ghamartale, A., Escrochi, M., Riazi, M., & Faghih, A. (2019). Experimental investigation of ultrasonic treatment effectiveness on pore structure. *Ultrasonics Sonochemistry*, *51*, 305-314.

Giammar, D. E., Maus, C. J., & Xie, L. (2007). Effects of particle size and crystalline phase on lead adsorption to titanium dioxide nanoparticles. *Environmental Engineering Science*, *24*(1), 85-95.

Gluyas, J., & Cade, C. A. (1997). Prediction of porosity in compacted sands. *Reservoir Quality Prediction in Sandstones and Carbonates*. *69*, 19-27.

Gomez-Rivero, 1976

Gong, L., Nie, L., & Xu, Y. (2020). Geometrical and topological analysis of pore space in sandstones based on x-ray computed tomography. *Energies*, *13*(15), 3774.

Grathwohl, P. (2012). *Diffusion in Natural Porous Media: Contaminant Transport, Sorption/Desorption and Dissolution Kinetics* (Vol. 1). Springer Science & Business Media.

Greenkorn, R., Johnson, C., & Harding, R. (1965). Miscible displacement in a controlled natural system. *Journal of Petroleum Technology*, *17*(11), 1329-1335.

Hajizadeh, A., Safekordi, A., & Farhadpour, F. A. (2011). A multiple-point statistics algorithm for 3D pore space reconstruction from 2D images. *Advances in Water Resources*, *34*(10), 1256-1267.

He, Y. Q., Zhang, N. N., & Wang, X. D. (2011). Adsorption of graphene oxide/chitosan porous materials for metal ions. *Chinese Chemical Letters*, *22*(7), 859-862.

He, Z., Li, G., Tian, S., Wang, H., Shen, Z., & Li, J. (2016). SEM analysis on rock failure mechanism by supercritical CO_2 jet impingement. *Journal of Petroleum Science and Engineering*, *146*, 111-120.

Helios-Rybicka, E., & Wójcik, R. (2012). Competitive sorption/desorption of Zn, Cd, Pb, Ni, Cu, and Cr by clay-bearing mining wastes. *Applied Clay Science*, *65*, 6-13.

Hiatt, E. E., & Pufahl, P. K. (2014). Cathodoluminescence petrography of carbonate rocks: a review of applications for understanding diagenesis, reservoir quality and pore system evolution. *Short Course*, *45*, 75-96.

Hill, H. J., & Milburn, J. D. (1956). Effect of clay and water salinity on electrochemical behavior of reservoir rocks. *Transactions of the AIME*, 207(01), 65-72.

Hollis, C., Vahrenkamp, V., Tull, S., Mookerjee, A., Taberner, C., & Huang, Y. (2010). Pore system characterisation in heterogeneous carbonates: An alternative approach to widely-used rock-typing methodologies. *Marine and Petroleum Geology*, *27*(4), 772-793.

Hong, M., Yu, L., Wang, Y., Zhang, J., Chen, Z., Dong, L., Zan, Q., & Li, R. (2019). Heavy metal adsorption with zeolites: The role of hierarchical pore architecture. *Chemical Engineering Journal*, *359*, 363-372.

Hou, S., Wang, X., Wang, X., Yuan, Y., Pan, S., Wang, X., 2017. Pore structure characterization of low volatile bituminous coals with different particle size and tectonic deformation using low pressure gas adsorption. *International Journal of Coal Geology*, 183, 1-13.

Houseknecht, D. W. (1987). Assessing the relative importance of compaction processes and cementation to reduction of porosity in sandstones. *AAPG Bulletin*, *71*(6), 633-642.

Hu, Q., 2019. *Pore structure, fluid flow and radionuclide transport in geological barrier materials.* Proceedings of International High-Level Radioactive Waste Management Conference (IHLRWM): Robust Collaboration on the Safe, Secure, and Sustainable Management of High-Level Radioactive Materials Over Multiple Generations, American Nuclear Society, LaGrange Park, IL, pp. 480–486.

Hu, Q., & Wang, J. S. Y. (2003). Aqueous-phase diffusion in unsaturated geologic media: A review. *Critical Reviews in Environmental Science and Technology*, *33*(3), 275-297.

Hu, Q., & Mao, X. (2012). Application of Laser Ablation-Inductively Coupled Plasma-Mass Spectrometry to studies of chemical diffusion, sorption, and transport in natural rock. *Geochemical Journal*, *46*(5), 459-475.

Hu, Q., Ewing, R. P., & Dultz, S. (2012). Low pore connectivity in natural rock. *Journal of Contaminant Hydrology*, *133*, 76-83.

Hu, Q., Ewing, R. P., & Rowe, H. D. (2015). Low nanopore connectivity limits gas production in Barnett formation. *Journal of Geophysical Research: Solid Earth*, *120*(12), 8073-8087.

Hu, Q., Kneafsey, T. J., Trautz, R. C., & Wang, J. S. (2002). Tracer penetration into welded tuff matrix from flowing fractures. *Vadose Zone Journal*, *1*(1), 102-112.

Hu, Q., Zhao, P., Moran, J. E., & Seaman, J. C. (2005). Sorption and transport of iodine species in sediments from the Savannah River and Hanford Sites. *Journal of Contaminant Hydrology*, *78*(3), 185-205.

Hu, Q. Zhang, Y., Meng, X., Li, Z., Xia, Z., & Li, M. (2017). Characterization of micro-nano pore networks in shale oil reservoirs of Paleogene Shahejie Formation in Dongying Sag of Bohai Bay Basin, East China. *Petroleum Exploration and Development*, *44*(5), 720-730.

Hu, Q., Wang, Q., Zhao, C., Zhang, T., Tachi, Y., & Fukatsu, Y. (2021). Fluid flow and chemical transport of shallow and deep mudrocks being implicated by pore geometry and connectivity. Abstract for the 11th Asian Rock Mechanics Symposium (ARMS 11),

Ikenyiri, P., Ukpaka, C., 2016. Overview on the effect of particle size on the performance of wood based adsorbent. *Journal of Chemical Engineering & Process Technology*, 7(5), 1-4.

Ishii, E., Sanada, H., Iwatsuki, T., Sugita, Y., & Kurikami, H. (2011). Mechanical strength of the transition zone at the boundary between opal-A and opal-CT zones in siliceous rocks. *Engineering Geology*, *122*(3-4), 215-221.

Ji, W., Hao, F., Schulz, H.-M., Song, Y., & Tian, J. (2019). The architecture of organic matter and its pores in highly mature gas shales of the lower Silurian Longmaxi Formation in the upper Yangtze platform, south China. *AAPG Bulletin*, *103*(12), 2909-2942.

Jia, Q., Yang, Q., Guo, L., Knutsson, S., Xue, P., Liu, G., & Jiang, L. (2016). Effects of fine content, binder type and porosity on mechanical properties of cemented paste backfill with co-deposition of tailings sand and smelter slag. *Electron. J. Geotech. Eng*, *21*, 6971-6988.

Jiang, F., Tsuji, T., & Shirai, T. (2018). Pore geometry characterization by persistent homology theory. *Water Resources Research*, *54*(6), 4150-4163.

Jiang, Z., Van Dijke, M., Sorbie, K. S., & Couples, G. D. (2013). Representation of multiscale heterogeneity via multiscale pore networks. *Water Resources Research*, *49*(9), 5437-5449.

Johannesen, E., Riskedal, H., Tipura, L., Howard, J., Graue, A., 2007. *Wettability characterization by NMR T2 measurements in Edwards limestone rock*. International Symposium of the Society of Core Analysts, 10-13.

Jones, B., & Luth, R. W. (2003). Petrography of finely crystalline Cenozoic dolostones as revealed by backscatter electron imaging: case study of the Cayman Formation (Miocene), Grand Cayman, British West Indies. *Journal of Sedimentary Research*, *73*(6), 1022-1035.

Jones, B., Luth, R. W., & MacNEIL, A. J. (2001). Powder X-ray diffraction analysis of homogeneous and heterogeneous sedimentary dolostones. *Journal of Sedimentary Research*, *71*(5), 790-799.

Kara, S., Aydiner, C., Demirbas, E., Kobya, M., Dizge, N., 2007. Modeling the effects of adsorbent dose and particle size on the adsorption of reactive textile dyes by fly ash. *Desalination*, 212(1), 282-293.

Karickhoff, S. (1980). In Contaminants and Sediments; Baker, RA, Ed. *Ann Arbor Science Pub. Inc. Ann Arbor, MI*, 193-205.

Kashif, M., Cao, Y., Yuan, G., Asif, M., Javed, K., Mendez, J. N., Khan, D., & Miruo, L. (2019). Pore size distribution, their geometry and connectivity in deeply buried Paleogene Es1 sandstone reservoir, Nanpu Sag, East China. *Petroleum Science*, *16*(5), 981-1000.

Kast, W., & Hohenthanner, C.-R. (2000). Mass transfer within the gas-phase of porous media. *International Journal of Heat and Mass Transfer*, *43*(5), 807-823.

Kate, J. M., & Gokhale, C. S. (2006). A simple method to estimate complete pore size distribution of rocks. *Engineering Geology*, *84*(1-2), 48-69.

Katsube, T., & Williamson, M. (1994). Effects of diagenesis on shale nano-pore structure and implications for sealing capacity. *Clay Minerals*, *29*(4), 451-461.

Katz, A. J., & Thompson, A. (1985). Fractal sandstone pores: implications for conductivity and pore formation. *Physical Review Letters*, *54*(12), 1325.

Katz, A., & Thompson, A. (1986). Quantitative prediction of permeability in porous rock. *Physical Review B*, *34*(11), 8179.

Kaufmann, J., Loser, R., & Leemann, A. (2009). Analysis of cement-bonded materials by multi-cycle mercury intrusion and nitrogen sorption. *Journal of Colloid and Interface Science*, *336*(2), 730-737.

Kc, B., Foroutan, M., Kamali-Asl, A., Ghazanfari, E., & Cladouhos, T. (2019). *Geomechanical Characterization of a Granodiorite Rock Specimen from Patua Geothermal Field.* 53rd US Rock Mechanics/Geomechanics Symposium,

Keller, L. M., Holzer, L., Wepf, R., & Gasser, P. (2011). 3D geometry and topology of pore pathways in Opalinus clay: Implications for mass transport. *Applied Clay Science*, *52*(1-2), 85-95.

Khanqa, P. A., Karim, S. A., Sissakian, V. K., & Kareem, K. H. (2009). Lithostratigraphic study of a late Oligocene–Early Miocene succession, south of Sulaimaniyah, NE Iraq. *Iraqi Bulletin of Geology and Mining*, *5*(2), 41-57.

Khasainov, B., Ermolaev, B., Presles, H.-N., & Vidal, P. (1997). On the effect of grain size on shock sensitivity of heterogeneous high explosives. *Shock Waves*, *7*(2), 89-105.

Klaver, J., Desbois, G., Littke, R., & Urai, J. L. (2015). BIB-SEM characterization of pore space morphology and distribution in postmature to overmature samples from the Haynesville and Bossier Shales. *Marine and Petroleum Geology*, *59*, 451-466.

Klaver, J., Hemes, S., Houben, M., Desbois, G., Radi, Z., & Urai, J. (2015). The connectivity of pore space in mudstones: insights from high-pressure Wood's metal injection, BIB-SEM imaging, and mercury intrusion porosimetry. *Geofluids*, *15*(4), 577-591.

Knözinger, H., & Kochloefl, K. (2000). Heterogeneous catalysis and solid catalysts. *Ullmann's Encyclopedia of Industrial Chemistry*.

Kosuge, K., Kubo, S., Kikukawa, N., & Takemori, M. (2007). Effect of pore structure in mesoporous silicas on VOC dynamic adsorption/desorption performance. *Langmuir*, *23*(6), 3095-3102.

Lai, J., Wang, G., Wang, Z., Chen, J., Pang, X., Wang, S., Zhou, Z., He, Z., Qin, Z., & Fan, X. (2018). A review on pore structure characterization in tight sandstones. *Earth-Science Reviews*, *177*, 436-457.

Lambert, L., Durlet, C., Loreau, J.-P., & Marnier, G. (2006). Burial dissolution of micrite in Middle East carbonate reservoirs (Jurassic–Cretaceous): keys for recognition and timing. *Marine and Petroleum Geology*, *23*(1), 79-92.

Lander, R. H., & Walderhaug, O. (1999). Predicting porosity through simulating sandstone compaction and quartz cementation. *AAPG Bulletin*, *83*(3), 433-449.

Levy, B., & Chambers, R. (1987). Bromide as a conservative tracer for soil-water studies. *Hydrological Processes*, *1*(4), 385-389.

Li, M., Guo, P., Stolle, D. F., Liang, L., & Shi, Y. (2020). Modeling hydraulic fracture in heterogeneous rock materials using permeability-based hydraulic fracture model. *Underground Space*, *5*(2), 167-183.

Li, M., Wu, J., Li, J., Zhuang, L., Wang, S., & Zhang, F. (2022). Modeling of hydraulic fracturing in polymineralic rock with a grain-based DEM coupled with a pore network model. *Engineering Fracture Mechanics*, *275*, 108801.

Li, P., Zheng, M., Bi, H., Wu, S., & Wang, X. (2017). Pore throat structure and fractal characteristics of tight oil sandstone: A case study in the Ordos Basin, China. *Journal of Petroleum Science and Engineering*, *149*, 665-674.

Li, W. D., & Qiang, W. Z. (2004). Counting secondary porosity in metamorphic rock with microresistivity images: a land case study from China. In *SPWLA 45th Annual Logging Symposium*, Noordwijk, Netherlands.

Li, X., Puhakka, E., Ikonen, J., Söderlund, M., Lindberg, A., Holgersson, S., Martin, A., & Siitari-Kauppi, M. (2018). Sorption of Se species on mineral surfaces, part I: Batch sorption and multi-site modelling. *Applied Geochemistry*, *95*, 147-157.

Li, X., Xiao, W., He, G., Zheng, W., Yu, N., & Tan, M. (2012). Pore size and surface area control of MgO nanostructures using a surfactant-templated hydrothermal process: high adsorption capability to azo dyes. *Colloids and Surfaces A: Physicochemical and Engineering Aspects*, *408*, 79-86.

Li, X., Yao, D., Zuo, K., Xia, Y., Yin, J., Liang, H., & Zeng, Y.-P. (2019). Fabrication, microstructural characterization and gas permeability behavior of porous silicon nitride ceramics with controllable pore structures. *Journal of the European Ceramic Society*, *39*(9), 2855-2861.

Li, Y., Chang, X., Yin, W., Sun, T., & Song, T. (2017). Quantitative impact of diagenesis on reservoir quality of the Triassic Chang 6 tight oil sandstones, Zhenjing area, Ordos Basin, China. *Marine and Petroleum Geology*, *86*, 1014-1028.

Li, Y., Chang, X., Yin, W., Wang, G., Zhang, J., Shi, B., Zhang, J., & Mao, L. (2019). Quantitative identification of diagenetic facies and controls on reservoir quality for tight sandstones: A case study of the Triassic Chang 9 oil layer, Zhenjing area, Ordos Basin. *Marine and Petroleum Geology*, *102*, 680-694.

Li, Y., Li, M., Li, Z., Yang, L., & Liu, X. (2019). Effects of particle size and solution chemistry on Triclosan sorption on polystyrene microplastic. *Chemosphere*, *231*, 308-314.

Li, Y., Yang, Y., Dong, M., Liu, C., Iglauer, S., Kang, L., Yao, J., Zhang, K., Sun, H., & Zhang, L. (2022). Effect of pore structure and capillary number on gas-water flow patterns in carbonate rocks. *SPE Journal*, *27*(04), 1895-1904.

Lim, Y. Y., Pham, T. M., & Kumar, J. (2021). Sustainable alkali activated concrete with fly ash and waste marble aggregates: Strength and Durability studies. *Construction and Building Materials*, *283*, 122795.

Liu, H., Zhang, S., Song, G., Xuejun, W., Teng, J., Wang, M., Bao, Y., Yao, S., Wang, W., & Zhang, S. (2019). Effect of shale diagenesis on pores and storage capacity in the Paleogene Shahejie Formation, Dongying Depression, Bohai Bay Basin, east China. *Marine and Petroleum Geology*, *103*, 738-752.

Liu, H., Zhao, Y., Luo, Y., Chen, Z., & He, S. (2015). Diagenetic facies controls on pore structure and rock electrical parameters in tight gas sandstone. *Journal of Geophysics and Engineering*, *12*(4), 587-600.

Loog, A., Kurvits, T., Aruvali, J., & Petersell, V. (2001). Grain size analysis and mineralogy of the Tremadocian Dictyonema shale in Estonia. *Oil Shale*, *18*(4), 281-297.

Lu, S.-G., Malik, Z., Chen, D. P., & Wu, C. F. (2014). Porosity and pore size distribution of Ultisols and correlations to soil iron oxides. *Catena*, *123*, 79-87.

Lucas, M., Vetterlein, D., Vogel, H. J., & Schlüter, S. (2021). Revealing pore connectivity across scales and resolutions with X‐ray CT. *European Journal of Soil Science*, *72*(2), 546-560.

Makowitz, A., Lander, R., & Milliken, K. (2006). Diagenetic modeling to assess the relative timing of quartz cementation and brittle grain processes during compaction. *AAPG Bulletin*, *90*(6), 873-885.

Makowitz, A., & Milliken, K. L. (2003). Quantification of brittle deformation in burial compaction, Frio and Mount Simon Formation sandstones. *Journal of Sedimentary Research*, *73*(6), 1007-1021.

Malekimostaghim, E., Gholami, R., Rezaee, R., Asef, M. R., Zhong, Z., & Sarmadivaleh, M. (2019). A laboratory-based approach to determine Archie's cementation factor for shale reservoirs. *Journal of Petroleum Science and Engineering*, 183, 106399.

Mandelbrot, B. B., & Mandelbrot, B. B. (1982). *The fractal geometry of nature* (Vol. 1). WH freeman New York.

Marshall, J. D., & Pirrie, D. (2013). Carbonate concretions—explained. *Geology Today*, *29*(2), 53-62.

Mastalerz, M., Hampton, L., Drobniak, A., Loope, H., 2017. Significance of analytical particle size in low-pressure N_2 and CO_2 adsorption of coal and shale. *International Journal of Coal Geology*, 178, 122-131.

Matsui, Y., Ando, N., Yoshida, T., Kurotobi, R., Matsushita, T., Ohno, K., 2011. Modeling high adsorption capacity and kinetics of organic macromolecules on super-powdered activated carbon. *Water Research*, 45(4), 1720-1728.

Mazzullo, S., & Harris, P. (1991). An overview of dissolution porosity development in the deep-burial environment, with examples from carbonate reservoirs in the Permian Basin. *West Texas Geological Society, Midland, Texas*, 91-89.

McKinley, J. M., Atkinson, P. M., Lloyd, C. D., Ruffell, A. H., & Worden, R. (2011). How porosity and permeability vary spatially with grain size, sorting, cement volume, and mineral dissolution in fluvial Triassic sandstones: the value of geostatistics and local regression. *Journal of Sedimentary Research*, *81*(12), 844-858.

Mitchell, S. F., Ball, J. D., Crowley, S. F., Marshall, J. D., Paul, C. R., Veltkamp, C. J., & Samir, A. (1997). Isotope data from Cretaceous chalks and foraminifera: Environmental or diagenetic signals? *Geology*, *25*(8), 691-694.

Mohammed, I., Al Shehri, D. A., Mahmoud, M., Kamal, M. S., & Alade, O. (2021). Surface Charge Investigation of Reservoir Rock Minerals. *Energy & Fuels*, *35*(7), 6003-6021.

Moldrup, P., Olesen, T., Blendstrup, H., Komatsu, T., de Jonge, L. W., & Rolston, D. E. (2007). Predictive-Descriptive Models for Gas and Solute Diffusion Coefficients in Variably Saturated Porous Media Coupled to Pore-Size Distribution. *Soil Science*, *172*(10), 741-750.

Mondol, N. H., Bjørlykke, K., Jahren, J., & Høeg, K. (2007). Experimental mechanical compaction of clay mineral aggregates—Changes in physical properties of mudstones during burial. *Marine and Petroleum Geology*, *24*(5), 289-311.

Mørk, M. B. E. (2013). Diagenesis and quartz cement distribution of low-permeability Upper Triassic–Middle Jurassic reservoir sandstones, Longyearbyen CO2 lab well site in Svalbard, Norway. *AAPG Bulletin*, *97*(4), 577-596.

Mu, D., Liu, Z.-S., Huang, C., & Djilali, N. (2008). Determination of the effective diffusion coefficient in porous media including Knudsen effects. *Microfluidics and Nanofluidics*, *4*(3), 257-260.

Musso, T. B., Carlos, L., Parolo, M. E., Francisca, F. M., Pettinari, G., Giuliano, V., & Ruffato, M. (2022). Mudstones as Landfill Liner Material for Heavy Metal Removal: Equilibrium and Dynamic Sorption Study. *Water, Air, & Soil Pollution*, *233*(4), 1-16.

Navarre-Sitchler, A., Brantley, S. L., & Rother, G. (2015). How porosity increases during incipient weathering of crystalline silicate rocks. *Reviews in Mineralogy and geochemistry*, *80*(1), 331-354.

Nishimura, H., Kouduka, M., Fukuda, A., Ishimura, T., Amano, Y., Beppu, H., Miyakawa, K., & Suzuki, Y. (2022). Fe (III)-dependent anaerobic methane-oxidizing activity in a deep underground borehole demonstrated by in-situ pressure groundwater incubation. *bioRxiv*.

Noiriel, C., Bernard, D., Gouze, P., & Thibault, X. (2005). Hydraulic properties and microgeometry evolution accompanying limestone dissolution by acidic water. *Oil & Gas Science and Technology*, *60*(1), 177-192.

Okabe, H., & Blunt, M. J. (2005). Pore space reconstruction using multiple-point statistics. *Journal of Petroleum Science and Engineering*, *46*(1-2), 121-137.

Olsen, C., Hongdul, T., & Lykke Fabricius, I. (2008). Prediction of Archie's cementation factor from porosity and permeability through specific surface. *Geophysics*, *73*(2), E81-E87.

Pang, Y., Soliman, M. Y., Deng, H., & Xie, X. (2017). Experimental and analytical investigation of adsorption effects on shale gas transport in organic nanopores. *Fuel*, *199*, 272-288.

Peng, S., Hu, Q., Dultz, S., & Zhang, M. (2012). Using X-ray computed tomography in pore structure characterization for a Berea sandstone: Resolution effect. *Journal of Hydrology*, *472*, 254-261.

Peng, S., Hu, Q., & Hamamoto, S. (2012). Diffusivity of rocks: Gas diffusion measurements and correlation to porosity and pore size distribution. *Water Resources Research*, *48*(2).

Peth, S., Horn, R., Beckmann, F., Donath, T., Fischer, J., & Smucker, A. (2008). Three-dimensional quantification of intra-aggregate pore-space features using synchrotron-radiation-based microtomography. *Soil Science Society of America Journal*, *72*(4), 897-907.

Phounglamcheik, A., Bäckebo, M., Robinson, R., & Umeki, K. (2022). The significance of intraparticle and interparticle diffusion during CO2 gasification of biomass char in a packed bed. *Fuel*, *310*, 122302.

Ping, L., & Machel, H. G. (1995). Pore size and pore throat types in a heterogeneous dolostone reservoir, Devonian Grosmont Formation, Western Canada sedimentary basin. *AAPG Bulletin*, *79*(11), 1698-1720.

Pittman, E. D. (1992). Relationship of porosity and permeability to various parameters derived from mercury injection-capillary pressure curves for sandstone. *AAPG Bulletin*, *76*(2), 191-198.

Plötze, M., & Niemz, P. (2011). Porosity and pore size distribution of different wood types as determined by mercury intrusion porosimetry. *European Journal of Wood and Wood Products*, *69*(4), 649-657.

Porcheron, F., Monson, P., & Thommes, M. (2004). Modeling mercury porosimetry using statistical mechanics. *Langmuir*, *20*(15), 6482-6489.

Porter, C. R., & Carothers, J. E. (1970, May). Formation factor-porosity relation derived from well log data. In SPWLA Annual Logging Symposium (pp. SPWLA-1970). SPWLA.

Portsmouth, R., & Gladden, L. (1991). Determination of pore connectivity by mercury porosimetry. *Chemical Engineering Science*, *46*(12), 3023-3036.

Punyapalakul, P., Suksomboon, K., Prarat, P., & Khaodhiar, S. (2013). Effects of surface functional groups and porous structures on adsorption and recovery of perfluorinated compounds by inorganic porous silicas. *Separation Science and Technology*, *48*(5), 775-788.

Raiga-Clemenceau, J. (1977). The cementation exponent in the formation factor-porosity relation: The effect of permeability. SPWLA 18th Annual Logging Symposium, Houston, Texas.

Raposo, F., De La Rubia, M., Borja, R., 2009. Methylene blue number as useful indicator to evaluate the adsorptive capacity of granular activated carbon in batch mode: Influence of adsorbate/adsorbent mass ratio and particle size. *Journal of Hazardous Materials*, 165(1-3), 291-299.

Regnet, J., David, C., Robion, P., & Menéndez, B. (2019). Microstructures and physical properties in carbonate rocks: A comprehensive review. *Marine and Petroleum Geology*, *103*, 366-376.

Rezaee, M. R., Motiei, H., & Kazemzadeh, E. (2007). A new method to acquire m exponent and tortuosity factor for microscopically heterogeneous carbonates. *Journal of Petroleum Science and Engineering*, 56(4), 241-251.

Rivero, O. G. (1977, June). Some considerations about the possible use of the parameters a and m as a formation evaluation tool through well logs. In SPWLA Annual Logging Symposium (pp. SPWLA-1977).

Rolston, D. E., & Moldrup, P. (2002). 4.3 Gas Diffusivity. *Methods of Soil Analysis: Part 4 Physical Methods*, *5*, 1113-1139.

Rushing, J. A., Newsham, K. E., & Blasingame, T. A. (2008). Rock typing: Keys to understanding productivity in tight gas sands. In *SPE Unconventional Reservoirs Conference*, Keystone, Colorado.

RP40, A. (1998). Recommended Practices for Core Analysis. *Feb*.

Sahimi, M. (1993). Flow phenomena in rocks: from continuum models to fractals, percolation, cellular automata, and simulated annealing. *Reviews of Modern Physics*, *65*(4), 1393.

Salem, H. S., & Chilingarian, G. V. (1999). The cementation factor of Archie's equation for shaly sandstone reservoirs. *Journal of Petroleum Science and Engineering*, *23*(2), 83-93.

Sammaljärvi, J., Jokelainen, L., Ikonen, J., & Siitari-Kauppi, M. (2012). Free radical polymerisation of MMA with thermal initiator in brick and Grimsel granodiorite. *Engineering Geology*, *135-136*, 52-59.

Sasamoto, H., Satoh, H., & Arthur, R. C. (2018). Characterization of mineralogical controls on ammonium concentrations in deep groundwaters of the Horonobe area, Hokkaido. *Journal of Geochemical Exploration*, *188*, 318-325.

Sbiga, H. M., & Alusta, G. (2019). Deriving a correlation of cementation factor in Nubian sandstone formation (Upper and Lower Cretaceous), Sirt Basin. *International Journal of Petrochemistry and Research*, 3, 286-291.

Schlanger, S. O., & Douglas, R. G. (1974). The pelagic ooze-chalk-limestone transition and its implications for marine stratigraphy. In *Pelagic Sediments: on Land and under the Sea* (Vol. 1, pp. 117-148). Blackwell Scientific Publications Oxford, London, Edinburgh, Melbourne.

Schmitt, M., Fernandes, C. P., da Cunha Neto, J. A., Wolf, F. G., & dos Santos, V. S. (2013). Characterization of pore systems in seal rocks using nitrogen gas adsorption combined with mercury injection capillary pressure techniques. *Marine and Petroleum Geology*, *39*(1), 138-149.

Schmitt, M., Fernandes, C. P., Wolf, F. G., da Cunha Neto, J. A. B., Rahner, C. P., & dos Santos, V. S. S. (2015). Characterization of Brazilian tight gas sandstones relating permeability and Angstrom-to micron-scale pore structures. *Journal of Natural Gas Science and Engineering*, *27*, 785-807.

Schneeberger, R., Kober, F., Spillmann, T., Blechschmidt, I., Lanyon, G.W., Mäder, U.K., 2019. *Grimsel Test Site: Revisiting the site-specific geoscientific knowledge*. National Cooperative for the Disposal of Radioactive Waste (NAGRA), No. NTB-19-01.

Schön, J. (2011). *Physical Properties of Rocks: A Workbook* (Vol. 8). Elsevier.

Schön, J. H. (2015). *Physical properties of rocks: Fundamentals and principles of petrophysics*. Elsevier.

Sepulveda, P., Jones, J.R., Hench, L.L., 2001. Characterization of melt-derived 45S5 and sol-gel–derived 58S bioactive glasses. *Journal of Biomedical Materials Research*, 58(6), 734-740.

Shah, S. M., Crawshaw, J. P., Gray, F., Yang, J., & Boek, E. S. (2017). Convex hull approach for determining rock representative elementary volume for multiple petrophysical parameters using pore-scale imaging and Lattice–Boltzmann modelling. *Advances in Water Resources*, *104*, 65-75.

Shaheen, S. M., Derbalah, A. S., & Moghanm, F. S. (2012). Removal of heavy metals from aqueous solution by zeolite in competitive sorption system. *International Journal of Environmental Science and Development*, *3*(4), 362.

Shalaby, M. R., Hakimi, M. H., & Abdullah, W. H. (2014). Diagenesis in the middle Jurassic Khatatba formation sandstones in the Shoushan Basin, northern Western Desert, Egypt. *Geological Journal*, *49*(3), 239-255.

Siemers, W., Caldwell, C., Farrel, H., Young, C., Yang-Logan, J., & Howard, J. (1994). Chalk lithofacies, fractures, petrophysics and paleontology-An interactive study of chalk reservoirs. EAPG/AAPG Special Conference on Chalk,

Silin, D., & Patzek, T. (2006). Pore space morphology analysis using maximal inscribed spheres. *Physica A: Statistical Mechanics and Its Applications*, *371*(2), 336-360.

Slatt, R. M., & O'Brien, N. R. (2011). Pore types in the Barnett and Woodford gas shales: Contribution to understanding gas storage and migration pathways in fine-grained rocks. *AAPG Bulletin*, *95*(12), 2017-2030.

Soil Science Society of America. (2008). *Glossary of Soil Science Terms 2008*. ASA-CSSA-SSSA.

Sondergeld, C. H., Ambrose, R. J., Rai, C. S., & Moncrieff, J. (2010). *Micro-structural studies of gas shales.* SPE Unconventional Gas Conference.

Stipp, S.L.S., Lakshtanov, L.Z., Jensen, J.T., Baker, J.A., 2003. Eu^{3+} uptake by calcite: Preliminary results from coprecipitation experiments and observations with surface-sensitive techniques. *Journal of Contaminant Hydrology,* 61(1-4), 33-43.

Sun, H., Yao, J., Cao, Y.-c., Fan, D.-y., & Zhang, L. (2017). Characterization of gas transport behaviors in shale gas and tight gas reservoirs by digital rock analysis. *International Journal of Heat and Mass Transfer, 104*, 227-239.

Tabibi, M., & Emadi, M. (2003). *Variable cementation factor determination (empirical methods).* SPE Middle East Oil and Gas Show and Conference.

Tachi, Y., Ito, T., & Gylling, B. (2021). A scaling approach for retention properties of crystalline rock: Case study of the In-Situ Long-Term Sorption and Diffusion Experiment (LTDE-SD) at the Äspö Hard Rock Laboratory in Sweden. *Water Resources Research*, *57*(11), e2020WR029335.

Tachi, Y., Shibutani, T., Sato, H., & Yui, M. (1998). Sorption and diffusion behavior of selenium in tuff. *Journal of Contaminant Hydrology*, *35*(1-3), 77-89.

Taylor, K., Macquaker, J., & Shaw, H. (2014). Diagenetic alterations in a silt-and clay-rich mudstone succession: an example from the Upper Cretaceous Mancos Shale of Utah, USA. *Clay Minerals*, *49*(2), 213-227.

Teng, H., & Zhao, T. (2000). An extension of Darcy's law to non-Stokes flow in porous media. *Chemical Engineering Science*, *55*(14), 2727-2735.

Tews, J., Brose, U., Grimm, V., Tielbörger, K., Wichmann, M. C., Schwager, M., & Jeltsch, F. (2004). Animal species diversity driven by habitat heterogeneity/diversity: the importance of keystone structures. *Journal of Biogeography*, *31*(1), 79-92.

Timur, A., Hempkins, W., & Weinbrandt, R. (1971). Scanning electron microscope study of pore systems in rocks. *Journal of Geophysical Research*, *76*(20), 4932-4948.

Timur, A., Hempkins, W. B., & Worthington, A. E. (1972, May). Porosity and pressure dependence of formation resistivity factor for sandstones. In Trans CWLS 4th Formation Evaluation Symposium (Vol. 30).

Tokunaga, T. K., Shen, W., Wan, J., Kim, Y., Cihan, A., Zhang, Y., & Finsterle, S. (2017). Water saturation relations and their diffusion-limited equilibration in gas shale: Implications for gas flow in unconventional reservoirs. *Water Resources Research*, *53*(11), 9757-9770.

Tucker, M. E., & Bathurst, R. G. (2009). *Carbonate Diagenesis*. John Wiley & Sons.

Veeresh, H., Tripathy, S., Chaudhuri, D., Hart, B., & Powell, M. (2003). Sorption and distribution of adsorbed metals in three soils of India. *Applied Geochemistry*, *18*(11), 1723-1731.

Venegas, M. J., Fregoso-Israel, E., Escamilla, R., & Pfeiffer, H. (2007). Kinetic and reaction mechanism of CO_2 sorption on Li_4SiO_4: Study of the particle size effect. *Industrial & Engineering Chemistry Research*, *46*(8), 2407-2412.

Viana, M., Jouannin, P., Pontier, C., & Chulia, D. (2002). About pycnometric density measurements. *Talanta*, *57*(3), 583-593.

Vik, B., Bastesen, E., & Skauge, A. (2013). Evaluation of representative elementary volume for a vuggy carbonate rock—Part: Porosity, permeability, and dispersivity. *Journal of Petroleum Science and Engineering*, *112*, 36-47.

Vogel, H., & Kretzschmar, A. (1996). Topological characterization of pore space in soil—sample preparation and digital image-processing. *Geoderma*, *73*(1-2), 23-38.

Vogel, H.-J., & Roth, K. (2001). Quantitative morphology and network representation of soil pore structure. *Advances in Water Resources*, *24*(3-4), 233-242.

Voutilainen, M., Kekäläinen, P., Siitari-Kauppi, M., Sardini, P., Muuri, E., Timonen, J., & Martin, A. (2017). Modeling transport of cesium in Grimsel granodiorite with micrometer scale heterogeneities and dynamic update of Kd. *Water Resources Research*, *53*(11), 9245-9265.

Wang, F., Yang, K., You, J., & Lei, X. (2019). Analysis of pore size distribution and fractal dimension in tight sandstone with mercury intrusion porosimetry. *Results in Physics*, *13*, 102283.

Wang, G., Chang, X., Yin, W., Li, Y., & Song, T. (2017). Impact of diagenesis on reservoir quality and heterogeneity of the Upper Triassic Chang 8 tight oil sandstones in the Zhenjing area, Ordos Basin, China. *Marine and Petroleum Geology*, *83*, 84-96.

Wang, T., Zhang, L., Li, C., Yang, W., Song, T., Tang, C., Meng, Y., Dai, S., Wang, H., & Chai, L. (2015). Synthesis of core–shell magnetic Fe_3O_4@ poly (m-phenylenediamine) particles for chromium reduction and adsorption. *Environmental Science & Technology*, *49*(9), 5654-5662.

Wang, Y., Liu, L., & Cheng, H. (2021). Gas adsorption characterization of pore structure of organic-rich shale: Insights into contribution of organic matter to shale pore network. *Natural Resources Research*, *30*(3), 2377-2395.

Wardlaw, N., & Cassan, J. (1978). Estimation of recovery efficiency by visual observation of pore systems in reservoir rocks. *Bulletin of Canadian Petroleum Geology*, *26*(4), 572-585.

Wardlaw, N. C. (1980). The effects of pore structure on displacement efficiency in reservoir rocks and in glass micromodels. SPE/DOE Enhanced Oil Recovery Symposium.

Washburn, E. W. (1921). Note on a method of determining the distribution of pore sizes in a porous material. *Proceedings of the National Academy of Sciences of the United States of America*, *7*(4), 115.

Wei, L., Cook, A., Daigle, H., Malinverno, A., Nole, M., & You, K. (2019). Factors controlling short-range methane migration of gas hydrate accumulations in thin coarse-grained layers. *Geochemistry, Geophysics, Geosystems*, *20*(8), 3985-4000.

Westphal, H., Eberli, G. P., Smith, L. B., Grammer, G. M., & Kislak, J. (2004). Reservoir characterization of the Mississippian Madison formation, Wind River Basin, Wyoming. *AAPG Bulletin*, *88*(4), 405-432.

Whitthueser, K., Hötzl, H., Reichert, B., Stichler, W., & Nativ, R. (2000). Laboratory experiments for diffusion transport processes in fractured chalk. *IAHS Publication(International Association of Hydrological Sciences)*(262), 303-308.

Widarsono, B. (2011). The importance of litho-facies distinction in determining the most representative cementation factors for well-log evaluation: an old issue persistently neglected. *Scientific Contributions Oil and Gas*, *34*(2), 139-148.

Wu, F., Wen, Z., Yao, C., Wang, X., Xi, Y., & Cong, L. (2020). Numerical simulation of the influence of pore structure on resistivity, Formation factor and cementation index in tight sandstone. *Acta Geologica Sinica -English Edition*, *94*(2), 290-304.

Wu, K., Van Dijke, M. I., Couples, G. D., Jiang, Z., Ma, J., Sorbie, K. S., Crawford, J., Young, I., & Zhang, X. (2006). 3D stochastic modelling of heterogeneous porous media– applications to reservoir rocks. *Transport in Porous Media*, *65*, 443-467.

Wu, M., Fridh, K., Johannesson, B., & Geiker, M. (2018). Impact of sample crushing on porosity characterization of hardened cement pastes by low temperature calorimetry: Comparison of powder and cylinder samples. *Thermochimica Acta*, *665*, 11-19.

Wyllie, M., & Rose, W. D. (1950). Some theoretical considerations related to the quantitative evaluation of the physical characteristics of reservoir rock from electrical log data. *Journal of Petroleum Technology*, *2*(04), 105-118.

Wyllie, M., & Gregory, A. (1953). Formation factors of unconsolidated porous media: Influence of particle shape and effect of cementation. *Journal of Petroleum Technology*, *5*(04), 103-110.

Wyllie, M., & Spangler, M. (1952). Application of electrical resistivity measurements to problem of fluid flow in porous media. *AAPG Bulletin*, *36*(2), 359-403.

Xiong, Q., Baychev, T. G., & Jivkov, A. P. (2016). Review of pore network modelling of porous media: Experimental characterisations, network constructions and applications to reactive transport. *Journal of Contaminant Hydrology*, *192*, 101-117.

Xue, R., Li, R., Guo, H., Guo, L., Su, Z., Ni, X., Qi, L., Zhang, T., Li, Q., & Zhang, Z. (2016). Variable intra-tumor genomic heterogeneity of multiple lesions in patients with hepatocellular carcinoma. *Gastroenterology*, *150*(4), 998-1008.

Yan, J., Xue, Y., Long, L., Zeng, Y., & Hu, X. (2018). Adsorptive removal of As (V) by crawfish shell biochar: batch and column tests. *Environmental Science and Pollution Research*, *25*(34), 34674-34683.

Yang, R., Hu, Q., Yi, J., Zhang, B., He, S., Guo, X., Hou, Y., & Dong, T. (2019). The effects of mineral composition, TOC content and pore structure on spontaneous imbibition in Lower Jurassic Dongyuemiao shale reservoirs. *Marine and Petroleum Geology*, *109*, 268-278.

Yang, X., Yi, H., Tang, X., Zhao, S., Yang, Z., Ma, Y., Feng, T., & Cui, X. (2018). Behaviors and kinetics of toluene adsorption‐desorption on activated carbons with varying pore structure. *Journal of Environmental Sciences*, *67*, 104-114.

Yao, Q.-l., Xia, Z., Tang, C.-J., Zhu, L., Wang, W.-N., Chen, T., & Tan, Y.-M. (2020). Characteristics of heavy metal ion adsorption by silty mudstones in coal mine goafs. *Geofluids*, *2020*.

Yao, Y., Liu, D., Che, Y., Tang, D., Tang, S., & Huang, W. (2010). Petrophysical characterization of coals by low-field nuclear magnetic resonance (NMR). *Fuel*, *89*(7), 1371-1380.

Yavuz, H., Demirdag, S., & Caran, S. (2010). Thermal effect on the physical properties of carbonate rocks. *International Journal of Rock Mechanics and Mining Sciences*, *47*(1), 94-103.

Yin, Y., Qu, Z., & Zhang, J. (2019). Multiple diffusion mechanisms of shale gas in nanoporous organic matter predicted by the local diffusivity lattice Boltzmann model. *International Journal of Heat and Mass Transfer*, *143*, 118571.

Yoo, H., Park, J., Lee, Y., & Lee, J. (2019). An experimental investigation into the effect of pore size distribution on the acid-rock reaction in carbonate acidizing. *Journal of Petroleum Science and Engineering*, *180*, 504-517.

Yuan, X., Hu, Q., Lin, X., Zhao, C., Wang, Q., Tachi, Y., Fukatsu, Y., Hamamoto, S., Siitari-Kauppi, M., & Li, X. (2023). Pore connectivity influences mass transport in natural rocks: Pore structure, gas diffusion and batch sorption studies. *Journal of Hydrology*, *618*, 129172.

Zachara, J. M., Smith, S. C., Liu, C., McKinley, J. P., Serne, R. J., & Gassman, P. L. (2002). Sorption of Cs+ to micaceous subsurface sediments from the Hanford site, USA. *Geochimica et Cosmochimica Acta*, *66*(2), 193-211.

Zavarin, M., Roberts, S.K., Hakem, N., Sawvel, A.M., Kersting, A.B., 2005. Eu (III), Sm (III), Np (V), Pu (V), and Pu (IV) sorption to calcite. *Radiochimica Acta*, 93(2), 93-102.

Zhai, G.-y., Wang, Y.-f., Zhou, Z., Liu, G.-h., Yang, Y.-r., & Li, J. (2018). "Source-Diagenesis-Accumulation" enrichment and accumulation regularity of marine shale gas in southern China. *China Geology*, *1*(3), 319-330.

Zhao, C., Zhou, W., Hu, Q., Xu, H., & Zhang, C. (2021). Porosity measurement of granular rock samples by modified bulk density analyses with particle envelopment. *Marine and Petroleum Geology*, *133*, 105273.

Zhong, Z., Rezaee, R., Esteban, L., Josh, M., & Feng, R. (2021). Determination of Archie's cementation exponent for shale reservoirs; an experimental approach. *Journal of Petroleum Science and Engineering*, 201, 108527.

Zhuang, J., & Yu, G.-R. (2002). Effects of surface coatings on electrochemical properties and contaminant sorption of clay minerals. *Chemosphere*, *49*(6), 619-628.